ON-CHIP MAGNETIC SEPARATION

DESIGN, FABRICATION, AND CHARACTERIZATION OF MICRO-ELECTROMAGNETIC DEVICES FOR MANIPULATION OF MAGNETIC PARTICLES

By AMIN (SEYED) HOSSEINI, B.Eng.

A Thesis Submitted to the School of Graduate Studies in Partial Fulfilment of the Requirements for the Degree Doctor of Philosophy in Biomedical Engineering

McMaster University DOCTOR OF PHILOSOPHY (2018) Hamilton, Ontario

(Biomedical Engineering)

TITLE: Design, Fabrication, and Characterization of Micro-Electromagnetic Devices for Manipulation of Magnetic Particles

AUTHOR: Amin Hosseini, B. Eng (McMaster University)

SUPERVISOR: Professor Leyla Soleymani

NUMBER OF PAGES: xvii, 153

LAY ABSTRACT

On-chip micro-electromagnetic devices are ideally suitable for manipulating magnetic particles in an automated and fully-controlled fashion, and thus they hold great promise for integration into miniaturized, portable and handheld lab-on-a-chip platforms applicable to point-of-care settings. In this thesis, we use computer simulations and benchtop fabrication methods to develop a polymer-based magnetic device, composed of an integrated micro/nano-structured electromagnet and a ferromagnetic layer. In addition, we seek to comprehend the mutual role of thermally generated and magnetic forces on the motion of magnetic particles to enhance the device capability. This work aids us to develop a thermo-magnetic system, which can thermally concentrate magnetic particles to specific locations and magnetically capture them. Furthermore, we pursue to integrate these devices with microfluidics to separate magnetically tagged cells in a continuous flow. Finally, we investigate developing conductive, slippery, and self-cleaning surfaces which can be applied for biosensing applications.

ABSTRACT

Molecular analysis for disease management is performed in equipped laboratories by specialists. This process can be slow, costly, and inaccessible in remote rural areas. This inspires the need for developing highly specific, and robust lab-on-a-chip (LOC) devices. Analyte separation is an essential step for molecular diagnosis. Among micro-scale separation techniques, magnetophoresis benefits from its high throughput, relatively non-invasive nature, integrability, and availability of magnetic particles in variety of sizes and coatings. Magnetic forces are applied on magnetically tagged objects using permanent magnets, ferromagnetic micro/nano-structures (passive), or electromagnets (active). In this thesis, we integrate active and passive elements, by coupling micro/nano-structured electromagnets with ferromagnetic materials, to capture MPs at low currents (< 50 mA). These active-passive devices are fabricated using benchtop techniques such as xurography, polymer induced thin film wrinkling, spin coating, and electrodeposition.

An efficient transport of analytes inside LOC platforms is essential for reducing the sample-to-response time and improving the limit-of-detection. Micro-electromagnetic devices are suited for this task due to their high level of controllability over the generated magnetic force. However, the magnetic force attenuates rapidly as we move away from the surface of the device. Elevating the current improves the magnetic strength in expense of destructive Joule heating and high-power consumption. In this work, we investigate the combined role of temperature and magnetic field gradients on the motion of MPs to extent

the capture zone of the device beyond its surface. We show that the measured terminal velocities of particles located near the magnetic traps (~5.5 μm) replicate the values provided by the simualtions. Remarkably, we demonstrate two orders of magnitude deviation between the experimental and simulation results for the terminal velocities of far particles (~55.5 μm). By modelling the heat transfer of the system, we demonstrate that this inconsistency is due to the fluid movement caused by convection.

Magnetophoretic cell manipulation in a free-flow condition is beneficial in terms of high throughput and integrability. Here, after integrating the active-passive device with microfluidic channels, we successfully capture and release magnetically tagged-yeasts in a continuous flow with an applied current of 30 mA.

Micro/nanotextured lubricant-infused surfaces can be applied to LOC devices, due to their self-cleaning, frictionless, and high surface area properties. In this thesis, we integrate the wrinkling process and fluorosilanization to develop conductive lubricant-infused surfaces that are electrochemically active, slippery, and anti-biofouling. Self-assembled monolayers of fluorosilane are deposited on gold-coated shrinkable substrates. After creating the micro-wrinkled structures by heating the substrate (160°C), a lubricant is applied to the surfaces. High water contact (~150°) and low sliding angles (<5°), along with manipulation of magnetic droplets in a friction-less fashion, confirm the hydrophobicity and slipperiness of these surfaces. We demonstrate that these surfaces can prevent non-specific adhesion of proteins, which is crucial for surface-based biosensors.

ACKNOWLEDGEMENTS

I would like to start with expressing my genuine appreciation to my supervisor, Dr. Leyla Soleymani for her exceptional leadership, positive attitude, patience, and support throughout this research project and my graduate study since 2012. During these past six years, she has always been inspiring and nurturing the development of confidence to pursue independent ideas, while providing insightful advices when needed. Dr. Soleymani has been more than a prefect fit for what I could have asked for a supervisor. I would like to thank my supervisory committee members, Dr. Michael Noseworthy and Dr. Ponnambalam Ravi Selvaganapathy, for their thoughtful advices and guidance throughout my PhD.

I am privileged to be among the first generation of graduate students in Dr. Soleymani's research group, and I am grateful that I had a chance to work alongside several incredible graduate students, including Christine Gabardo, Joey Pavlovski, Stephen Woo, Jie Yang, Barnabas Fung, Roqibul Hasan, Sudip Saha, Sara Imani, Larona Toteng, Eric Daigle, Yuting Chan, Amanda Victorious, Sadman Sakib, and Sarah Traynor. I would like to especially thank David Philpott for his outstanding work and dedication to our collaborative projects.

I would like to thank my lovely family for their endless support, not just during my graduate studies, throughout my life. To my parents, thank you for all the tremendous care, support, and encouragement that you have given me during all these years. To my sisters, thank you for your emotional support. I would like to thank my best friend forever, Alireza, who has

been my sidekick for almost 12 years. Lastly, but not least, thank you to my lovely girlfriend, Nina, for always believing in me and her patience.

Finally, I would like to acknowledge the Natural Sciences and Engineering Research Council of Canada (NSERC), and McMaster University for their financial support.

TABLE OF CONTENTS

LIST OF FIGURES

LIST OF ABBREIVIATIONS AND SYMBOLS

BSA	bovine serum albumin
CTC	circulating tumor cell
CVD	chemical vapor deposition
DEP	dielectrophoresis
DNA	deoxyribonucleic acid
EDC	N-(3-dimethylaminopropyl)-N′-ethylcarbodiimide
EDX	energy-dispersive X-ray spectroscopy
FACS	fluorescence activated cell sorting
IC	integrated circuit
LOC	lab-on-a-chip
MACS	magnetic activated cell sorting
MEMS	microelectromechanical systems
MES	2-(N-morpholino) ethanesulfonic acid
MPs	magnetic particles
PBS	phosphate buffered saline
PDMS	polydimethylsiloxane
POC	point-of-care
PS	polystyrene
PSPS	pre-strained polystyrene
Py	permalloy
RIE	reactive ion etching

RNA	ribonucleic acid
SAM	self-assembled monolayer
sccm	standard cubic centimeter per minute
SEM	scanning electron microscopy
SQUID	superconducting quantum interference device
WBC	white blood cell
XPS	x-ray photoelectron spectroscopy

DECLARATION OF ACADEMIC ACHIEVEMENT

Most of the work described within this thesis was devised, conducted, analyzed, and written by the author of the thesis, in consultation from Dr. Leyla Soleymani, with the exception to the following:

Chapter 3: Paul Dube performed the superconducting quantum interference device (SQUID) measurements.

Chapter 4: David N. Philpott fabricated and tested the silicon-based micro-electromagnetic devices. He documented the entire experimental results and procedures.

Chapter 6: XPS data was obtained by Danielle Covelli. Martin Villegas performed the fluorosilanization step of the fabrication process. He also conducted the contact and sliding angle measurements, and statistical analysis. Martin aided with conducting the magnetic droplet manipulation experiments. In addition, Martin contributed to the writing of the manuscript. The scanning electron microscopy (SEM) images were obtained by Jie Yang. Jie also performed the electrodeposition of the palladium. In addition, she contributed to the experimental section of the manuscript. Maryam Badv conducted the blood plasma coagulation assay experiments. Maryam also contributed in writing the blood plasma coagulation section of the manuscript. Dr. Tohid F Didar contributed to the writing of the manuscript

Chapter 1 Introduction

This chapter reviews the motivation to develop lab-on-a-chip (LOC) devices for point-of-care (POC) diagnosis. It discusses different components of LOC technologies and explains how essential it is to be able to separate bio-molecules of interest suspended in heterogeneous biological samples. Furthermore, it reviews the current chip-based bio-separation technologies, including their advantages and disadvantages. The motivation behind designing, rapid prototyping, and characterization of the micro-electromagnets is discussed. Finally, this chapter concludes with the objectives and overview of the thesis.

1.1 Background

1.1.1 Introduction to Lab-on-a-Chip Devices for Point-of-Care Diagnostics

Infectious diseases, cancers, or even a heart attack are typical situations where early diagnosis and treatment become paramount.[1] Conventionally, patient samples are collected and analysed in laboratories using medical diagnostic equipment. These laboratory-scale instruments are acceptable for clinical or research applications where well-trained technicians are readily available, their cost of operation is relatively insignificant, and long turnaround times (for example 24 hours) are expected. However, these devices are not suitable for healthcare systems in the developing world, remote locations, and small laboratories due to their slow sample-to-result times, high cost, non-portability, and requirement for highly trained personnel. Therefore, there is a high demand for affordable,

fully automated, accurate, rapid, and portable diagnostic platforms which can be used for POC applications.

The concept of LOC or micro-total analysis system (μTAS) was first introduced by Manz *et al.* in early 1990's.[2] It was not until mid 1990's that commercial interest on LOC devices started to emerge, when LOC technologies turned out to offer solutions for genomics applications including microcapillary electrophoresis[3] and DNA microarrays.[4] In recent years, there has been tremendous interest in developing miniaturized LOC devices, which can bring medical diagnosis to the patient's sites. Generally, these LOC devices integrate multiple steps of a typical assay into a single microfluidic chip, where the sample is delivered from one assay step to the next via microchannels. These chips are designed to work with small volume of samples while remaining highly sensitive, specific, fast, portable, inexpensive, easy to operate, and environmentally friendly.[5] The LOC devices can separate, detect and analyze multiple target bio-molecules through the integration and parallelization of LOC compartments such as micro-channels, lysing, mixing, separation/sorting, and sensing chambers on a single chip. On-chip high-throughput analysis can be achieved by monitoring one sample for sensing multiple targets in parallel,[6] or by simultaneous screening of multiple samples for detecting one specific target,[7] or by combining both of these methods.[8] In addition to POC diagnostics, the LOC devices can be employed for water, nutrition, environmental, and biological warfare sensing. [9] As computer chips have accelerated and automated mathematics, LOC aims to speed up and automate biology and chemistry.[10]

LOC devices for POC diagnostics are generally composed of two main compartments: the sample preparation and the biosensor. A general scheme of a LOC device and its components are shown in Figure 1.1. A biosensor is defined as a self-sufficient integrated platform which provide specific quantitative or semi-quantitative analytical information by bringing a biorecognition element (nucleic acids, proteins, metabolites, etc.) in a direct contact with a transducer.[11] Bio-recognition used in bio-sensing is divided into two main classes: bio-catalysis and bio-affinity.[12] In bio-catalysis, one or multiple enzymes are integrated into a transducer to selectively catalyze a reaction involving a target bio-molecule as a substrate and generate quantitative analysis. [13] Bio-affinity is typically achieved by immobilizing capture probes onto the surface of a electrode or other transducer , where they can bind to their specific target biomolecules.[14] This binding event is then translated into a measurable signal using electrical/electrochemical[15], optical[16], and piezoelectric/mechanical transducers.[17]

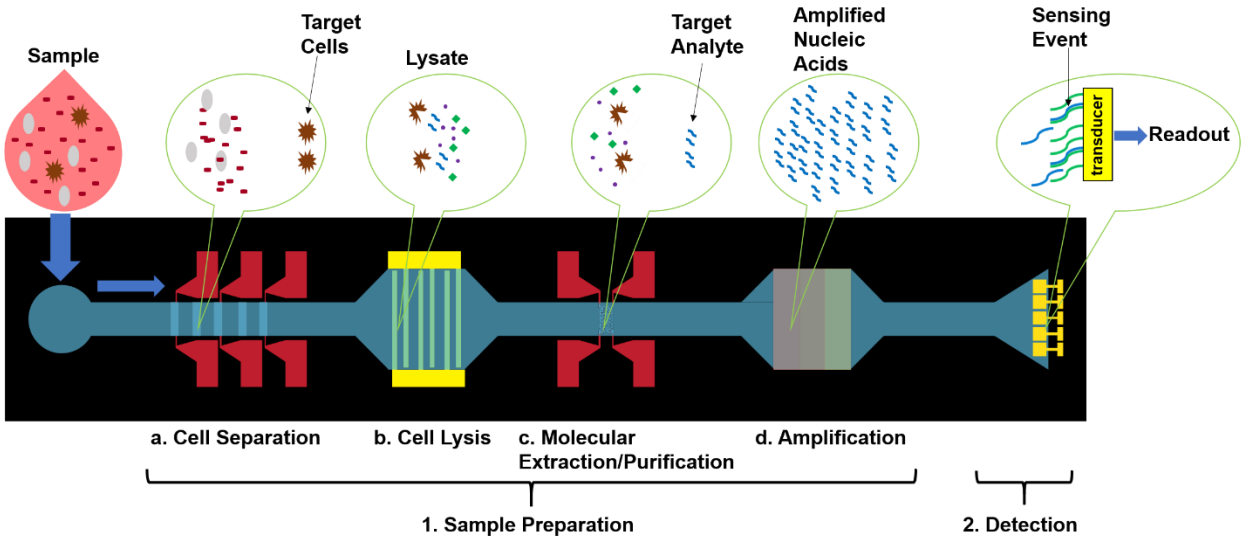

Figure 1.1 General scheme of a LOC device and its compartments.

Typical sample-preparation procedure for molecular diagnostics on a chip include cell separation/concentration, cell lysis, molecular extraction/purification, and DNA/RNA amplification.[18] Cell separation is a critical step when dealing with a heterogeneous sample (e.g. blood), particularly when the target cells are rare (e.g. circulating tumor cell (CTC)). Conventional methods used for cell separation include density gradient centrifugation,[19] fluorescence activated cell sorting (FACS),[20] and magnetic activated cell sorting (MACS).[21] In spite of high throughput screening offered by these conventional techniques, their complexity and high initial cost of the systems along with cost of operation and reagents, limit their adaption for POC settings.[22] Therefore there is a pressing need for facile and inexpensive cell separation techniques such as affinity-based[20], label-free [22], and on-chip magnetic separation methods. The above approaches are explained thoroughly in sections 1.1.2 and 1.1.3. To access a target biomolecule within a cell (e.g. nucleic acids or proteins), the separated cells need to be broken down to release their intercellular contents. This step of sample-preparation is called cell lysis which can be divided in four major categories: electrical, chemical, mechanical, and thermal lysis.[23] After the cell lysis step, the target analytes can be extracted from the rest of the sample and re-suspended in a new buffer. The molecular extraction/purification is an essential step to reduce the effect of other cellular-contamination and enhance the signal-to-noise ratio at the output of the transducer. Nucleic acid separation is classified into four main categories: silica-based surface affinity, electrostatic interactions, nano-porous membrane filtration, and functionalized micro/nano-particles.[23] In order for the extracted target nucleic acids to fall within the limits of detection of biosensors, they may

have to be amplified from low to higher copy numbers.[18] Among many amplification techniques, the enzymatic polymerase chain reaction (PCR) is the most established and commonly employed technique.[24] In PCR, typically, the temperature is raised above 92 °C to denature the complementary strands of DNA followed by decreasing the temperature to anneal primers and their enzymatic extension. Most on-chip DNA amplification researchers have focused on developing miniaturized PCR devices using integrated circuit (IC) and microelectromechanical systems (MEMS) technologies.[18] In order to effectively design the biosensing, sample preparation, and microfluidics portions of a LOC device, three specific length-scales need to be considered: the macroscopic scale of physiological samples, including millilitres of patient's body fluid, and chip dimensions; the microscopic scale of cells and biomolecular diffusion; and the nanoscale range of biological analytes.[25]

The ability to miniaturize mechanical, fluidic, electrochemical, electrical, magnetic and thermal systems has led to many new fields and applications including LOC and microfluidics. The first miniaturized analytical device was introduced by Terry *et al.,* a gas chromatographic analyzer fabricated on a silicon substrate. By taking advantage of IC processing technique, they were able to miniaturize the size of the sensor from a bulky laboratory equipment to a pocket-sized device, while maintaining the same level of performance.[26] Miniaturization of LOC devices allows multiple sample preparation and detection systems to be integrated and operated in parallel on a single chip. In addition, miniaturization enables portability, automation, and ease of use, reduces the manufacturing costs, and promotes integration of the device with other electronic measurement systems.

In terms of device functionality, miniaturized magnetic features are favorable in magnetic separation devices where the target MPs-biomolecules/cells complex are continuously sorted or captured.[27], [28] Sharp and narrow nano/microscale magnetic structures can create large magnetic field gradients which results in higher capture efficiency and throughput.[29], [30] Likewise, miniaturization greatly affects limit-of-detection and response time of a biosensor.[12] It has been shown that reducing the dimensions of an electric or electrochemical biosensing compartment enhances its sensitivity by improving the system's signal-to-noise ratio.[31] In order to exploit the enhanced signal-to-noise ratio of these sensing platforms, several microfluidic techniques have been developed to overcome the mass transport limitations and reduce the sample-to-response time from hours or days to order of minutes.[12]

Microfluidics is a technology which is employed to transport, process, and manipulate small volume (10^{-9} to 10^{-18} liters) of fluids, using micro-scale channels or reservoirs. The concept was first introduced by IBM researchers in the form of truncated pyramidal holes which were anisotropically etched in a silicon substrate.[32] The key benefits of integrating microfluidics into POC diagnostic devices include high throughput, rapid sample-to-response time, miniaturized sample size, and high sensitivity.[33] Since the diffusion time for a bio-molecule to transport from one point to another in a fluid is proportional to the square of the distance between the points,[34], [35] thus significantly faster on-chip sample preparation and detection can be achieved by using microfluidic systems. When designing microfluidic channels/reservoirs, special attention must be given to the scaling law associated with surface and geometrical effects. Miniaturizing the

dimensions of a fluidic system and high surface-to-volume ratio of micro-channels/reservoirs, often lead to an increase in interfacial surface interactions including capillary effect, viscous force, and electrostatic force, which are often neglected in macroscale. In addition, the volumetric effects such as inertial and gravity forces become insignificant as the dimensions of a channel decreases. Conventionally, transport of analytes within a microfluidic system is done using an active pressure driven flow generated by mechanical pumps. One drawback of the active transport mechanism is that at higher flow rates, the fluid velocity is at its maximum in the center of the channel, which indicates that most of the analytes practically pass through the middle of the microchannel. This is problematic because majority of LOC components such as bio-separators and biosensors are located on the bottom or top of the channel, or integrated within the walls.[36] Moreover, it has been shown that miniaturized sensors with critical features smaller than 10 μm do not efficiently deal with analytes in bulk solution, therefore elevating the analyte flux to the sensor sites by increasing the flow rate is ineffective.[37] In addition to a pressure-driven flow, there are other driving forces which can be employed, including: electrical forces in electro-osmosis, electrowetting, electrophoresis, and dielectrophoresis;[38]–[41] acoustic force in acoustophoresis;[42] magnetic force in magnetophoresis;[43] chemical or thermal gradients[44]–[47]; and surface tension in droplet-based microfluidics.[35]

Generation of a steep temperature gradients within a microfluidic channel can be used as a mechanism to transport cells, bio-molecules or particles.[45], [47], [48] This technique takes advantage of natural convection and thermophoresis to actuate the fluid

and move the analytes toward and away from the heat source, respectively.[12] Laser-induced local heating[47] and Joule heating[44] have been employed for generating the required temperature gradient. Thamdrup *et al.* introduced a laser-based microfluidic system, in which a laser beam was utilized to locally heat a portion of the micro/nano-channel to thermophoretically manipulate DNA.[47] There are many limitations and challenges involved with this technique. One limitation is that this method is not able to precisely control the movement of a single particle or cell. Furthermore, fabrication and integration of heating elements into a LOC device is a complex and time-consuming task.[12]

1.1.2 On-Chip Bio-Separation Techniques

Separation of target cells (e.g. rare CTCs) or biomolecules (e.g. nucleic acids or proteins) from a heterogeneous physiological sample is an essential step in biomedical applications such as diagnostics,[49] therapeutics,[50] and cell biology.[51] For example, blood is one of the readily available and informative tissues containing a complicated mixture of cells and proteins, from which separation of a target cell can be a tedious task. Despite these challenges, several established laboratory-based techniques have been developed to sort and separate specific cells or analytes. These methods often require an intensive need for highly trained staff to perform the procedures and are not suitable for POC application. Therefore, there has been a rising interest in development of microfluidic bio-separator for isolation of target cells or biomolecules due to their miniaturized size, reduced cost, and improved automation.[22] Several physical properties of cells, molecules, or carriers (e.g. magnetic particles) are exploited for separation purposes. These

physical properties include size[52], motility[53], electric charge[54], electric dipole moment[55], optical[56], and magnetic properties.[43] Based on these physical properties, on-chip bio-separation can be divided into three main subgroups: (i) affinity-based, (ii) label-free, and (iii) magnetic separation.

1.1.2.1 Affinity-based separation: In this approach, functionalized microchannels or micro/nanostructured materials are employed to separate cells or biomolecules of interest while keeping the targets intact for later molecular analysis. Capture agents used for affinity-based separation include antibodies such as epithelial-cell adhesion-molecule antibody (anti-EpCAM) which is a predominant capture protein for CTCs separation. Other antibodies can also be used as the capture agents which widen the applicability of these systems to non-epithelial tumors or low-level EpCAM CTCs.[20] In addition, materials such as silica or glass in a strong ionic solution have a large affinity for nucleic acid due to low level of electrostatic repulsion, which can be exploited for nucleic acid extraction.[23]

One of the early microfluidic CTC affinity-based isolation system, reported by Nagrath *et al.*, featured micro-posts etched into a silicon wafer that were labelled with anti-EpCAM. The device architecture was in such a way that maximize the physical contact between the micro-posts and cells as they flow through the device. This platform was one of the first affinity-based microfluidic device with the ability to directly process the whole blood in one step and separate CTCs without damaging them. This technology holds a great promise in early diagnosis and long-term screening of cancer, and provides the ability to analyze main biological elements responsible for blood-borne metastases.[57] It has been shown that by taking advantage of nanostructured materials, it is possible to further

improve the capture efficiency of affinity-based devices. Wang *et al.* introduced *NanoVelcro* chip which is based on an array of silicon nanopillars (SiNPs) functionalized with anti-EpCAM. High surface-to-volume ratio of the nanostructures promotes the interaction between the antibody coated SiNPs and cells, and thus enables the capture of a single tumor cell.[58]–[60] Other nanostructured materials such as functionalized conducting polymer nanodots[61], electrospun TiO_2[62], and polymer nanofibers[63] have been optimized and tested for cell separation.

Affinity-based separation can also be applied for nucleic acid purification. Micro-solid phase extraction (µSPE) is the typical technique used to separate nucleic acid on a chip. The most commonly used solid supports for µSPE of nucleic acid are silica-based. Silica has a high affinity for nucleic acid in presence of a chaotrpoic salt solution.[64] In early stages of on-chip µSPE, silica particles were maintained in a polyethylene sleeve using two glass fiber frits, and silica capillaries were connected to act as the inlet and outlet of the system. Testing the device with white blood cell (WBC) lysates resulted in ~ 70% yield rate, indicating the high binding capacity of silica beads.[65] Later on, researchers were able to maximize the capture efficiency to ~ 90% by immobilizing hybrid sol–gel/silica bead matrices within microchannels. Drawbacks of this method include bonding and shrinking issues between the channel walls and the matrix.[23] To enhance the surface area within the microchannels, silica-coated microstructures such as micropillars were fabricated in silicon wafers using reactive ion etching (RIE).[66], [67] Chen *et al.* reported an integrated microfluidic platform implementing cell separation, lysis and DNA extraction simultaneously. The nucleic acid separation module consisted of a porous silicon matrix

fabricated using anodizing method, followed by thermal oxidization to functionalize the porous matrix with silanol groups. Increasing the silanol density, using both anodizing and oxidization steps, enhanced the adsorption of the nucleic acids.[68]

Although these affinity-based methods have provided the means to isolate and study cells and nucleic acids, there are still many challenges and limitations surrounding these methods. For example, in case of separating CTCs, the heterogeneity of tumor cells and their surface biomarkers put some restrains on these methods. In addition, complex fabrication process and immobilization of micro/nanostructures within microchannels remain as one of the major challenges.

1.1.2.2 label-free separation: Label-free techniques rely on the intrinsic physical property of target cells or biomolecules. Some of these physical criteria include size, geometry, density, deformability, hydrodynamic properties, magnetic susceptibility, electrical polarizability, and impedance. These principles must be linked to an external force to re-direct and separate the target cell or biomolecule. Due to the scale of miniaturized separation systems, one can exploit these forces to manipulate single cells or particles in three generalized approaches including continuous kinetic, continuous equilibrium, and elution methods; continuous kinetic methods rely on the rate of cell/particle deflection perpendicular to the main flow; continuous equilibrium methods depend on transportation of cells/particles to their equilibrium positions based on their physical properties; elution methods rely on forces that are antiparallel to the main flow to fractionate cells/particles based on their physical properties.[22]

Early work with sieve like materials indicated that target cells could be isolated from blood samples based on their sizes.[69] In general, since CTCs are significantly larger than normal blood cells[70], [71], separation based on cell size has been achieved using membrane microfilters. These membrane filters consist of an array of microfabricated pores, devised to block the path of the cells above a certain size. This is an example of simple, cost-effective, and efficient method with a high throughput of 0.75 (ml/min) and capture efficiency of ~ 90%.[72] Despite of all the advantages that micro/nanofiltration offer including high throughput and capture efficiency, simple and cost-effective fabrication process, there are some limitations within this method. Although tumor cells are generally larger than normal blood cells, there are some rare CTCs that are smaller or the same size as WBCs.[73] Diversity of CTCs in terms of size within the same population results in an unwanted blocking and contamination of micro-pores, which can locally disrupt the flow and compromise the capture efficiency. At high throughput, this disruption can cause extrusion of target cells through micro-pores which results in lost or damage of the cells.[74]

Combination of nanoporous membranes and electrostatic interactions has shown to enhance nucleic acids separation.[75], [76] Elgort *et al.* demonstrated the separation of genomic DNA (gDNA) using nanoporous aluminium oxide membrane (AOM)-based filtration and surface interactions.[75] Following the same technology, Kim *et al.* integrated nanoporous AOM with microfluidics for nucleic acids separation.[76] The system was tested and optimized under different ionic strength and pH conditions, in addition to various pores sizes.[77]

Flow regimes in microfluidic channels are mainly laminar. Exploiting this property, microchannels architecture can be tuned to control the flow, and direct the target cells or particles, based on their sizes, towards specific stream lines for separation.[78] Pinched flow fractionation is a technique that relies on response of cells or particles to low Reynolds number laminar flows. In pinched flow fractionation, two laminar streams (sample stream with microparticles and buffer stream with no particles) are merged through a narrow channel, known as pinched segment, and then enter a wider channel. The sample stream contains a mixture of micro-particles with two different sizes. Flow rate of the buffer stream is higher than the sample one, which results in microparticles being pushed against the pinched channel wall. Within the narrow region of the channel, larger particles stay further away from the wall while smaller particles remain closer. The laminar flow directs and separates the particles along two different stream lines as soon as they approach the wider channel. Tuning the dimensions of the pinched segment has a significant impact on the device performance and size range of cells or particles that can be separated.[79] One challenge that this method faces is the complex tuning of the pinched segment design in order to separate submicron particles.[78] In addition, Warkiani *et al.* designed an ultra-fast size-based separation platform which exploits hydrodynamic lift forces within a spiral microfluidic channel to separate CTCs.[80] However, this system is not capable of separating cells that are smaller than 12 μm.

Physical barriers within a microchannel such as microgrooves, micro-posts, chevrons, and ridges can be used to separate cells or nucleic acids. In this technique, the separation process takes place by pumping a laminar flow containing the target analytes

through an array of microstructures. For example, cells maneuver through an array of micro-posts oriented using deterministic lateral displacement method.[52], [81] Other researchers have developed separation systems based on physical barriers, size and deformability of biological cells to isolate tumor cells.[82], [83] The geometry and orientation of the micro-obstacles are the key design factors which determine the efficiency of the device but also impose some limitations in terms of cells or particle sizes.

Field-based methods such as acoustophoresis, electrophoresis, dielectrophoresis (DEP), dielectrophoresis field flow fractionation (depFFF), and magnetophoresis, can be applied in microfluidic separation systems. In acoustofluidic systems, an acoustic pressure wave is applied to sort target cells, particles, or their complex based on their sizes.[81] The magnitude of the acoustic force relies on three properties of the target object including its volume, density of the object relative to the fluid, and compressibility of the object relative to the fluid.[84] The separation can be achieved by applying a stationary mechanical wave over the cross-section of a microchannel. This method has been utilized for separating platelets from peripheral blood progenitor cells, for concentrating cancer stem cells (CSCs) from WBCs, and for high-throughput isolation of live cells from non-viable cells.[42], [85], [86] In spite of all promises that acoustophoresis holds, this method is not capable of isolating small nanoscale particles or analytes, since the acoustic force is proportional to the volume of the target object. In addition, the fabrication and integration of an on-chip micro-actuator at the proximity of a channel can be a tedious task.

Electric fields have been widely exploited in chip-based separation of cells or biomolecules of interest. Huang *et al.* combined the physical barriers and an electric field

in one platform to separate charged molecules such as DNA. The system was operated by applying a DC electric field, diagonally and parallel, to an array of micro-posts. By constantly altering between the parallel and diagonal fields, the DNA molecules were separated based on their molecular weight.[87] Free-flow electrophoresis and isoelectric focussing are other types of electrophoretic force-based separations. In free-flow electrophoresis, charged analytes are exposed to a laminar flow and a homogeneous electric field perpendicular to the flow. The electrophoretic force deflects and separate the charged molecules, based on their charge-to-size ratio, whereas uncharged analytes continue following the flow. In free-flow isoelectric focusing, a pH gradient is formed across the separation chamber while a heterogeneous sample containing amphoteric molecules, such as proteins, is pumped into the chamber perpendicular the electric field. When the target amphoteric molecule reaches at a location where there is a difference between the pH and its isoelectric point, it experiences a net charge, and therefore an electrophoretic force. The target molecule moves along the electric field direction until it approaches a point where the pH is equal to its isoelectric point. The net charge of the molecule is now zero, thus it becomes focused at its isoelectric point, and moves in the direction of the flow.[78] The main limitation of electrophoresis is that it can only separate charged objects due to homogeneity of the electric field. Uncharged analytes, particles or cells can be separated using an AC electric field (DEP).

DEP is another electric field-based separation technique. In presence of an inhomogeneous electric field, cells or particles become polarised with one side of the dipole experiencing different electrostatic force than the other side. This non-zero net force results

in movement of cells or particles toward or away from the electric field maxima. Positive DEP happens when the particle/cell is more polarised than the surrounding medium, directing the polarized target towards the field maxima. When the cell/particle is less polarisable than the medium (negative DEP), the target is forced away from the field maxima towards its minima.[78] This label-free technique creates the opportunity to non-invasively separate subpopulations of cells from other cells within a heterogeneous sample exploiting the intrinsic dielectric differences between cell types.[81] However, the main drawback of this technique involves its lack of practicability to be applied on a real clinical sample where the concentration of the target cell (e.g. CTC) is low.[88] Moreover, due to inadequate variation in cell sizes, structures, and DEP potentials, this technique is not sensitive enough to be applied in clinical or POC applications.[89] To overcome some of these limitations, DEP forces have been combined with drag forces to fractionate a heterogeneous sample. This technique is called the dielectrophoresis field flow fractionation (depFFF). It has been shown that depFFF is able to recover up to 90% of CTCs within blood.[90], [91] Another limitation of DEP-force based separation is related to its complex, time-consuming, and expensive fabrication process. This issue has been addressed using optically-induced DEP (ODEP), which provides a facile and rapid generation of electrode layout via controlling light patterns, where optical images are employed as virtual electrodes to generate DEP forces.[81] Chiu *et.al.* have exploited a commercially available digital projector to create optical electrodes on a microfluidic system to control and manipulate cells movement via a computer interface.[92] One general drawback of DEP-based separation technique arises from the fact that cytoplasmic and

membrane conductivities and relative permittivity may change over the course of the sorting process.

1.1.3 Introduction to On-Chip Manipulation of Magnetic Particles

Magnetic micro/nanoparticles have long been applied in bioanalysis for many applications including cell separation, immunoassays, and nucleic acid purification. The benefits that magnetic separation offer include: (i) selective binding of biomolecules to the MP surface based on molecular recognition, (ii) selective separation of MPs from a heterogeneous sample using an external magnetic force, and (iii) its non-invasive nature to maintain cell viability for further analysis. In addition, MPs are readily available in various size range, starting from few nanometres to tens of micrometers. The core of magnetic particles is usually composed of polymer or silica matrix impregnated with iron oxide nanoparticles. The surface of MPs can be activated with functional groups or biomolecules using well-established protocols. Moreover, surface charges, ionic strength, and pH of the sample solution do not affect the magnetic force that each particle experiences.[93], [94] Magnetic separation can be as easy as applying a permanent magnet to the wall of a test tube carrying MPs suspension, followed by discharging the supernatant. However, due to the macroscale setup and relative homogeneity of the magnetic field, separation of magnetically tagged cells or biomolecules using this technique is rather slow. Therefore, it is preferable to miniaturize magnetic separation systems and create regions of high magnetic field gradient, where MPs can be trapped.[95] In the past couple of decades, there has been a rising interest in developing miniaturized on-chip magnetic separator due to the promise they hold in terms of automation and integration with LOC devices. Several

technologies have been developed to enhance the performance of chip-based magnetic separation. These technologies are classified and reviewed as follows.

On-chip magnetic separation devices are typically categorised into three main groups: (i) passive, (ii) active, and (iii) hybrid active-passive devices.[96], [97] Passive systems employ nano/micro-structured ferromagnetic materials, which focus or direct magnetic field lines when magnetized by an external magnet.[29], [98], [99] Active magnetic devices generate localized magnetic field gradients by using current-carrying electromagnets.[43], [100], [101] These active and passive platforms can be integrated into one device, in which ferromagnetic structures are magnetised using an active electromagnet.[97], [102], [103] In the next few paragraphs, a literature review of the magnetic devices with specific examples will be discussed.

In general, passive devices consist of microfabricated ferromagnetic structures, such as nickel or nickel-iron alloys. When these ferromagnetic features are exposed to an external magnetic field, they become magnetized, which results in capturing or deflecting target magnetic objects in a continuous flow. Inglis *et al.* reported a passive silicon-based microfluidic separation platform composed of microfabricated nickel strips which apply a lateral magnetic force on MPs in a continuous flow for cell isolation.[27] Guo *et al.* integrated the patterned nickel strips with magnetic traps for highly selective separation and on-chip detection of foodborne pathogens such as salmonella typhimurium from a heterogeneous sample. When the complex mixture flows over the patterned nickel strips in the separation chamber, the magnetically labeled pathogens are exposed to a lateral magnetic force, which leads them towards the detection zone. Within the detection

chamber, magnetically tagged pathogens move through an array of square-shaped nickel structures, where magnetic force is much larger than the hydrodynamic drag force, and thus they are captured between the nickel structures. Finally, other fluorescent molecules are added to the detection chamber creating a sandwich immune complex for on-chip fluorescent detection. This microfluidic separation system enhances the enrichment of target pathogens, reduces the nonspecific adsorption, and the on-chip detection decreases the sample lost, which results in high sensitivity.[28] As it was mentioned before, creating regions of high magnetic field gradient results in generation of larger magnetic force. It has been shown that creating high aspect ratio nano/microscale ferromagnetic structures within a microfluidic channel can improve the magnetic field gradient.[29], [30], [104] Xia *et al.* reported two different permalloy microstructures (micro-comb and micro-needle) to create regions of high magnetic field gradient. Using this system, magnetically tagged living E. coli bacteria were efficiently isolated from a continuous flow containing unlabelled red blood cells. Comparing these two permalloy microstructures, micro-needles focuses the magnetic field lines at the tip of the needles which is useful for capturing an individual MP or magnetically labelled cell, while the micro-comb generates a broader magnetic field gradient along the channel length and thus influences the trajectories of magnetically tagged objects and separates them somewhere along the channel.[104] One limiting factor of all these silicon/glass-based passive devices is their complex and expensive fabrication process, which make them not convenient for low- and mid-volume manufacturing. To overcome this limitation, Nawarathna *et al.* reported a rapid prototyping technique to fabricate polymer-based separation system composed of integrated nanostructured nickel

magnetic traps to isolate MPs. It was demonstrated that these passive devices could separate target analytes at the flow rate of up to 250 µl/min.[29] This polymer-based magnetic trap is an example of a robust, rapidly prototyped and simple passive device. Despite of facileness in operation of miniaturized passive devices, their dependence on external magnets makes the automation and integration process a tedious task. A programmable magnetic separation system that can capture and release MPs in an automated fashion is an essential component of a fully-integrated LOC device.

Miniaturized current-carrying wires can also generate regions of high magnetic field gradient. These active devices are typically composed of planar micro-coils, that generate localized magnetic field gradients when an electric current is applied. The geometry of a micro-electromagnet can be as simple as a bent wire (Figure 1.2a) or a single current loop (Figure 1.2b).[105] Dubus *et al.* developed a loop-shaped electromagnet to capture 2.8 µm DNA probe modified MPs by applying a current of up to 300 mA.[106] Despite the design simplicity, in order to generate a sufficient magnetic force, this device requires a relatively high current (>100 mA). Therefore, this design is not an appropriate choice to be used in a POC environment, due to its bulkiness (power supplies and cooling system) and extreme Joule heating.

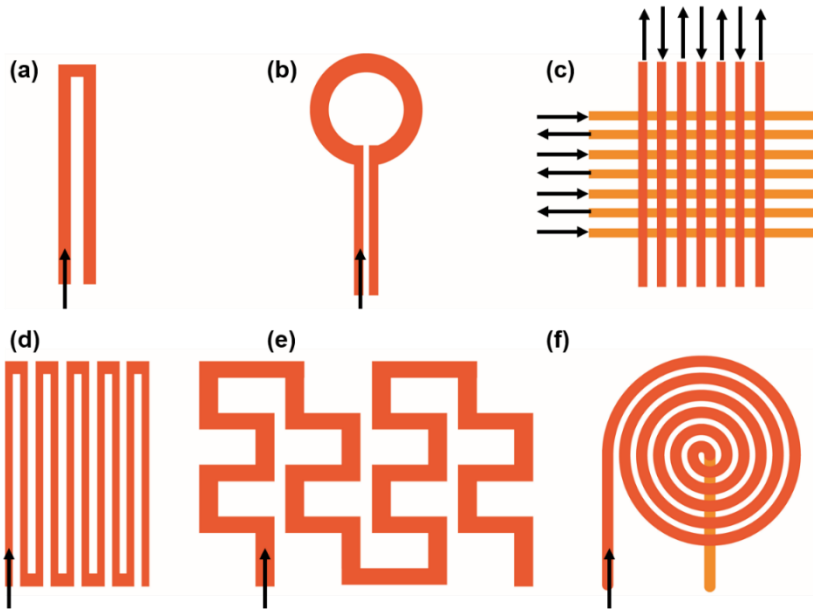

Figure 1.2 Schematic diagrams of common micro-electromagnet designs, arrows show the direction of the applied currents. (a) bent-wire, (b) single-loop, (c) conductor matrix, (d) serpentine, (e) mesh-shaped meander, and (f) spiral. Reprinted from Journal of Magnetism and Magnetic Materials, Vol. 281, Qasem Ramadan, Victor Samper, Daniel Poenar, Chen Yu, On-chip micro-electromagnets for magnetic-based bio-molecules separation, Pages No. 150-172, Copyright (2004), with permission from Elsevier. Adapted by permission from Springer, Microfluidics and Nanofluidics, Customized trapping of magnetic particles, Qasem Ramadan Daniel P. Poenar, Chen Yu), Copyright (2009). Reprinted from H. Lee, a. M. Purdon, and R. M. Westervelt, "Manipulation of biological cells using a microelectromagnet matrix," Appl. Phys. Lett., vol. 85, no. 6, p. 1063, with the permission of AIP Publishing, Copyright (2004).

Other researchers reported more complex designs, with multiple overlaid metallic layers or more turns, to be able to generate larger magnetic field gradients at lower applied currents. Lee *et al.* reported a multi-layer silicon-based micro-electromagnet matrix composed of two arrays of conductors overlaid perpendicular to each other (Figure 1.2c) to capture and manipulate MPs with a diameter of 1–2 μm with an applied current of up to 150 mA.[107], [108] The direction of current in this design has large impact on the magnitude of the generated magnetic field. Due to addition of magnetic field lines between two adjacent conductors with opposite current directions, antiparallel currents through two

neighbour wires generate a significantly larger magnetic field than parallel currents.[109] By programming the current in each conductor, the electromagnet can generate static or dynamic magnetic field hot spots in each square gap between the conductors to continuously capture, separate or combine suspended MPs.[108] One drawback of this design is its complex multilayer microfabrication process. Following the same idea of adjacent wires with opposite direction of current, researchers have introduced other designs consisting of only one layer of current-carrying conductor, while improving the generated magnetic force.

Ramadan *et al.* performed a thorough study on planar current-carrying micro-electromagnets, emphasizing on the effect of different geometries (e.g. serpentine and mesh-shaped meander designs) and magnetic coupling between wires or semi-loops on the magnetic flux density and field gradient.[103], [109], [110] A serpentine, also being referred as straight-conductors meander micro-electromagnet, shown in Figure 1.2d was developed from cascading an array of parallel bent conductors. This serpentine-shaped electromagnet generates a periodic magnetic field gradient distribution profile just above the surface, which oscillates between its maxima and minima. The reason behind this periodic behaviour is the coupling of the magnetic field components between neighbour conductors. However, this coupling is insignificant between the conductors that are further away from each other, and thus extending the device does not improve the magnitude of the magnetic force. Moreover, the magnetic field profile becomes more symmetric in case of even number of conductors, while the magnetic profile shifts toward one side of the device when odd number of wires are used.[109] Ramadan *et al.* also reported a mesh-

shaped meandering design (Figure 1.2e), consisting of a cascaded array of semi-loops. Each semi-loop is composed of three-conductor segments, and as the current passes through them, magnetic field components add up constructively within each semi-loop, which results in generation of localized magnetic potential wells. Ramadan *et al.* studied and compared both the serpentine and mesh-shaped meander designs numerically and experimentally. It was illustrated that mesh-shaped meander design generated higher magnetic force in comparison to the serpentine-shaped device, due to the coupling of the magnetic field lines produced by the three conductor segments in each semi-loop. Due to its structural simplicity (only one patterned conductor layer), the mesh-shaped meander design can be easily implemented and integrated in a microfluidic system.[110] Liu *et al*. utilized a similar meander-shaped micro-electromagnet to capture and concentrate RNA-coated MPs within a microfluidic reaction chamber with minimum applied current of 40 mA. In addition to RNA enrichment, the resultant Joule heating was exploited to enable a reverse-transcription process at constant temperature.[111] In this thesis, we adapted the mesh-shaped meander design as the active component of the proposed magnetic separation device.

Spiral micro-electromagnets (Figure 1.2f), are typically composed of a curled-up conductor with even spacing between adjacent turns.[109] The generated magnetic field, using these devices, is distributed radially such that the magnetic force is strongest at the center of the spiral micro-coil. Fulcrand *et al*. presented a silicon-based spiral micro-electromagnet to trap a batch of 2.8 µm MPs passing in the vicinity of the micro-coil with a flow rate of 1 µL/min by applying a current of 80 mA. In addition, they were able to

redirect MPs to a specific outlet by cascading multiple spiral micro-coils within a microchannel.[112] In compare to mesh-shaped meander design, spiral micro-electromagnet can generate a higher magnetic force due to spirals coupling, however its fabrication process is more complex (requires a second metal layer).[110]

Active devices hold great promise for integration into chip-based biosensors due to their ability to control the movement of MPs more precisely. Magnetic forces are large in the proximity of the micro-electromagnets and decay rapidly as moving away from the coil into the channel. One way to enhance the magnetic force at further distances from the coil is to increase the applied current. However, since the magnetic field intensity is directly proportional to applied current, thus magnetic field generated by an active device is limited by Joule heating and power supplies. Joule heating can create damage to the device and sample solution, if it is not controlled. Moreover, most of the reported active devices were fabricated using complex and expensive lithographic techniques, which are not ideal for low volume prototyping needed in research stages of product development.[106], [113], [114]

Active/passive devices use combination of planar micro-electromagnet and ferromagnetic materials isolated by insulating layers to improve the magnetic field gradients.[97], [102], [103] Choi and Ahn have been laying down the ground work in this field. They developed a number of silicon-based integrated micro-electromagnets including serpentine[115] and spiral[116] micro-electromagnets semi-encapsulated with permalloy. In case of the serpentine design, first antibody-coated MPs (with average dimeter of 1 μm) were injected through the microchannels and captured at the surface of the micro-

electromagnets with an applied current of 30 mA. Next, a heterogeneous sample containing target antigen was flown through the microchannel and the target protein was isolated by specific binding with the antibody coated MPs. Once the binding event was completed, a wash buffer was flown into the channel to clear away any free analytes. The maximum average fluid velocity at which the micro-electromagnet could hold the MPs without losing them in the washing solution was measured to be ~ 1 mm/s.[115] It was also shown that by using a spiral micro-electrograms semi-encapsulated with permalloy, it is possible to capture MPs in a continuous flow by applying a DC current of 300 mA for 10-30 seconds.[116] The fabrication of the devices presented by Choi *et. al.* involves complex and time-consuming steps such as photolithography, lift-off process, and back-side silicon etching, which are not suitable for low- and mid-volume manufacturing. In addition, to trap the MPs in a continuous flow they had to increase the current up to 300 mA, which can be problematic in terms of Joule heating and power supply. Song *et al.* demonstrated a multilayer active-passive magnetic device to separate magnetically tagged cells while exploiting the Joule heating to maintain the temperature of the device around the biocompatible point (~37 °C). The device was composed of six spiral micro-electromagnets, semi-capsulated with electroplated nickel, which were fabricated onto the backside of a silicon wafer. Two microfluidic systems were developed for this device, one used for magnetic cell separation and the other used to dissipate a fraction of the generated heat by the electromagnets.[117] Despite the high capture efficiency (up to 92.4%) offered by this platform, its high current requirement (up to 1.5 A) makes this device not suitable for POC applications.

1.1.4 Lubricant-Infused Slippery Surfaces

In general, when an object shrinks in size, its volume shrinks with higher rate than its surface area. Thus, body forces such as gravity become insignificant, while surface forces such as adhesion and friction become dominant.[118] This phenomenon applies to miniaturized LOC devices, where surfaces come in physical contact with biological fluids (e.g. blood) that are composed of complex matrix of cells and proteins. Therefore, for a LOC microfluidic device to function properly in a POC diagnostic setting, these surfaces must be physically and/or chemically modified to reduce the non-specific adhesion of cells or proteins and consequently preventing the blockage of the microfluidic channels. Lubricant-infused coatings, developed based on locking biocompatible lubricants onto self-assembled monolayers (SAMs) of hydrophobic organosilanes have shown great promise to lessen the non-specific adhesion.[119], [120] Wong *et al.* introduced the first lubricant-infused surfaces where a lubricant layer was tethered on the surface using a combination of physical and chemical surface modification.[121] Leslie *et al.* developed lubricant-infused fluorosilanized surfaces that were exclusively based on chemical modification.[122] Both the chemical (e.g. fluorosilanization) and physical (e.g. inducing micro/nanotextures) alterations increase the hydrophobicity of the surfaces.[123] Due to their excellent self-cleaning properties,[124] these surfaces have been implemented in many applications such as enhancing the mobility of droplets during acoustic actuation,[125] corrosion protection,[126] production of slippery, ice-phobic,[127] and biofouling-resistant surfaces.[128] In chapter 6, we present the development of micro/nano-structured lubricant-infused gold surfaces that are conductive, electrochemically active, and slippery.

These surfaces are capable of attenuating blood coagulation and biofouling due to their low adhesion properties, ideal for integration with LOC devices, where non-specific adhesion and clotting are the main challenges.

1.2 Motivation

Over the past two decades, development of fully-integrated miniaturized on-chip magnetic devices for separation of magnetically tagged cells or biomolecules have drawn an enormous research and commercial interest. Despite of all promises that these chip-based magnetic systems offer, a vast majority of them require external magnets (passive) or relatively high electric currents (active) to operate. Limited control over the manipulation of MPs and lack of integrability are the drawbacks of using passive devices. Active devices offer more controllability over localizing the magnetic field gradients by programing the operational current using handheld digital systems. Combining current-carrying micro-coils (active element) with ferromagnetic structures (passive element) on a single chip have shown to enhance the generated magnetic force. However, this magnetic force is only effective where MPs are at the vicinity of the device surface; it decays rapidly as we move away from the surface of the magnetic device into the sample solution. One way to compensate for the lost in the magnetic force is to increase the applied current; however, high electric current requirement is problematic because it means that there are needs for bulky power supplies and integrated cooling systems to regulate the device temperature, which makes the design and fabrication of these active-passive devices more complex and not suitable for POC applications. Another solution is to actively transport the suspended MPs toward the regions of high magnetic field gradient by using microfluidic techniques,

and magnetically capture or redirect them using a low-current operated hybrid active-passive device. In addition to microfluidic techniques, temperature gradients have been exploited as a transport mechanism to deliver particles or analytes to the detection sites by means of natural advection or thermophoresis.[45], [47], [48] However, temperature gradients have not been combined with magnetic field gradients to direct and capture MPs using on-chip micro-electromagnets.

In addition, even though many silicon-based hybrid active-passive devices have been developed, their complex, time consuming and expensive fabrication processes make them not suitable for low- and mid-volume manufacturing such as research laboratories. Rapid prototyping can provide a facile, economical, and accelerated path to prototype and optimize these microfluidic magnetic devices in the developmental cycles. Rapid prototyping has been used previously to prototype polymer-based passive magnetic devices,[29] However, to my best knowledge, it never being applied for fabricating current-controlled on-chip magnetic devices.

The main motivation behind this thesis is to conquer the drawbacks of the current on-chip magnetic separation technologies, including the requirement for external magnets, high applied current, and complicated, expensive, and time-consuming fabrication steps. To achieve these goals, we aim to develop a miniaturized active-passive on-chip magnetic separation platform on shrinkable polymeric substrates using lithography-free benchtop techniques including xurography, wrinkling, spin coating, and electrodeposition. Combination of wrinkled current-carrying conductors with thin film ferromagnetic materials can enhance the generated magnetic force while keeping the applied current

relatively low (~30 mA). Moreover, we look to understand the effect of Joule heating on the motion of fluids and apply the generated temperature gradient to drive the suspended MPs toward the capturing sites. Finally, we aim to integrate these rapidly prototyped magnetic devices with microfluidics to separate magnetically tagged cells in a continuous flow.

One of the challenges of working with body fluids is the non-specific adhesion of cells or proteins to the device and channel surfaces. In addition, higher magnetic force is required to separate a tagged cell from a complex sample such as blood due to its high viscosity. We investigate different surface treatment techniques to reduce the non-specific adhesion of cells or proteins to the surface of the magnetic device when dealing with more complex samples such as blood. This leads us into developing conductive lubricant-infused nanostructured surfaces (CLINS), which can be used in multi-purpose applications including, surface-based magnetic droplet manipulation, electrochemical-based biosensors, or other medical devices where the CLINS come in direct contact with complex biological samples. Like the active-passive magnetic devices, we aim to fabricate the CLINS on shrinkable polymers using techniques such as xurography, wrinkling, electrodeposition, and chemical vapor deposition (CVD). The hydrophobic slippery properties of CLINS come from the combination of micro/nanostructured conductive material with perfluorinated lubricant-infused coatings. To better understand the physical and chemical properties of CLINS, we look to characterize them using X-ray photoelectron spectroscopy (XPS), contact and sliding angle measurements, magnetic micro-droplet manipulation, and

electrochemical methods. Moreover, we seek to assess CLINS hemocompatibility using human blood plasma.

1.3 Objectives

The objectives of this thesis are summarized below:

A. Rapid and inexpensive prototyping of multi-scale micro-electromagnets for capturing MPs

Cost of fabrication and operational power must be minimized for a micro-electromagnetic separation device to be utilised in a real-world application. By using computer simulations and benchtop prototyping techniques, we explore the possibility to design and fabricate micro-electromagnets on polystyrene (PS) substrates. Through a numerical modeling software, we simulate multiple electromagnet designs and select the best one based on the generated magnetic force, operational current, and ease of fabrication. We also look at simulating the effect of micro/nanotextured current-carrying conductors on the device performance. We explore benchtop fabrication techniques such as xurography, polymer-based thin metallic film wrinkling, spin coating, and electroplating to prototype the simulated active-passive magnetic device. To verify the functionality of the device, we design experiments to capture suspended MPs upon application of relatively small currents (< 50 mA).

B. Device optimization and understanding the physics of operation

In general, one limitation of micro-electromagnet is that at relatively low currents, the generated magnetic field is weak and thus the induced magnetic force attenuates quickly

moving away from the device surface. Through numerical modeling, we explore the effects of the conductor widths and permalloy geometry (patterned permalloy) on the generated magnetic force and propose the optimum dimensions and geometry for fabrication. Moreover, we study the combined effects of thermal gradients, as a result of Joule heating, and magnetic field gradients on the movement of MPs to be able to transport and capture MPs that are further away from the device surface. To verify the simulation results, we design multiple experiments to measure the terminal velocities of magnetic and non-magnetic beads at different distances from the magnetic hot spots. This study provides the rationale behind designing a thermo-magnetic system, which applies temperature gradients to drive MPs towards the magnetic traps and captures them using the generated magnetic force.

C. Capture and release of magnetically labeled cells in a continuous flow using the benchtop fabricated micro-electromagnet

Capture and release of magnetically labelled cells in a continuous flow can be used for separation or concentration of rare cells. By electroplating the permalloy layer, with high relative permeability and low magnetic coercivity, in the vicinity of the current-carrying micro-electromagnet, the device can generate localized high magnetic field gradients around the edges of the permalloy, and thus capturing the magnetically tagged cells in a continuous flow at a relatively low current (~30 mA).

D. Development of conductive lubricant-infused frictionless surfaces to attenuate non-specific adhesions

Separation of magnetically labelled cells from a complex and high viscosity physiological samples such as blood, using the benchtop fabricated magnetic device is challenging due to non-specific adhesion and high magnetic force requirement.[129] This lead us to explore a lubricant-infused coating which enhances the self-cleaning and slipperiness of the device and channel surfaces. The principle of this lubricant-infused coating is based on locking biocompatible lubricants onto self-assembled monolayers (SAMs) of hydrophobic fluorosilane. To verify the slipperiness of these lubricant-infused surfaces, we measure the sliding angle of these surfaces. Furthermore, by combining these surfaces with passive magnetic actuators we manipulate superparamagnetic microdroplets in a frictionless and open channel setting. To examine the self-cleaning property of these surfaces, we explore their resistivity against protein adhesion using a human plasma coagulation assay. In addition, these conductive lubricant-infused slippery surfaces are characterized electrochemically to assess their utility in applications where charge transfer between the surface of electrode and redox species in the solution is required.

1.4 Overview

In this thesis, the theory behind magnetic separation and associated scaling laws are discussed. Next, it focuses on the development and characterization of benchtop fabricated multi-scale micro-electromagnets for capturing MPs. It is demonstrated that temperature and magnetic field gradients are responsible for transporting and trapping the MPs. It is shown that by integrating these magnetic devices with microfluidics, one can capture and release magnetically labelled cells in a continuous flow with an applied current of 30 mA. Lastly, this thesis looks into development and characterization of slippery

electrochemically-active lubricant-infused micro/nanostructured surfaces, capable of attenuating and delaying blood coagulations.

Chapter 2 provides background information on the theory of magnetic separation, including magnetism, properties of magnetic particles, physics behind magnetic separation in miniaturized microfluidic device, the effect of magnetic and other forces acting on MPs, and the scaling laws associated with them.

Chapter 3 focuses on the numerical modeling and the rapid prototyping process for creating a polymer-based micro-electromagnetic device that satisfies both requirements of low power consumption and low-cost fabrication. It is shown that coupling the ferromagnetic layers with current-controlled planar coil is essential for generating a sufficient magnetic force for MP manipulation at low currents (<50 mA). In addition, it is demonstrated that current-carrying conductors created from micro/nanotextured materials further enhance the generated magnetic force at a given current. We develop a benchtop fabrication process based on xurography, polymer induced thin film wrinkling, and electrodeposition to create a multilevel arrangement of multi-scale materials essential for low-current operation. We demonstrate that the fabricated active-passive devices featuring wrinkled copper active layers and permalloy passive layers can capture 2.8 μm MPs upon the application of a 35-mA current. These devices are ideal for addressing the rapid prototyping needs of industry and academic researchers as new device geometries can be created from design to fabrication in a matter of hours.

Chapter 4 concentrates on understanding the combined role of temperature and magnetic field gradients on the movement of MPs in order to extend the interaction distance

of on-chip magnetic devices beyond the device vicinity. We apply the developed rapid prototyping method in Chapter 3 to fabricate an active/passive on-chip electromagnet with a micro/nano-structured active layer and a patterned ferromagnetic passive layer. Through numerical modelling and experiments, we demonstrate the enhanced fluid movement is caused by the thermal gradient. This study enables the rational design of thermo-magnetic systems for thermally driving and magnetically capturing MPs that are positioned at distances tens to hundreds of microns away from the edges of on-chip magnetic devices.

Chapter 5 focuses on integrating the previously developed benchtop-fabricated active-passive magnetic device with microfluidic flow to capture and release magnetically labelled yeast cells in a continuous flow with an applied current of 30 mA. This study indicates the possibility of using these platforms for separation of rare cells such as CTCs.

Chapter 6 looks into fabrication and characterization of conductive electrochemically active lubricant-Infused nanostructured surfaces capable of attenuating the non-specific adhesion of proteins or cells and enabling friction-less droplet manipulation. These surfaces provide slippery and conductive interfaces for LOC applications. In addition, they are capable of resisting blood coagulation and biofouling due to their low adhesion properties, which is essential for LOC applications that deal with complex body fluids. Furthermore, the integration of a permalloy layer enables long-range frictionless actuation of superparamagnetic droplets, ideal for droplet-based LOC devices.

Chapter 7 focuses on the conclusions of this research, providing a summary of the main findings and their contributions to development of microfluidic magnetic bio-

separators. Lastly, the limitations of the current findings and the anticipated future works are discussed.

Chapter 2 Background on Theory of Magnetic Separation

This chapter starts with an introduction to magnetism followed by reviewing the properties of MPs. The physics behind magnetic separation in miniaturized microfluidic device is studied, including the effect of magnetic and other forces acting on MPs, and the scaling law associated with them.

2.1 Introduction to Magnetism

Magnetism is a property of materials that its origin lies in intrinsic behaviour of electrons, including: spin motion of the electron around its own axis and orbital motion of electron around the nucleus. There is also a quantum exchange force, which is responsible for aligning (parallelizing or anti-parallelizing) the magnetic moments in adjacent atoms. Therefore, each atom contributes independently to the total magnetic moment (***m***). Since the magnetic moment of electrons with spin down are canceled by ones with spin up, just unpaired electrons are responsible for magnetism in materials. All materials are affected by the presence of an external magnetic field to some extent depending on their magnetic properties. When a substance is exposed to an external magnetic field of strength ***H*** (A/m), the interaction between each individual magnetic dipole moment and the external magnetic field contributes to the material's overall response, inducing magnetic field lines within the material.[130] Depending on the magnetic property of a material, magnetic field lines can reach a specific density within the material, quantified by the magnetic permeability of that specific material, μ (Vs/Am). The magnetic flux density, ***B*** (Tesla or T), represents the number of magnetic field lines per unit area:[131], [132]

$$\boldsymbol{B} = \mu_0(\boldsymbol{M} + \boldsymbol{H}) \tag{2.1}$$

where μ_0 is the magnetic permeability of free space ($4\pi \times 10^{-7}\ Vs/Am$), and $\boldsymbol{M}$ (A/m), the total magnetic moment per unit volume ($\frac{\boldsymbol{m}}{V}$) represents the magnetization induced in a material by $\boldsymbol{H}$:

$$\boldsymbol{M} = \chi \boldsymbol{H} \tag{2.2}$$

where χ is the dimensionless proportionality constant, known as the volumetric magnetic susceptibility, which is unique for each material. The maximum magnetization or saturation magnetization ($\boldsymbol{M_s}$) is reached when all the magnetic moments are aligned with the external field. Combining equations (2.1) and (2.2):

$$\boldsymbol{B} = \mu_0(1 + \chi)\boldsymbol{H} \tag{2.3}$$

where $1 + \chi = \mu_r$ is the relative permeability of the material.

In general, materials are classified in two main groups, based on their magnetic properties: (i) The materials with no permanent magnetization which display a linear response to a modest applied field, including diamagnetic, paramagnetic or antiferromagnetic materials, (ii) and the ones with intrinsic magnetization which express a nonlinear response to the applied field, including ferromagnetic and ferrimagnetic materials.[130] Diamagnetic materials ($\chi < 0$) are repelled from maxima of the magnetic fields strength. Majority of materials and biomolecules are slightly diamagnetic (or in other word non-magnetic), such as water, wood, glass, polymers, proteins, DNA, and cells. Paramagnetic materials ($\chi > 0$) such as oxygen, platinum and manganese (II) salts, are attracted towards magnetic field maxima with small force. Ferromagnetic materials such as iron, cobalt, nickel, and their compound with rare earth elements have an intrinsic magnetization ($\chi >> 0$), and are strongly forced toward maxima of magnetic fields.[133]

2.2 Properties of Magnetic Particles

The irreversibility in the magnetization process of non-linear magnetic materials results in generation of hysteresis loops in M-H curves. This hysteresis M-H response is observed in larger ferromagnetic particles with multi-domain structures generated by regions of homogeneous magnetization isolated by domain walls. The hysteresis curves are associated with the energy balance due to the motion of the domain wall between adjacent magnetic domains when the temperature and/or applied magnetic field are varied, which results in disturbing the alignment of the magnetic moments in the material. The generation of multi-domains ferromagnetic particles becomes unfavorable (no hysteresis curve) if the diameter of the MP is in the same order of magnitude or smaller than the thickness of the magnetic domain wall. Depending on the compound, the width of the magnetic domain wall ranges from ~10 nm to ~130 nm.[43], [134] At a presence of an external magnetic field, these magnetic nanoparticles remain as single domain with one large magnetic moment because the energy is not dissipated by the motion of domain walls. However, when the external magnetic field is removed, their average magnetization returns to zero within a short period of time, known as the relaxation time (τ). τ is the time required for the magnetic moment spin reversal, which depends on the energy barrier between the spin-up and spin-down states, known as easy-axis orientation, and the thermal energy. τ can be calculated using equation (2.4):[130], [135]

$$\tau = \tau_0 \exp(\frac{KV}{k_B T}) \tag{2.4}$$

where K (J/m^3) and V (m^3) are the nanoparticle magnetic anisotropy energy density and volume respectively. Thus, KV is the energy barrier related with the magnetization moving

from its initial state, through a hard plane, to the other easy-axis orientation. k_BT represents the thermal energy, where, k_B and T are the Boltzmann constant and absolute temperature respectively. The pre-exponential factor τ_0 weakly depends on the temperature and is in order of 10^{-10} to 10^{-12} seconds.[95] With sufficiently small MPs, the thermal energy surpass the energy barrier and thus the magnetic moment is quickly reversed to the other easy-axis direction.[130] If the relaxation time is shorter than the measurement time of the experimental technique being used ($\tau << \tau_m$), then these single domain nano-sized MPs are in superparamagnetic regime. Otherwise ($\tau >> \tau_m$), the system is called blocked, and the temperature that defines the midpoint between these two states ($\tau = \tau_m$) is called the blocking temperature (T_b), which depends on the MP magnetic anisotropy energy density, the size of the MP, and the applied magnetic field.[95], [136]

A dispersion of superparamagnetic nanoparticles (typically 5-100 nm in diameter) such as iron oxide crystals can be embedded in a spherical polymer matrix to create a magnetic microparticle which behaves superparamagnetically with a large magnetic moment due to the cumulative effect of the planted superparamagnetic nanoparticles.[136], [137] The combination of high $\boldsymbol{M_s}$ and superparamagnetism makes these MPs an optimum choice to be used as magnetic carriers. They are strongly attracted to the magnetic field maxima while retaining no residual magnetism after removing the source of the magnetic force. Turning off the magnetic field spontaneously brings the total magnetic moment back to zero (no magnetic memory), and thus multiple cycles of capture and release are feasible [130], [138] This behavior provides a great degree of controllability over the motion of MPs within microfluidics. The superparamagnetic core of a MP is protected by a shell to

avoid direct contact with the surrounding medium, thus preventing undesired interactions and oxidation. On-chip magnetic separation is conducted by binding specific biomolecules or cells to the MPs and isolating or redirecting them from the sample mixture by imposing magnetic forces. Two examples of superparamagnetic microparticles that are employed throughout this thesis include 2.8 μm carboxylic acid coated Dynabeads M-270 and 1 μm carboxylic acid coated Dynabead MyOne. These uniformly dispersed Dynabeads are composed of superparamagnetic nanoparticles (γFe_2O_3 and Fe_3O_4) embedded in highly cross-linked polystyrene matrix. The MPs are further coated with a hydrophilic layer of glycidyl ether, protecting the magnetic core. The surface of the Dynabeads are then modified with functional groups such as carboxylic acid. The hydrophilic nature of these MPs offers low non-specific adsorption and great dispersion abilities in various buffers. The magnetic susceptibilities of Dynabead M-270 and Dynabead MyOne are calculated from the slope of the magnetization curves to be ~0.17 and 1.5, respectively.[139]–[141]

2.3 Physics of Magnetic Separation

This section focuses on the physics of magnetic separation and main forces involved in the process. To optimize the capture efficiency and throughput of an on-chip magnetic separation device, it is necessary to identify and understand all the forces that a suspended MP can experience, such as magnetic, viscous drag, gravitational, buoyancy, Brownian, lift, thermophoretic, and magnetic interaction forces.[94] The effect of the scaling law on these forces is investigated to determine the dominant forces and their related design criterion.

2.3.1 Magnetic Force

The equation for the magnetic force acting on a magnetic moment (***m***) can be written in terms of gradient in the magnetic energy. Assuming ***m*** is constant:[132]

$$\boldsymbol{F_m} = -\boldsymbol{\nabla}(U_m) = \boldsymbol{\nabla}(\boldsymbol{m}\cdot\boldsymbol{B}) = (\boldsymbol{\nabla m})\cdot\boldsymbol{B} + \boldsymbol{m}\cdot\boldsymbol{\nabla B} \approx (\boldsymbol{m}\cdot\boldsymbol{\nabla})\boldsymbol{B} \tag{2.5}$$

where $\boldsymbol{F_m}$ and U_m are the magnetic force and potential energy respectively. ***m*** can be expressed as:

$$\boldsymbol{m} = V\boldsymbol{M} = V\Delta\chi\boldsymbol{H} \tag{2.6}$$

where V is the volume of the particle and $\Delta\chi = \chi_p - \chi_m$ is the effective magnetic susceptibility of the particle (χ_p) relative to its surrounding medium (χ_m). Non-magnetic fluids such as water have negligible magnetic susceptibilities compared to MPs, and thus $\Delta\chi \approx \chi_p$. Combining equations (2.3), (2.5), and (2.6):[134]

$$\boldsymbol{F_m} = \frac{V\Delta\chi}{\mu_0}(\boldsymbol{B}\cdot\boldsymbol{\nabla})\boldsymbol{B} \tag{2.7}$$

Equation (2.7) implies that a magnetic field gradient ($\nabla\boldsymbol{B}$) is required to capture or manipulate a MP. Homogeneous magnetic fields can only apply torques on MPs but no translational forces.[95], [134] Equation (2.7) assumes that the MP is uniformly magnetised.[142]

2.3.2 Force Balance in Magnetic Separation

In general, the trajectory of a moving spherical MP or MPs-cells/biomolecules complex in a microfluidic laminar flow is estimated by the balance of multiple forces (Figure 2.1), based on Newton's second law:[143], [144]

$$m_p\frac{\partial \boldsymbol{v}}{\partial t} = \boldsymbol{F_m} + \boldsymbol{F_d} + \boldsymbol{F_g} \tag{2.8}$$

where m_p and $\boldsymbol{v}$ are the mass and velocity of the MP (or the magnetically tagged composite), respectively. $\boldsymbol{F_m}$, $\boldsymbol{F_d}$, $\boldsymbol{F_g}$, are magnetic, drag, and gravitational forces, correspondingly.

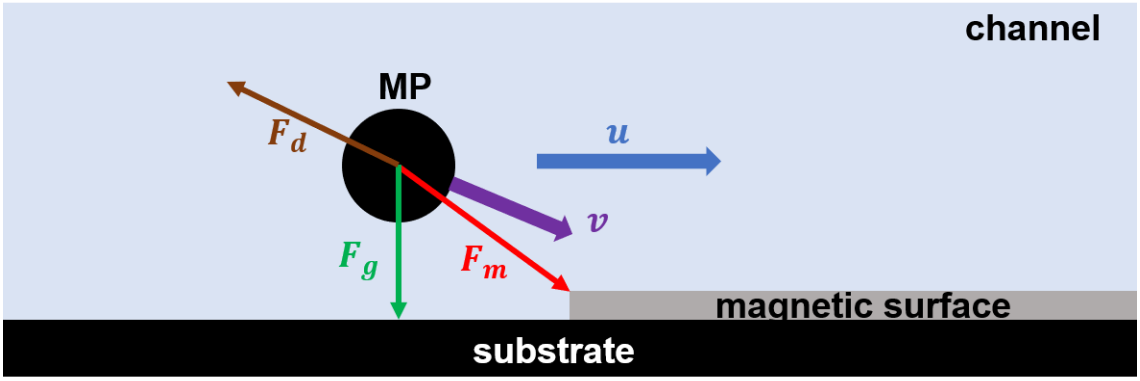

Figure 2.1 Dominant forces acting on a MP and velocity components in a microfluidic magnetic separation device. **u** and **v** represent fluid and MP velocities, respectively. The dimensions are not to scale.

Considering buoyancy, the gravitational force acting on a particle can be calculated as:[94]

$$\boldsymbol{F_g} = -V(\rho_p - \rho_f)\boldsymbol{g} \tag{2.9}$$

where $\boldsymbol{g}$ is the gravitational acceleration, V is the volume of the particle, ρ_p, and ρ_f are the particle and fluid densities respectively. For a spherical particle moving in a laminar flow, the viscous drag force is approximated from the Stokes' law:[43], [144]

$$\boldsymbol{F_d} = 6\pi\eta r(\boldsymbol{u} - \boldsymbol{v})f_d \tag{2.10}$$

where η, r, $\boldsymbol{u}$, $\boldsymbol{v}$, and f_d are dynamic viscosity of the fluid, particle radius, fluid velocity, particle velocity, and drag coefficient respectively. f_d takes into account the effect of a solid wall in the proximity of a moving particle.[145] In microfluidic magnetic separation, the viscous drag force, acting on a MP or a MPs-cells/biomolecules complex, is comprised of two vector components; One is caused by the fluid flow, opposing the flow direction, and the other one is caused by magnetophoresis, opposing the magnetic force direction. The

summation of these vector components results in the net viscous drag force, opposing the overall direction of the spherical magnetic object.[94]

Majority of the works reported in the literature only consider the two most substantial forces: the viscous drag force and the magnetic force.[94] The magnetic force is opposed to the viscous drag force acting on a single MP suspended in a stationary fluid ($\boldsymbol{u} = 0$), and thus the magnetophoretic velocity can be calculated by balancing the equations (2.7) and (2.10):[43], [146]

$$\boldsymbol{v_m} = \frac{2r^2\Delta\chi}{9\mu_0\eta f_d}(\boldsymbol{B}\cdot\boldsymbol{\nabla})\boldsymbol{B} \tag{2.11}$$

Equation (2.11) indicates that the key design parameters for developing a functional magnetic device include size of the MP, difference in magnetic susceptibility of the MP and the surrounding fluid, viscosity of the fluid, generated magnetic flux density, and magnetic field gradient.

In addition to the above-mentioned forces, other forces can be added to the equation (2.8) under certain conditions. These forces include thermophoretic, hydrodynamic lift, Brownian, and particle-particle magnetic interaction forces.[147] However, in microfluidic magnetic separation, the effect of many of the mentioned forces becomes negligible. In the next section, we apply the scaling law to understand the effect of MP size and device dimensions on magnitude of the magnetic force relative to other forces.

2.3.3 Scaling Law in Magnetic Separation

To apply the scaling law on suspended MPs, the particles diameter (d_p) is chosen as the characteristic size. In addition, the dimensionless stability numbers ($S =$

$\frac{\text{magentic potential energy}}{\text{other types of energy}}$) are utilized to estimate the stability of the magnetic potential energy associated with the MP ($U_m = mB = \frac{\pi}{6} d_p^3 MB$) relative to other types of energy, such as viscous drag (E_v), gravitational potential (E_g), thermal (E_{th}), and magnetic dipole potential energy(E_d).[134]

Assuming the fluid is stationary, the viscous drag energy of a moving MP within the fluid can be calculated as:

$$E_v = 3\pi\eta d_p^2 v \tag{2.12}$$

where v is the magnitude of the MP velocity. If the movement of the MP is due to a magnetophoretic force, then the magnetophoretic stability number can be expressed as:

$$S_{mp} = \frac{U_m}{E_v} = \frac{1}{18}\frac{MBd_p}{\eta v} \tag{2.13}$$

, which is directly proportional to the MP diameter. Thus, as the size of MPs decrease, it becomes more challenging to magnetically separate them since the viscous drag force becomes the dominant force.

A suspended MP also experiences a gravitational force. The gravitational potential energy of a MP, located at a distance h from the surface, can be calculated as:

$$E_g = \frac{\pi d_p^3}{6}\left(\rho_p - \rho_f\right)gh \tag{2.14}$$

The ratio between the magnetic and gravitational potential energy is called the sedimentation stability number:

$$S_s = \frac{U_m}{E_g} = \frac{MB}{(\rho_p - \rho_f)gh} \tag{2.15}$$

, which does not scale with the size of the MP since both gravitational and magnetic forces are body forces.

The ratio between the magnetic potential energy and thermal energy of a MP is called the thermal stability number, also known as the Langevin parameter:

$$S_{th} = \frac{U_m}{E_{th}} = \frac{\pi}{6}\frac{MBd_p^3}{k_BT} \tag{2.16}$$

Given the magnetic field intensity, equation (2.16) indicates that downsizing the MP results in a drastic weakening of the magnetic potential energy relative to the thermal energy. As it was mentioned in section 2.2, below a critical dimension, the thermal energy dominates leading the MP to a superparamagnetic regime.

Magnetic dipole potential energy is defined as:

$$E_d = \frac{\mu_0 \pi M^2 d_p^3}{72(\frac{\delta}{d_p}+1)^3} \tag{2.17}$$

where δ is the distance gap between two adjacent MPs. The ratio between U_m and E_d is called the dipole stability number:

$$S_d = \frac{U_m}{E_d} = 12\frac{B}{\mu_0 M}(\frac{\delta}{d_p}+1)^3 \tag{2.18}$$

, which contains two length parameters, d_p and δ. Miniaturizing the size of MPs enlarges the dipole stability number, thus the applied magnetic force becomes the dominant force relative to the magnetic particle-particle interaction force. Moreover, magnetic particle-particle interactions can be ignored for MP suspensions with small volume concentration (large δ).[148] On the other hand, increasing the size of MPs lowers S_d, which results in the dominance of the magnetic dipole interaction force in compare to the magnetic force. A small dipole stability number means that MPs can self-assemble and create supraparticles.[134]

Furthermore, a spherical particle can experience a hydrodynamic lift force, which results in a vector velocity that is orthogonal to the main fluid flow. However, the lift force is directly proportional to the flow velocity and the particle size relative to the channel length, and thus it is only effective at a high Reynolds numbers conditions ($Re_p >> 1$). Dimensionless Reynolds number of a particle is estimated as:[94], [149]

$$Re_p = \frac{inertial\ force}{viscous\ force} = \frac{\rho_f U_p d_p}{\eta} \tag{2.19}$$

where η and ρ_f are the viscosity and density of the fluid respectively. U_p is the particle average velocity. Since the microfluidic magnetic separation mainly operates at low Reynolds number conditions ($Re_p << 1$), thus generally the contributions of the hydrodynamic lift forces on MPs complex are insignificant.

Molecules of a fluid containing suspended particles collide with each other randomly. This can cause an arbitrary motion to the particles, which is called the Brownian motion.[94] The effect of Brownian motion becomes noteworthy as the size of the MP decreases to the nanoscale range. This can be observed from Stokes-Einstein equation:[43]

$$D = \frac{k_B T}{3\pi\eta d_p} \tag{2.20}$$

where D is the diffusion coefficient (m^2/s), which is directly related with the diffusion length $x = \sqrt{Dt}$. t is the diffusion time.

The scaling law can be exploited in design and optimization of miniaturized microfluidic magnetic separators. Equation (2.5) implies that suspended MPs follow the steepest ascent path of the magnetic energy. Thus, the capturing sites for MPs are determined by the spatial resolution of the magnetic field gradients. In case of bulky

magnetic field generating elements (e.g. permanent magnets, ferromagnetic structures or current-carrying wires) relative to the size of the MPs, an aggregation of the MPs are captured at the magnetic traps.[108], [137] By adjusting the dimensions of the magnetic field generating elements within the size range of MPs, it is possible to immobilize an individual MP on a single magnetic element.[150]

As it was mentioned previously, the magnetic flux density generated by a micro-electromagnet can be controlled by adjusting the applied electric current. From Biot-Savart Law, $\boldsymbol{B}$ can be calculated at a distance r from the current-carrying wire:[110]

$$\boldsymbol{B} = \frac{I}{4\pi\mu_0}\int_l \frac{\boldsymbol{dl}\times\boldsymbol{r}}{r^2} \tag{2.21}$$

where I is the applied current, $\boldsymbol{dl}$ is a vector whose magnitude is the length of the differential element of the current-carrying wire and its direction follows the current flow, and $\boldsymbol{r}$ is the displacement unit vector pointing from the conductor element towards the point at which the magnetic field is calculated. Equation (2.21) indicates that the magnetic flux density and magnetic field gradient generated by current-carrying wires are scaled as $\boldsymbol{B} \propto I/L$ and $\boldsymbol{\nabla B} \propto I/L^2$, where L is the characteristic size of the system. Joule heating limits the maximum applied current to $I_{max} \propto L$, thus $\boldsymbol{B}$ is size independent, and $\boldsymbol{\nabla B} \propto 1/L$. By increasing the cross-sectional area of the conductor, a higher electric current can be applied to the micro-electromagnet, which results in an increase in $\boldsymbol{B}$, while reducing the width of the conductor enhances the generated magnetic field gradient. It has been demonstrated that an optimum design can be achieved by increasing the conductor thickness and reducing its width. Using this design approach, one can maintain the desired applied current while enhancing the magnetic field gradient.[110] Typically, fabrication of these micro-

electromagnets involves photolithography, lift off process, and electroplating to increase the thickness of the conductors. In this thesis, we exploit the heat shrinking property of polymer-based micro-electromagnets to reduce the width of the conductor while the resultant stress causes the conductive thin film (100 nm) to crumple, creating relatively tall (>20 μm) micro-wrinkled structures.[97]

2.4 Summary

In this chapter, we reviewed the concept of magnetism including magnetic moment, field intensity, flux density, and susceptibility. Different type of magnetism including diamagnetism, paramagnetism, ferromagnetism, and superparamagnetism were investigated. Next, properties of magnetic materials were studied. Below certain dimensions, generation of multi-domains ferromagnetic particles becomes unfavorable, and nanoscale MPs (superparamagnetic nanoparticles) remain in a single-domain region, only magnetized in the presence of an external magnetic field and shortly become demagnetized when the field is removed. After that, the physics behind on-chip microfluidic magnetic separation was reviewed. The major forces acting on a suspended MP include magnetic, hydrodynamic, and gravitational forces. However, other forces such as thermal, inertial, Brownian, and particle-particle magnetic interaction forces can also have impacts on the overall trajectories of MPs within microfluidic channels, depending on the size of MPs, flow velocity, and channel dimensions. Moreover, the scaling law was utilized to study the effect of other forces relative to the magnetic force acting on MPs.

Chapter 3 Benchtop Fabrication of Multi-Scale Micro-Electromagnets for Capturing Magnetic Particles

Chapter Introduction (Objectives A)

Minimizing the cost of fabrication and operational power is paramount for a micro-electromagnetic separation device to be utilised in a POC application. This chapter focuses on the numerical modeling and rapid prototyping process to create a polymer-based micro-electromagnetic device that satisfies both requirements of low power consumption and low-cost fabrication. Through numerical modeling, we simulate multiple electromagnet designs and select one based on the generated magnetic force, operational current, and ease of fabrication. The effects of the micro/nano-structured surface-coil and its coupling with permalloy structures on the device performance is studied through these simulations. we explore benchtop fabrication techniques such as xurography, polymer-based thin metallic film wrinkling, spin coating, and electroplating to prototype the simulated active-passive magnetic device. To verify the functionality of the device, we design experiments to capture suspended MPs upon application of relatively small currents (< 50 mA). In summary, the polymer-based micro-electromagnetic devices are prototyped using lithography-free benchtop methods. We integrate a variety of multi-scale materials into a single chip and take advantage of the materials properties such as micro/nano-wrinkling to enhance the magnetic force and lower the current requirement. By passing a relatively low current (35 mA) through the micro/nano-structured wrinkled copper micro-electromagnet, we generate a magnetic field, which subsequently magnetizes the permalloy thin film to collect 2.8 µm MPs suspended in an aqueous solution.

Authors: Amin Hosseini and Leyla Soleymani

Publication: Applied Physics Letters, 105, 7, 074102

Publication Date: August 2014

3.1 Abstract

Micro-electromagnets hold great promise for integration into portable and handheld lab-on-a- chip systems applicable to point-of-care disease management. Two major requirements must be satisfied in order for such devices to be applicable into practical, miniaturized, and portable biomedical instrumentation: low power operation and low-cost fabrication. In this paper, we use numerical modeling combined with a lithography-free fabrication process to create micro-electromagnets on a polymer substrate. Numerical modeling reveals that active-passive devices—ferromagnetic layers coupled with current-controlled planar coils—are essential for generating a sufficient magnetic force for magnetic particle manipulation at low currents (<50 mA). In addition, it is shown that current carrying conductors created from micro/nanotextured materials further enhance the generated magnetic force at a given current. To combine low-cost fabrication with low-current operation, we developed a benchtop fabrication method based on craft cutting, polymer induced thin film wrinkling, and electrodeposition to create a multilevel arrangement of multi-scale materials essential for low-current operation. We demonstrate that the fabricated active-passive devices featuring wrinkled copper active layers and

permalloy passive layers capture 2.8 μm magnetic particles upon the application of a 35mA current.

Keywords: permalloy, magnetic fields, copper, microelectromechanical systems, metallic thin films

3.2 Introduction

Recently, there has been a rising interest in the development of chip-based biosensors for point-of-care disease management. In order to detect specific biomolecules suspended in heterogeneous biological samples, functionalized magnetic particles (MPs) are used to filter out biomolecules of interest and suspend them into solutions of desired composition and volume.[136], [151]–[156] In previous reports, functionalized MPs were extracted from solutions[151], [153] using permanent magnets,[95] on-chip magnetized strips, or micro-electromagnets.[43] Although magnetic separation using permanent magnets offers simplicity,[157] on-chip magnets offer miniaturization and automation for use in lab-on-a-chip biosensors.[157], [158] Chip-based magnetic separation devices are categorized into passive and active devices.[96] Active devices induce local magnetic fields by micro-electromagnetic elements, typically, planar coils, when an electric current is applied. Passive devices generally utilize micro/nanoscale ferromagnetic structures to generate high magnetic field gradients when magnetized by an external magnet.

Dubus et al. reported a silicon-based microfabricated active electromagnetic device, where 2.8 μm MPs were trapped by applying a 300 mA current for 5 minutes.[106] In spite of great promise, the high current requirement of this device is problematic due to its reliance on bulky power supplies and generation of excessive Joule heating. Inglis *et al.*

presented a passive silicon device with microfabricated nickel strips to induce lateral forces on MPs for continuous cell-by-cell separation from a flow stream in microfluidic channels.[98] Although this passive device is relatively simple, it requires magnetization by an external magnet, and its magnetic separation lacks controllability. Choi *et al.* devised an active-passive bio-separator with planar electromagnets semi-encapsulated in permalloy for separating MPs by applying a relatively small DC of 30 mA. This device elegantly combined magnetic force tunability with low-current requirements; however, its lithographic fabrication requires complex and expensive processes not suitable for low- and mid-volume manufacturing.[159] To overcome the complexities introduced by lithography-based microfabrication, Nawarathna *et al.* introduced a rapid prototyping method for fabricating nanostructured nickel structures on commercially available shrink-wrap polyolefin films to sort 1 µm MPs from non-magnetic beads.[29] This demonstrates a facile method for prototyping on-chip micro-electromagnets; however, it is an example of a passive magnetic separation device.

Here, we demonstrate an active-passive magnetic separation device that is miniaturized (~1 cm^2) and applicable to lab-on-a-chip systems; operated at a low current (~30 mA); and fabricated using facile, inexpensive, and rapid processes.

3.3 Experimental

3.3.1 Materials

All devices were fabricated on pre-strained polystyrene (PSPS) (55 × 55 mm^2) substrates (Graphix Shrink Film, Graphix, Maple Heights, Ohio). Self-adhesive vinyl (FDC 4304 Easy Removable sign vinyl, BDF Graphics, Toronto, Ontario) were used as the mask

several times during fabrication process. Permanent epoxy negative photoresist SU-8 2007 (MicroChem, Newton, Massachusetts) was utilized as a dielectric layer within the device. Reagents used in preparation of permalloy electrodeposition bath include nickel (II) sulfate hexahydrate ($NiSO_4.6H_2O$, ACS reagent, 99%), boric acid (H_3BO_3, 99.999%), iron (II) sulfate heptahydrate ($FeSO_4.7H_2O$, ACS reagent, ≥99.0%), sodium saccharin ($C_7H_4NNaO_3S.xH_2O$, analytical standard), and sodium dodecyl sulfate ($CH_3(CH_2)_{11}OSO_3Na$, ACS reagent, ≥99.0%), all were purchased from Sigma-Aldrich (St. Louis, Missouri). Milli-Q grade water (18.2 MΩ) was used to prepare all the solutions. Magnetic beads used in the experimental section were 2.8 µm carboxylic acid coated Dynabeads M-270 (Invitrogen, Carlsbad, California).

3.3.2 Fabrication Process

Figure 3.1 shows the side and top view of the fabrication process PSPS sheets were cleaned under orbital agitation for 10 min in isopropanol and water baths and were dried using air stream. Self-adhesive vinyl sheets were laid over the cleaned polystyrene sheets and evenly flattened with a hand roller. The mesh-shaped meander design was created using Adobe Illustrator software and patterned using top-down electrode patterning on PSPS and vinyl masks using a Robo Pro CE5000-40-CRP vinyl cutter (Graphtec America Inc., Irvine, California) equipped with a CB09UA super steel blade, with force, quality and speed set at 10, 1, and 1 respectively. The cut out meandering shape was peeled off from the PSPS film using tweezers. The remaining self-adhesive vinyl was used as a mask during copper sputtering. 100 nm of copper was sputtered from a 99.999% purity copper target (Kurt J. Lesker Company, Concord, Ontario) using a Torr Compact Research Coater CRC-600

manual planar magnetron DC sputtering system (New Windsor, New York) onto the masked polystyrene sheets. The argon (> 99.999% purity, AlphaGaz, Air Liquide, Montreal, Quebec) plasma was created by a DC current of 50 A, which lead to a copper deposition rate, monitored by the quartz crystal thickness sensor, of 0.4 Å/s. After sputtering the vinyl mask was removed manually using tweezers. Copper-coated polystyrene devices were shrunk on an aluminum plate at 150-160°C in an oven (BINDER, GENEQ Inc., Tuttlingen, Germany) for 3 minutes. The devices contact pads were masked with regular tapes and then the surfaces of the devices were cleaned with ethanol and deionised water, dried with a stream of air, and placed on a hotplate at 60°C for 30 minutes. After cooling down the devices at room temperature for a few minutes, the devices were located inside a spin coater (Laurell Technologies, North Wales, Pennsylvania) with its spin speed set to 1000 rpm. Using a regular syringe and after removing all air bubbles from the SU-8 2007 inside the syringe, few drops of SU-8 2007 was added to the surface of the devices. After waiting for 20 seconds, letting the SU-8 to cover the entire surface area, ran the spinner for 30 seconds. The spinning procedure was repeated one more time and the devices were baked at 95 °C on a hot plate for 15 minutes and cooled down to room temperature. After fully curing the SU-8, the tape covering the contact pad was carefully removed using tweezers. A T-shaped design was patterned on the self-adhesive vinyl using Adobe Illustrator and the craft cutter, then peeled off using tweezers, laid over and aligned carefully on the shrunk PS devices leaving the SU-8 covered meandering design exposed through the T-shaped window. Next, 20 nm of silver thin film was deposited on top of the devices using the DC sputtering system with the DC current of 35 A and deposition rate of

1 Å/s. The silver acts as a conductive seed layer for the permalloy electrodeposition. After removing the vinyl, the devices were masked again with the self-adhesive vinyl with a rectangular opening (10 × 1.2 mm) to ensure the same electrochemically active surface area for all the devices. The permalloy electrodeposition was performed using CHI660D electrochemical workstation (CH Instrument, Austin, Texas) and a standard three-electrode set-up. The electrochemical system consisted of an Ag/AgCl reference electrode, a platinum wire counter electrode, and the silver sputtered PS devices as the working electrode. permalloy electrodeposition bath solution consists of 0.95 M $NiSO_4.6H_2O$, 18 mM $FeSO_4.7H_2O$, 0.4 M H_3BO_3, 4.87 mM sodium saccharin, and 0.35 mM sodium dodecyl sulfate. The permalloy plating was performed at room temperature using chronopotentiometry technique with the current density controlled at 5 mA/cm^2 for duration of 44 seconds. Once the plating was completed, the vinyl masks were removed, and the device was rinsed with the deionised water and dried with nitrogen stream.

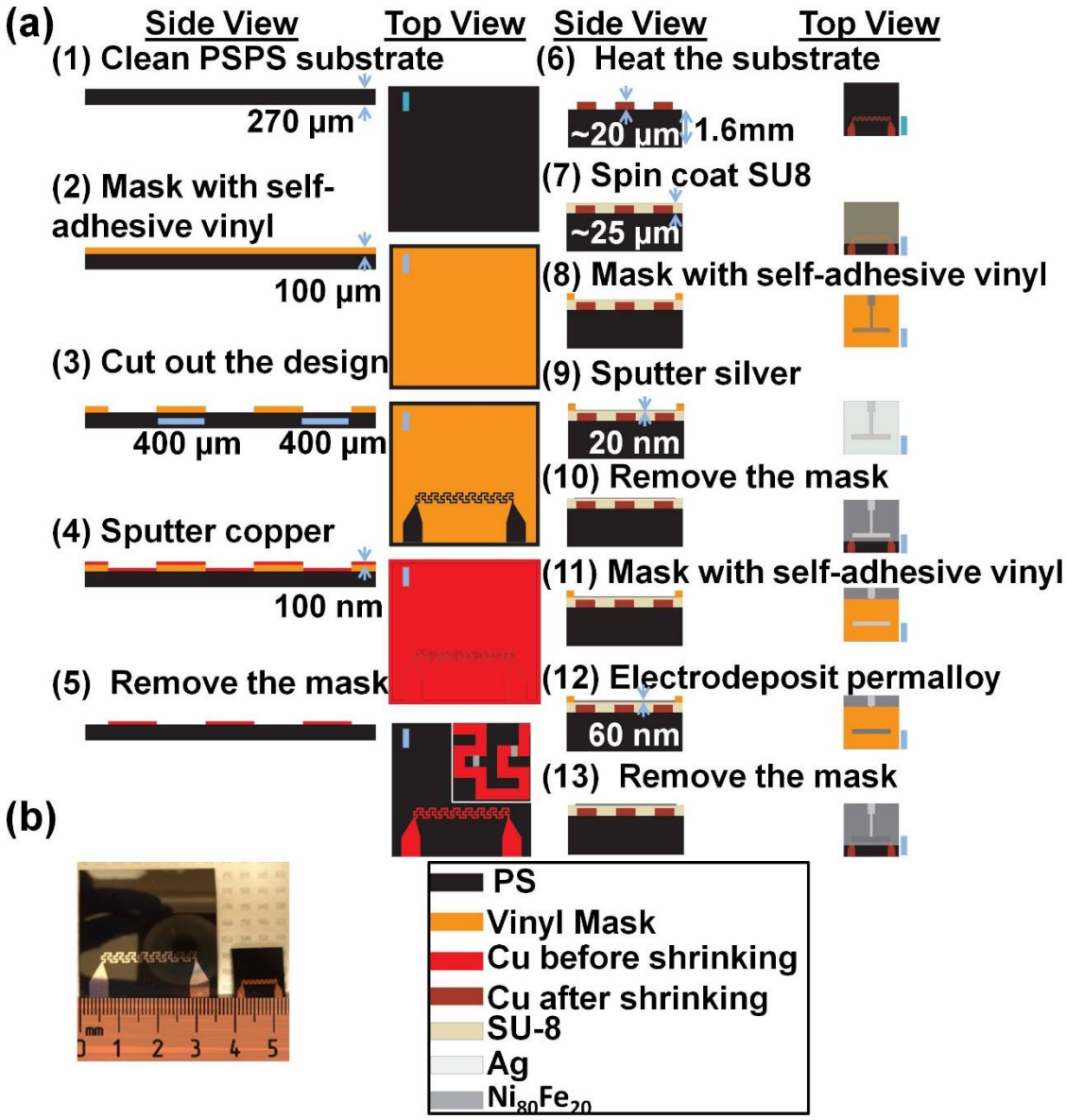

Figure 3.1 Fabrication of micro-electromagnets on polystyrene substrates (a) top- and side-view schematic of the fabrication process. All scale bars represent 5 mm, except the scale bar in the inset of step 5 (top-view) represents 400 µm. (b) Optical images of the pre-shrunk (left) and shrunk (right) PSPS devices. Reprinted from [97], with the permission of AIP Publishing, Copyright (**2014**).

3.3.3 COMSOL Simulations

To compare the magnetic field strength, gradient, and force generated by active and active-passive devices and to investigate the effect of wrinkled structures on the magnetic force, numerical simulation was performed using the finite element analysis software COMSOL Multiphysics (version 4.3b, COMSOL, Burlington, Massachusetts), purchased from Canadian Microelectronics Corporation (CMC).

3.3.4 SEM Characterization

SEM images of the wrinkle copper structures were obtained using a JEOL JSM-7000S Scanning Electron Microscope with an accelerating voltage of 3 kV for cross section images, and 10kV for top view images.

3.3.5 Permalloy Characterization

EDX was used to obtain the composition of the electrodeposited permalloy. TESCAN VEGA scanning electron microscope with backscatter electron detector and an accelerating voltage of 10 kV was employed to perform the EDX analysis. In addition, magnetic properties of the deposited permalloy were obtained using superconducting quantum interference device (SQUID) magnetometer (Quantum Design Inc, San Diego, California) with the range of magnetic field scanning of -8 to 8 kA/m.

3.3.6 Trapping of Magnetic Microparticles

The magnetic beads solution with concentration of 4×10^6 beads/ml was prepared from the stock solution of concentration of 2×10^9 beads/ml. A 5×5 mm^2 reservoir was patterned on 150 μm thick double-sided tape (3M Canada, London, Ontario) using a laser engraver (VLS3.50, Universal Laser Systems, Scottsdale, Arizona), and bonded to the

device surface. Next, a drop of the beads solution (10 µl) was added onto the surface of the device, within the reservoir, covered by a cover slip. After that a DC current of 30-50 mA was applied to the contact pads using a power source (Keithley Instruments, Cleveland, Ohio). The entire experiments were conducted under an optical microscope (Nikon, Mianto, Tokyo, Japan) equipped with a Retiga 2000R scientific camera (Q Imaging, Surrey, BC) to record and monitor the motion of the magnetic particles in real time. To reduce the effect of the joule heating, the devices were mounted on top of a thermoelectric cooler, which was attached on top of a heat sink (aluminium plate). Each experiment was run for 10 minutes.

3.4 Results and Discussion

Our vision was to create on-chip electromagnets with sub-millimeter dimensions and sub-micrometer surface texturing using benchtop, rapid, and dynamic fabrication methods. Figure 3.1 summarizes this fabrication process. Cleaned prestressed polystyrene (PSPS) sheets were masked with self-adhesive vinyl (Figure 3.1, steps 1 and 2). A mesh-shaped meandering design with the smallest feature size of 400 µm was cut into the vinyl using a robotic craft cutter (Figure 3.1, step 3). A 100 nm copper film was sputtered onto the patterned vinyl mask (Figure 3.1, step 4), and after removing the mask the mesh-shaped meandering design was obtained (Figure 3.1, step 5). Copper-coated PSPS devices were heated for 3 min at 150–160 °C (Figure 3.1, step 6) as heating PSPS above its glass transition temperature of 100 °C causes it to shrink to under 50% of its original size due to polymer chain relaxation.[160] Figure 3.1b shows the photograph of the active devices before (left) and after (right) shrinking. The mesh-shaped meandering design was chosen

for the copper wire as Ramadan *et al.* reported an enhancement in the generated magnetic force in this design compared to planar and rosette geometries.[110] The thermal shrinking process was used here to serve a dual purpose: to reduce the electrode width and inter-electrode spacing while increasing its height, and to introduce micro/nanotexturing to the electrode surfaces.[160] Previous reports have shown that reducing the conductor width and spacing increases the magnetic field gradient (in the direction perpendicular to the reduced side) and strength.[110] In addition, we have previously shown that the sheet resistance of metallic thin films (≤100 nm) decreases after the wrinkling process due to an increase in the effective height of the film. This effect would allow us to create wrinkled metal lines having a smaller resistance compared to non-wrinkled lines (with the same thickness as the wrinkled film before shrinking) of the same footprint.[160]

After fabricating the device active layer, we designed a process flow to integrate a magnetic material on the copper layer for enhancing the magnetic force at a given current. A thick layer of negative photoresist, SU-8 2007, was spun on the active device and baked at 95 °C for 15 min (Figure 3.1, step 7). SU-8 2007 was chosen as the insulating layer between the copper and the magnetic material (permalloy) due to its relatively low baking temperature and compatibility with the PSPS substrate.[159] The SU-8 thickness is important for maximizing the magnetic force while eliminating inter-metallic current leakage, and was optimized to be 25 µm. A second vinyl mask was used in combination with a lift-off process to create a silver seed layer (Figure 3.1 steps 8–10) for permalloy electrodeposition. Permalloy electrodeposition was done in a rectangular area (10 × 1.2 mm) defined by a third vinyl mask (Figure 3.1, steps 11–13) using chronopotentiometry

(current density = 5 mA/cm^2 for 44 s) in a three-electrode electrochemical cell. The electrodeposition bath (0.95M $NiSO_4.6H_2O$, 18mM $FeSO_4.7H_2O$, 0.4 M H_3BO_3, 4.87mM sodium saccharin, and 0.35mM sodium dodecyl sulfate) was optimized to obtain a uniform permalloy layer at a composition of Ni_{80}/Fe_{20}.[161]–[164] The thickness of the electrodeposited permalloy was estimated to be around 60 nm based on the total electronic charge transferred during electrodeposition.

The Scanning Electron Microscopy (SEM) images presented in Figure 3.2 show the copper strips in the mesh-shaped meandering design to be approximately 130–140 µm wide (Figure 3.2a) and >20 µm thick (Figure 3.2c). Furthermore, these images demonstrate the film to be composed of repeating hills and valleys with micrometer and sub-micrometer dimensions (Figure. 3.2a–c). This micro-structuring has been reported in the past as compressive stresses were exerted on metallic films causing them to buckle.[29], [160]

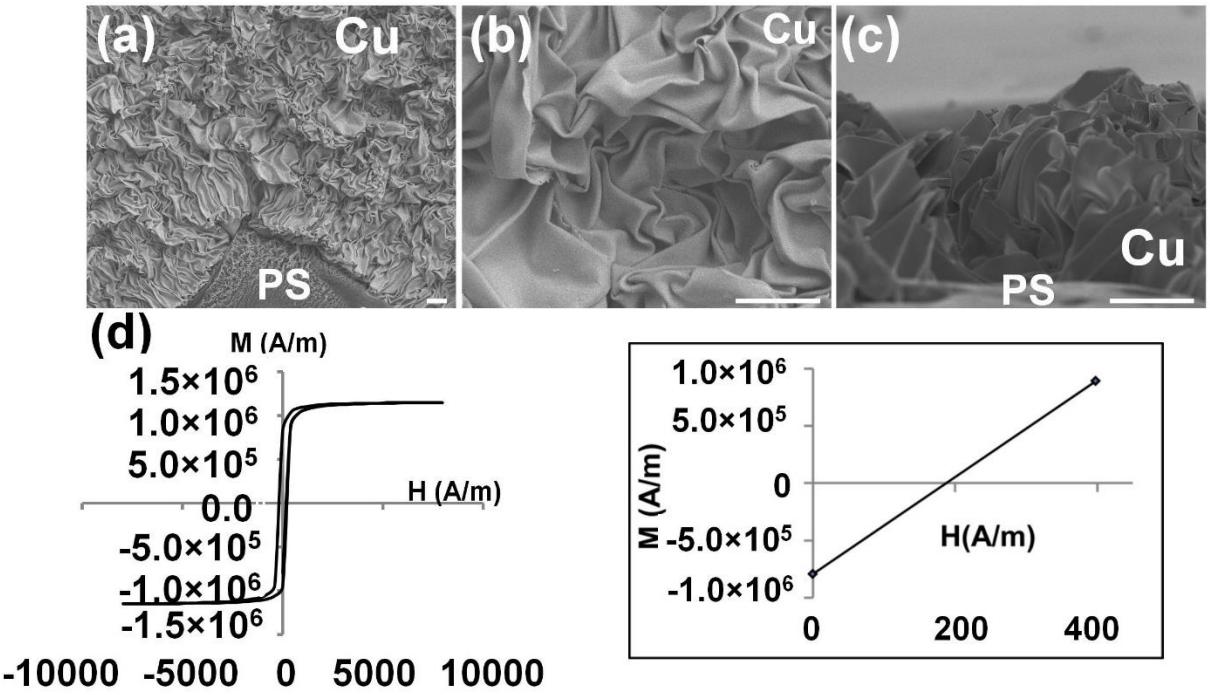

Figure 3.2 Micro-electromagnet materials characterization. (a) Low and (b) high magnification top view, and (c) high magnification side-view SEM images of the wrinkled copper structures. All scale bars represent 10 µm. (d) The M-H response of the electrodeposited permalloy obtained by SQUID. The inset shows the steepest part of the hysteresis curve. Reprinted from [97], with the permission of AIP Publishing, Copyright (**2014**).

To better understand the magnetic properties of the electrodeposited permalloy, energy-dispersive X-ray spectroscopy (EDX) was used to identify its composition. The permalloy composition was measured on three different samples and an average value of 85% Nickel and 15% iron (data not shown) was obtained, which is consistent with previous studies.[157], [161] In addition, superconducting quantum interference device (SQUID) magnetometer was used to obtain the magnetization versus magnetic field hysteresis plot (Figure 3.2d). The saturation magnetization (M_s) was estimated from this plot to be 1150 emu/cm^3, which is consistent with its tabled values for permalloy.[163] The relative

permeability (μ_r) was estimated from the linear portion of the M-H plot (Figure 3.2d inset) to be approximately 4000 using the following relationship:

$$\mu_r = \frac{M}{H} + 1 \quad (1)$$

Such high μ_r provides a magnetic flux linkage intensifying the generated magnetic flux density, which is desirable for trapping MPs.[165] The coercivity (H_c) of the electrodeposited permalloy, calculated from the M-H plot (Figure 3.2d), is 192 A/m. This relatively low coercivity is crucial for trapping and releasing MPs by modulating the current passing through the microcoil.[165]

In order to compare active and active-passive devices and to understand the effect of surface texturing on the magnitude, direction, and localization of magnetic force, a series of micro-electromagnetic devices were modeled and simulated using the finite element analysis method.

To study the effect of wrinkled copper structures on the magnetic force, the problem was simplified from 3D to 2D reducing the computational complexity in meshing and solving the problem.[165], [166] Through these simulations, we compare the flat versus crumpled copper structures in terms of magnetic field strength (|H|), gradient ($|\nabla\vec{B}|$), and force (F_y) exerted on 2.8 µm MPs (I = 35 mA). The magnetic force was numerically calculated using the following equation derived from the Maxwell tensor equation:[108], [110]

$$\overrightarrow{F_{mag}} = \frac{V\Delta\chi}{\mu_0}(\vec{B} \cdot \nabla)\vec{B} \quad (2)$$

where $\overrightarrow{F_{mag}}$ is the magnetic force exerted on each particle, V is the particle volume, and $\Delta\chi$ is the effective magnetic susceptibility of the particle relative to the surrounding medium. $\vec{B}$, $\nabla\vec{B}$, and μ_0 are the magnetic flux density, field gradient, and permeability of free space, respectively. To simplify the problem, we look at MP capture in the y-direction.

The schematic drawings of the flat (Figure 3.3a left) and wrinkled devices (Figure 3.3a right) are presented in Figure 3.3a. It should be noted that a conformal coverage of SU-8 over the wrinkled layer is assumed for the models generated (Figure 3.3a and b inset). |H|, $|\nabla\vec{B}|$, and F_y are plotted against distance in the X-coordinate and are shown in Figure 3.3b–d, respectively. Negative F_y indicates an attractive magnetic force towards the device surface. These simulation results indicate that the magnetic field strength (Figure 3.3), gradient (Figure 3.3c), and force (Figure 3.3b) are enhanced at the tips of the wrinkles. Although the magnetic field strength shows a slight increase at the tips of the wrinkles, the field gradient and the force are about 3 folds higher than the relatively uniform values seen on the flat structure (Figure 3.3b and c right). This local magnetic force enhancement is expected at the tips of the wrinkles due to the higher field gradient close to sharp and narrow regions.[29]

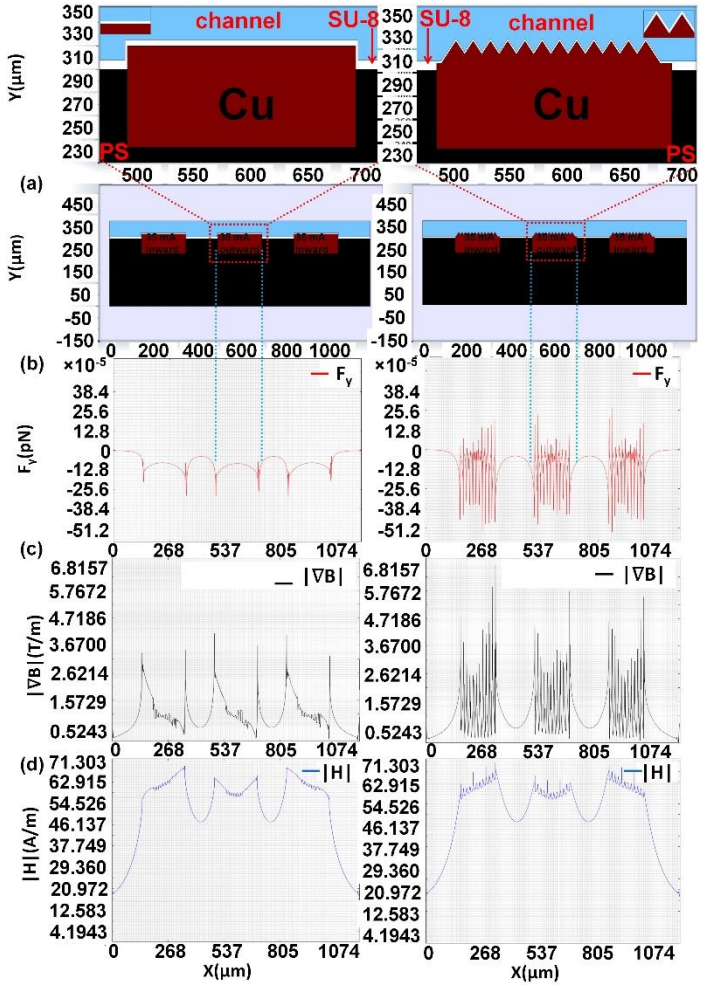

Figure 3.3 Comparing the magnetic field strength, gradient, and force of flat and wrinkled devices. (a) Schematic drawing showing the cross section often flat (left) and wrinkled (right) devices. The zoomed-in schematic is shown as an inset. 2D simulation of (b) F_y, (c) $|\nabla\vec{B}|$, and (d) |H| generated by a flat (left) and a wrinkled (right) device. (MPs diameter = 2.8 μm, χ = 0.17, and I = 35 mA). Reprinted from [97], with the permission of AIP Publishing, Copyright (**2014**).

To study the differences between active and active-passive devices in generating a magnetic force, we created a 3D model considering one period of the mesh-shaped meandering design. A single period was simulated to reduce the computational complexity (Figure 3.4). The spatial distributions of |H|, $|\nabla\vec{B}|$, and |F| were investigated on the surface of four different device architectures: (1) an active device with the copper meandering

design at the surface (Figure 3.4a); (2) an active device similar to (1) with an SU-8 coating (Figure 3.4b); (3) an active-passive device composed of device (2) topped with a rectangular permalloy layer (Figure 3.4c); and (4) an active-passive device similar to (3), except the permalloy is patterned to have a meandering design aligned with the underlying copper layer (Figure 3.4d).

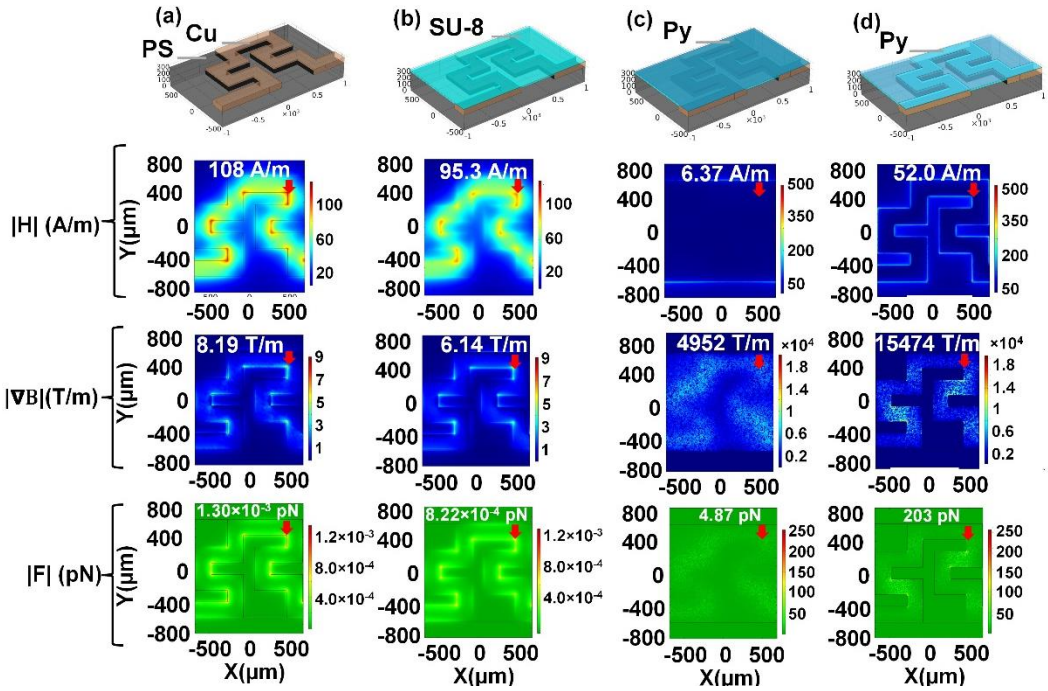

Figure 3.4 3D simulation of magnetic field strength, gradient, and force on the surface of (a) copper, (b) SU-8, permalloy (Py) patterned as a (c) rectangle, and (d) the meandering design on polystyrene (PS) substrates. (I = 35 mA, MP diameter = 2.8 μm, and MP χ= 0.17). First row from top for each sub-figure demonstrates the device schematics; second, third and fourth rows demonstrate |H|, $|\nabla\vec{B}|$, and |F| heat maps, respectively, with the color maps representing these variables. |H|, $|\nabla\vec{B}|$, and |F| for a particular point are shown using a red arrow. Reprinted from [97], with the permission of AIP Publishing, Copyright (**2014**).

It is evident from Figure 3.4a that higher magnetic field, gradient, and force are generated inside the U-shaped loop structure of the meandering design (the location is shown with an arrow on the figures). This is expected as the magnetic field components

add constructively in this region. By adding the SU-8 coating (Figure 3.4b), we see a slight decrease in the magnetic force. This is expected as the magnetic field deceases rapidly as we move away from the surface of the electromagnet. As the rectangular permalloy layer (Figure 3.4c) is added, the magnetic field decreases at the middle of the permalloy layer and increases at its edges compared to the active devices. This behavior is expected as the permalloy acts as a magnetic flux guide, drawing the field to its edges and creating a path for magnetic field lines. On the other hand, the magnetic field gradient increases after adding the permalloy to the active device due to its high relative permeability. As the permalloy layer is patterned in the meandering design, more magnetic flux guiding edges are present, serving as locations with enhanced magnetic fields. In addition, the magnetic field gradient and force are increased at these locations due to the presence of more sharp edges (Figure 3.4d).

The increased magnetic forces observed for active-passive devices are consistent with the previous study by Abidin *et al.*[165] Given the more than 40 times increase in the magnitude of the generated force using the meandering compared to the rectangular permalloy, we believe an optimal magnetic trapping device could be fabricated by adopting this design. However, using the presented fabrication technique, it is difficult to reproducibly create features smaller than 200 µm into the vinyl mask to match the dimensions of the underlying shrunk copper film. Furthermore, it is challenging to achieve inter-layer alignment with sufficient precision using this method. Consequently, we chose the device design presented in Figure 3.4c for our validation experiments. Based on the simulation results (Figure 3.4c), the magnetic flux density generated by this device at the

inner loop of the meandering design is about 40 mT (μ_r =4000). This is at least 4 times larger than the fields previously reported for microfabricated on-chip electromagnetic devices (operated at currents larger than 100 mA) used for trapping MPs of about the same size.[107], [108]

In order to study the effectiveness of our fabricated devices in capturing MPs, we designed an experiment to record particle movement in real-time using an optical microscope. The schematic drawing of the device used is displayed in Figure 3.5a. Aqueous solutions of MPs were placed on the device surface and monitored as a 35 mA current was applied (Figure 3.5b), while the device was continuously cooled with a compact (2×2 cm) thermoelectric cooler and a heat sink (aluminum plate). In addition, application of a DC of 35mA for 10 min (Figure 3.5c, Multimedia view) was compared to a case where no current was applied to the on-chip electromagnets (Figure 3.5d, Multimedia view). It is seen from Figure 3.5c and d, (Multimedia view) that MPs are driven towards the device from distances larger than 100 µm and are immobilized at the edge of the permalloy layer when the current was on (Figure 3.5c), while this behavior was absent when the current was off (Figure 3.5d). In the absence of any electrical current, particles experienced a slow zigzag motion towards the permalloy surface and occasionally got collected by the device if they were within 5 µm of the device edge (Figure 3.5d, Multimedia view). This is due to the stray fields present at the edges of the magnetic film, which is likely originated from the magnetic domain arrangement. In spite of this sluggish movement, very little localized trapping was observed in this case.

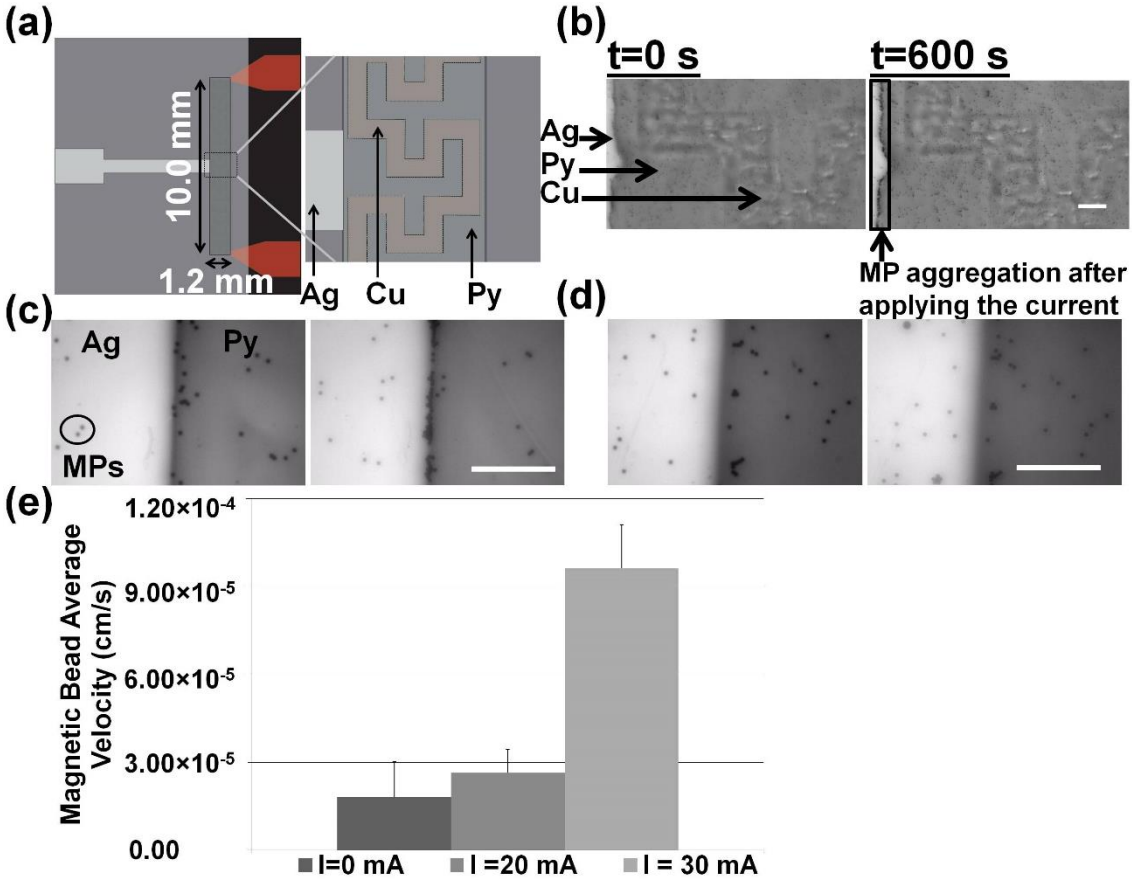

Figure 3.5 Experimental study of MP trapping using the fabricated microelectromagnet. (a) Top-view schematic of the device. The inset displays the zoomed-in device schematic. (b) Optical microscope images of the device before (left) and after (right) applying an electrical current (35 mA, 600 s). The Scale bar represents 100 µm. The zoomed-in optical microscopy images of the permalloy edge at t = 0 s (left) and t = 600 s (right) (c) under the influence of a 35mA and (d) no current. The scale bar represents 50 µm. (e) The mean average velocity of MPs (mean taken over 10 particles) suspended in water under different applied currents. The error bars represent standard deviation. (Multimedia view)[URL:*http://dx.doi.org/10.1063/*1.4893564.1][URL:*http://dx.doi.org/10.1063/1.4893564.2*] Reprinted from [97], with the permission of AIP Publishing, Copyright (**2014**).

To better understand the current dependence of the device and to estimate its minimum current requirement, we determined the average MP velocity under different current values. This was achieved by dividing the distance travelled by each MP by the time it took for it to travel the measured path. The mean average velocity of the particles

under the influence of a 35mA current was 2.8 E-4 cm/s, which was more than 13 times larger than the no current (1.8E-5 cm/s) scenario. This is expected, as the simulation results revealed that the current-carrying copper wire generates magnetic fields magnetizing the permalloy and attracting the MPs towards its edges. In addition, we determined the average particle velocity when the applied currents were 0, 20, and 30mA (Figure 3.5e). Through these experiments, we observed that statistically significant velocity increases (compared to I = 0) start to appear at currents between 20 and 30 mA, and we estimate the minimum DC requirement to be within this range.

Faster particle trapping was achieved at currents larger than 35 mA; however, this often led to device destruction. The required DC of 35 mA reported here is smaller by at least 3 folds compared to the previously reported devices for trapping MPs of about the same size.[106]–[108], [110], [167], [168] We suspect the presence of the permalloy[167] along with the micro/nanotexturing of the electrode surfaces developed here to be responsible for this reduced current requirement.

3.5 Conclusions

In summary, the PSPS-based micro-electromagnetic devices were fabricated using lithography-free benchtop techniques. These devices embedded active, current-carrying conductors, and passive ferromagnetic thin films separated by an insulating layer on a polymeric substrate. They combined a variety of multi-scale materials into a single microsystem and leveraged materials properties such as micro-/nano-wrinkling into increased magnetic flux density and reduced current requirement. The active-passive nature of the device allowed permalloy thin films to be magnetized by relatively low currents (35

mA) flowing through the microstructured wrinkled copper wires to collect 2.8 μm MPs suspended in an aqueous solution. These devices are ideal for addressing the rapid prototyping needs of industry and academic researchers as new device geometries can be made from design to fabrication in a matter of hours. One drawback of the devices presented here is their reliance on a separate thermoelectric cooler. We envision alleviating the issues related to excessive Joule heating by further lowering the minimum current requirement of the devices by using more optimal device designs such as those simulated in Figure 3.4d We will also investigate integrating micro-heat sinks[169] and micro-channel heat exchangers into the PSPS device using the previously described methods.[170]

3.6 Acknowledgements

The authors acknowledge funding support through NSERC Discovery Grant and Grand Challenges Canada, Rising Starts in Global Health programs. The electron microscopy research described in this paper was performed at the Canadian Centre for Electron Microscopy at McMaster University, which is supported by NSERC and other government agencies.

3.7 Supplementary Information

Authors: Amin Hosseini and Leyla Soleymani

Publication: Applied Physics Letters, 105, 7, 074102

Publication Date: August 2014

Supplementary Multimedia: http://dx.doi.org/10.1063/1.4893564.2

Chapter 4 Enrichment of Magnetic Particles using Temperature and Magnetic Field Gradients Induced by Benchtop Fabricated Micro-Electromagnets

Chapter Introduction (Objective B):

One of the challenges involved with using micro-electromagnet in magnetic separation is that at relatively low currents, the generated magnetic field is weak and thus the induced magnetic force attenuates rapidly moving away from the device surface; the magnetic forces decay up to 1% of their maxima (at the edge of the device) at the distance of ~ 1 μm from the force maxima. This behaviour did not show the same trend as predicted using theoretical calculations when we captured MPs using the prototyped devices in Chapter 3; MPs were attracted towards the magnetic traps from tens to hundreds of microns away from the edge of the permalloy. This chapter focuses on understanding the physics behind the device operation resulting in the enhanced device performance. Through numerical modeling, we study the combined effects of thermal gradients and magnetic field gradients on the movement of MPs that are further away from the device surface. To verify the simulation results, we designed multiple experiments to measure the terminal velocities of magnetic and non-magnetic beads at different distances from the magnetic hot spots. The overall results demonstrate that the enhanced fluid movement caused by the generated thermal gradient is the dominant force behind transporting the MPs from tens to hundreds of microns away from the edges of on-chip magnetic devices, while the magnetic force dominates at the vicinity ($\leq$ 1 μm) of the micro-electromagnet. This study provides the rationale behind designing a thermo-magnetic system, which applies temperature gradients

to drive MPs towards the magnetic traps and captures them using the generated magnetic force.

Authors: Amin Hosseini, David N. Philpott and Leyla Soleymani

Publication: Lab on a Chip, 17, 23, 4097–4104

Publication Date: October 2017

4.1 Abstract

The active transport of analytes inside biosensing systems is important for reducing the response time and enhancing the limit-of-detection of these systems. Due to the ease of functionalization with biorecognition agents and manipulation with magnetic fields, magnetic particles are widely used for active and directed transport of biological analytes. On-chip active electromagnets are ideally suited for manipulating magnetic particles in an automated and miniaturized fashion inside biosensing systems. Unfortunately, the magnetic force exerted by these devices decays rapidly as we move away from the device edges and increasing the generated force to the levels necessary for particle manipulation requires a parallel increase in the applied current and the resultant Joule heating. In this paper, we designed a study to understand the combined role of thermal and magnetic forces on the movement of magnetic particles in order to extend the interaction distance of on-chip magnetic devices beyond the device edges. For this purpose, we used a rapid prototyping method to create an active/passive on-chip electromagnet with a micro/nano-structured active layer and a patterned ferromagnetic passive layer. We demonstrated that

the measured terminal velocities of particles positioned near the electromagnet edge (~5.5 μm) closely reflect the values obtained by multi-physics modelling. Interestingly, we observed a two orders of magnitude deviation between the experimental and modelling results for the terminal velocities of particles far from the electromagnet edge (~55.5 μm). Heat modelling of the system using experimentally-measured thermal gradients indicates that this discrepancy is related to the enhanced fluid movement caused by thermal forces. This study enables the rational design of thermo-magnetic systems for thermally driving and magnetically capturing particles that are positioned at distances tens to hundreds of microns away from the edges of on-chip magnetic devices.

4.2 Introduction

Biosensors that combine high sensitivity and specificity with rapid sample-to-result time, low cost operation, portability and ease-of-use are central to the development of point-of-care diagnostics and continuous health monitoring platforms. Miniaturization is an ongoing trend in biosensor development since it enables multiple sensing and sample preparation components to be integrated into a single platform.[12] In addition, miniaturization into the nanoscale has been used to enhance the signal transduction efficiency of various classes of biosensors.[31] In spite of these advantages, the mass transport of target analytes from the solution to the sensor surface significantly limits the response time and limit-of-detection of nanoscale biosensors.[172] In order to overcome this limitation, several methods have been developed to decrease the long (hours to days)[37] mass transport times associated with the diffusion of target analytes to the surface of nanoscale biosensors. Particularly, force field based strategies such as

electrophoresis,[173] dielectrophoresis,[174], [175] thermal focusing,[44], [176] and magnetic separation/enrichment[94], [131] have been widely used for active and targeted delivery of analytes to the sensor surface. Among these, magnetic separation is ideally-suited for transporting a wide range of target analytes; because, it does not rely on the inherent properties of the analyte such as electrostatic charge or dielectric constant. In this technique, magnetic force is used to actively transport cells or biomolecules that are conjugated with magnetic particles (MPs), and deliver them into pre-defined locations.[110], [116], [136], [151]–[156]

On-chip magnetic separation is generally performed using passive and/or active devices.[96] Passive devices use micro-/nano-scale ferromagnetic structures that induce localized magnetic field gradients when magnetized by an external magnetic field,[29], [98], [99] while active devices use current-carrying electromagnets that generate localized magnetic fields and gradients to trap or redirect MPs.[43], [100], [101], [157] Although passive devices are relatively facile to fabricate and operate, they rely on external magnets, and it is difficult to program their operation (for example the capture and release of MPs) using a handheld electrical test and measurement instrument for use in fully-integrated biosensors. A wide range of active devices have been developed using photolithographic[106], [113], [114] and rapid prototyping[97] methods, which use planar magnetic coils to generate a magnetic field. Furthermore, active/passive devices use a combination of planar magnetic coils and ferromagnetic materials separated by an insulating layer[97], [102], [103] to enhance the magnetic field gradients for attracting and capturing microscale or nanoscale MPs. The major difficulty in employing active on-chip

magnetic separation in biosensing is twofold. On one hand, the magnetic force decays rapidly (the magnetic force exerted on a MP is directly proportional to the product of the magnetic flux density and field gradient[177]) as we move away from the transducer surface into the sample solution and it becomes necessary to increase the applied current to generate the force needed for transporting and capturing MPs from the solution. On the other hand, the increased applied current results in Joule heating, which could produce complexity in the device operation and performance.

In this study, our goal was to overcome the above-mentioned difficulties in active on-chip magnetic separation by understanding the effect of Joule heating on the fluidic flow, and to use this to create a bi-modal thermo-magnetic separation device. Our vision was to use modest thermal gradients to drive the MPs to locations where the magnetic force is strong enough, at a moderately low current (<50 mA), to magnetically capture the particles. Temperature gradients have been previously used as a strategy for actively delivering analytes and particles to sensing sites through natural advection and thermophoresis.[44], [45], [47], [48] Towards this goal, we performed a comprehensive numerical and experimental study to simulate and measure the terminal velocities of magnetic and non-magnetic particles at different locations on an active magnetic chip. These results, along with local temperature measurements and thermal gradient modelling inside the sample solution provide significant insight on the mechanisms of transport in active magnetic devices. It is concluded that the heat driven-flow caused by temperature gradients and natural convection effectively transport MPs inside the solution to locations where the magnetic forces are strong enough for magnetic capture. This makes the bi-modal

transport and capture strategy, a practical method for extending the interaction distance of active on-chip magnetic devices and enhancing the mass transport of analytes in biosensing systems. It should be noted that while Joule heating is typically detrimental to the integrity of the device and the quality of biological samples, in this particular case, it can be leveraged to enhance the device performance in a positive way. The operation of the thermo-magnetic device developed here is based on modest temperature increases (∼6 °C) at an applied current of 30 mA, which results in a maximum sample temperature of ∼25°C. Since this temperature is lower than the melting temperature of the large majority of biomolecules (nucleic acids and proteins) used in bioassays or the lysing temperature of cells, we believe the developed thermomagnetic route to be a vital strategy for use in systems that contain biological analytes.

4.3 Experimental

4.3.1 Device fabrication

Polystyrene devices. Figure 4.1(a) shows the side and top view of the bench-top fabrication process. All devices were fabricated on pre-strained polystyrene (PSPS) (55 × 55 mm^2) substrates (Graphix Shrink Film, Graphix, Maple Heights, OH, USA). PSPS substrates were cleaned under orbital agitation for 10 min in isopropanol and Milli-Q grade deionised (DI) water and were dried using a stream of air. Self-adhesive vinyl (FDC 4304 Easy Removable sign vinyl, BDF Graphics, Toronto, ON, Canada) was used as the masking material during the fabrication process. Self-adhesive vinyl sheets were laid on the cleaned PSPS using a hand roller. The mesh-shaped meandering[110] design was created using Adobe Illustrator software and patterned into the self-adhesive vinyl using the Robo Pro

CE5000-40-CRP cutter (Graphtec America Inc., Irvine, CA, USA) equipped with a 0.9 mm standard vinyl cutting blade (CB09UA), with force, quality and speed set at 10, 1, and 1 respectively. The patterned meandering shapes were peeled off from the PSPS substrate using tweezers. Next, 100 nm of copper was sputtered from a 99.999% purity copper target (Kurt J. Lesker Company, Concord, ON, Canada) using a Torr Compact Research Coater CRC-600 manual planar magnetron DC sputtering system (Torr International Inc. New Windsor, NY, USA) onto the masked PSPS substrates. The argon plasma was generated by a DC current of 60 A, which leads to a copper deposition rate of 0.4 Å/s monitored by the quartz crystal sensor. After sputtering, the vinyl masks were lifted manually using tweezers. Patterned copper-coated PSPS substrates were placed on an aluminium block, heat treated and shrunk at 160 °C in an oven (BINDER, GENEQ Inc., Tuttlingen, Germany) for 3 minutes. After shrinking, the devices contact pads were masked with a regular tape and the surface of the devices was rinsed with ethanol and DI water, dried with a stream of air, and placed on a hotplate at 60 °C for 30 minutes. After cooling down the devices at room temperature for a few minutes, they were placed inside a spin coater (Laurell Technologies, North Wales, PA, USA). Next, the surface of the devices was covered with the negative photoresist SU-8 2007 (MicroChem, Newton, MA, USA) using a syringe and waited for 20 seconds to let the SU-8 disperse over the device surface. The spin coater was operated at 1000 rpm for 30 seconds. After the first round of spin coating, the devices were soft baked at 95 °C for 3 minutes and cooled down to room temperature. This baking procedure was repeated for another 20 minutes. After cooling down the device to room temperature, the first layer of SU-8 was fully cured. Next, the spinner setting was changed to 2500 rpm,

and the entire spin coating and baking procedure was repeated. The final thickness of the cured SU-8 was verified to be ~ 25 µm using alpha step height measurement. After curing the SU-8, the tapes covering the contact pad were carefully removed using tweezers. A rectangular shaped design (2.28 ×18.16 mm^2) was patterned on the self-adhesive vinyl using Adobe Illustrator and the craft cutter, peeled off using tweezers, and aligned carefully on the shrunk polystyrene (PS) device. Next, 20 nm of gold thin film was deposited on the devices using the DC sputtering system with a DC current of 50 A, and a deposition rate of 0.90 Å/s. The gold acts as a conductive seed layer for the permalloy electrodeposition. After removing the vinyl, the devices were masked again with the self-adhesive vinyl with four rectangular openings (0.80 × 0.37 mm^2 in size, and 0.26 mm in spacing). The permalloy electroplating was performed using a CHI 660D electrochemical workstation (CH Instrument, Austin, TX, USA) and a standard three-electrode set-up. The electrochemical system consisted of an Ag/AgCl reference electrode, a platinum mesh counter electrode, and the PS device as the working electrode. The permalloy electrodeposition bath solution contained 0.95 M Nickel (II) sulfate hexahydrate, 18 mM Iron (II) sulfate heptahydrate, 0.4 M boric acid, 4.87 mM sodium saccharin, and 0.35 mM sodium dodecyl sulfate (Sigma-Aldrich, St. Louis, MO, USA). The permalloy plating was performed at room temperature using chronopotentiometry with a current density of 5 mA/cm^2 for a duration of 470 s. Following the deposition, the vinyl masks were removed, and the devices were rinsed with DI water and dried with a stream of air.

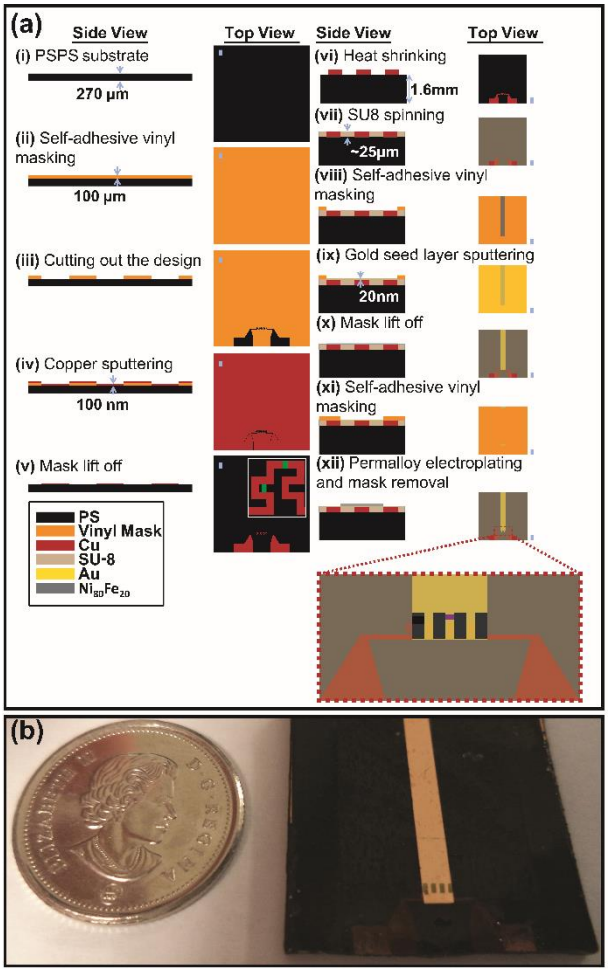

Figure 4.1 (a) Top-and side-view schematic of the fabrication process. All scale bars represent 5 mm, except the scale bars in the insets which represent 200 µm (green-step v), 370 µm (black-step xii), and 260 µm (purple-step xii). (b) Photograph of the benchtop-fabricated device

Silicon devices. The same mesh-shaped meandering design discussed above was fabricated on <100> silicon wafers (University Wafer, South Boston, MA, USA) using standard photolithography and lift-off techniques.

4.3.2 Numerical simulations

The 3D models of the magnetic forces generated by the device, and the coupled thermal-fluidic simulation within the reservoir were performed using COMSOL Multiphysics (version 4.3b) software.

4.3.3 Testing the devices with magnetic and polystyrene particles

An image of the bench-top microfabricated electromagnetic device is displayed in Figure 4.1(b). A 5×5 mm^2 reservoir was patterned on 150 µm thick double-sided tape (3M Canada, London, ON, Canada) using a laser engraver (VLS3.50, Universal Laser Systems, Scottsdale, AZ, USA), and bonded to the device surface. After adding the solution to the reservoir, it was enclosed by a hydrophobic coverslip (Trevigen Inc., Gaithersburg, MD, USA). The reservoir was designed in such a way that it contained both the meandering-shaped copper micro-coil and the permalloy layer. An aqueous solution of MPs with concentration of 4×10^6 /ml was prepared from a stock solution of 2.8 µm carboxylic acid coated Dynabeads M-270 (Invitrogen, Carlsbad, CA, USA) with concentration of 2×10^9 /ml. TWEEN 20 (1%) (BioShop, Burlington, ON, Canada) was added to the solution as a surfactant to minimize the non-specific adsorption effects. For each experiment, a 20 µl drop of the MP solution was deposited into the reservoir and covered by the coverslip, and a DC current of 30 mA was applied to the contact pads using a power supply (Keithley Instruments, Cleveland, OH, USA). The entire experiment was conducted under an optical microscope (Nikon, Mianto, Tokyo, Japan) equipped with a Retiga 2000R scientific camera (Q Imaging, Surrey, BC, Canada) in order to

record and monitor the motion of the MPs in real time. Each experiment was performed for 20 minutes. An identical experimental setup was used to test the devices with the 2.6 µm non-ionic PS beads (Molecular Probes Inc., Eugene, OR, USA). In order to control the generated heat, the device was mounted on an aluminium plate (a heat sink) which was submerged into an ice bath. For better heat conduction between the device and the heat sink, a high-density polysynthetic silver thermal paste (Arctic Silver Inc., Visalia, CA, USA) was applied to the bottom of the device, contacting the heat sink. An infrared camera, FLIR ONE (FLIR Systems Inc., Wilsonville, OR, USA) was used to monitor the temperature of the reservoir throughout the experiments.

4.4 Results & discussions

4.4.1 Device architecture

In order to better understand the transport mechanisms of MPs inside on-chip magnetic separation devices, we fabricated an active/passive device where the magnetic force generated and controlled in the active layer was enhanced by a passive ferromagnetic layer.[159], [165], [178]these chips were fabricated using a rapid prototyping method previously shown to result in localized magnetic force hot spots due to the presence of micro/nanostructures in the current-controlled active layer.[97] the active portion of the device was composed of a copper layer having a meandering design**,** which was separated from a ferromagnetic permalloy layer by an electrical insulator.

The active portion of the device was fabricated as follows (detailed description in the experimental section): the shrinkable substrates (PSPS) were masked with self-adhesive vinyl (Figure 4.1(a), i-ii), the meandering design with minimum feature size of 200 µm was

cut into the vinyl film (Figure 4.1(a), iii), a copper layer was sputtered onto the masked substrate and the vinyl mask was removed to obtain the meandering design (Figure 4.1(a), iv-v), and finally the copper-coated substrates were heated (Figure 4.1(a), vi). Heating the PSPS above its glass transition temperature (100 ºC) causes it to laterally shrink to 40% of its original size, and the resultant stress causes the sputtered copper film to wrinkle while maintaining its meandering pattern.[97], [160]In this study, we exploited the thermal shrinking process to miniaturize the device foot print (width and inter-electrode spacing)[97], [110] and introduce micro/nanoscale wrinkles in the micro-coil surfaces, enhancing the generated magnetic force due to existence of higher magnetic field gradients close to the sharp and narrow regions of the wrinkles.[29], [97]

Following the fabrication of the active portion of the device, a photoresist layer was deposited (Figure 4.1(a), *vii*) to electrically isolate the active and passive layers and the active layer and the sample solution. Following this step, the passive layer was fabricated as follows: a second patterned vinyl mask was placed on the insulator layer and was used to define the area for depositing a seed layer (Figure 4.1(a), *viii*), a seed layer was used for defining a conductive base for electrodepositing the ferromagnetic layer (Figure 4.1(a), *ix-x*). A third vinyl mask was placed on the substrate to create a template for permalloy electrodeposition (Figure 4.1(a), *xi*), and finally a permalloy layer was electrodeposited (Figure 4.1(a), *xii*).[97], [161], [162], [164] The permalloy composition was investigated using energy-dispersive X-ray spectroscopy. The electrodeposited permalloy was composed of 85% nickel and 15% iron, which is in line with previous studies.[157], [161]

The saturation magnetization, relative permeability, and coercivity of the electroplated permalloy were measured previously using superconductive quantum interference device (SQUID) magnetometer to be 1150 emu/cm^3, 4000, and 192 A/m respectively.[97] The edges of the patterned permalloy layer was designed to be aligned to the inner sides of the semi-loops in the copper meandering layer in order to create higher magnetic field gradients and stronger magnetic forces.[97] A photograph of the fabricated active/passive device used in this work is presented in Figure 4.1(b).

4.4.2 Simulation of the magnetic force and comparison with the experimental data

To investigate the effect of the magnetic force exerted on a single 2.8 µm MP at different distances from the permalloy edge, a 3D model was created in COMSOL Multiphysics considering one period of the meandering design (Figure 4.2(a)). One period of the micro-coil was simulated in order to reduce the computational time and complexity. A top view of the simulated device is displayed in Figure 4.2(a) with the inset showing the MPs positioned at 5.5 µm (*near*) and 55.5 µm (*far*) away from the edge of permalloy. This simulation enabled us to compute the magnetic force and the resultant terminal velocity exerted on the MPs suspended in a static solution at an applied current of 30 mA. Equation (1), derived from Maxwell tensor equation, was employed to numerically calculate the magnetic force:[43], [97], [108], [110]

$$\boldsymbol{F_m} = \frac{V\Delta\chi}{\mu_0}(\boldsymbol{B}\cdot\boldsymbol{\nabla})\boldsymbol{B} \quad (1)$$

where $\boldsymbol{F_m}$ is the magnetic force experienced by each MP, and V, $\Delta\chi$, μ_0, $\boldsymbol{B}$ and $\boldsymbol{\nabla B}$ are the MP volume, relative magnetic susceptibility, permeability of free space, magnetic flux density, and field gradient respectively.

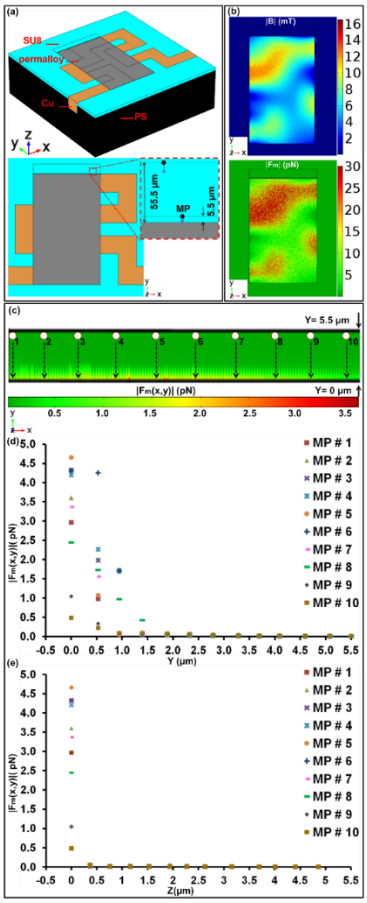

Figure 4.2 3D simulation of magnetic flux density ($|\boldsymbol{B}|$) and magnetic force ($|\boldsymbol{F_m}|$) with the application of a 30-mA current. (a) 3D (top) and top view (bottom) schematic of the device with the inset showing the MPs placed 5.5 and 55.5 µm away from the permalloy edge. (b) Heat maps demonstrating the spatial distribution of $|\boldsymbol{B}|$(top) and $|\boldsymbol{F_m}|$(bottom) at the surface of the permalloy layer. (c) 2D plot of the spatial distribution of magnetic force exerted on magnetic particles positioned on the SU8 layer. The white circles represent the MPs and their numbers represent the ones in the scattered 1D graphs. (d) 1D graph of the magnetic force ($|\boldsymbol{F_{m\_xy}}|$) applied to the 10 MPs depicted in Fig. 2(c) (MP #1–10) are placed at the SU8 surface as they move along the Y-axis towards permalloy. (e) 1D graph of the magnetic force ($|\boldsymbol{F_{m\_xy}}|$) exerted on the 10 MPs of Fig. 2(c) positioned at the permalloy edge (y = 0) at different heights. Z = 0 represents the case where the MPs are placed on the SU8 layer with their centers 1.4 µm above the SU8 surface.

The spatial distribution of magnetic flux density and its effect on the generated magnetic force were investigated at the device surface (Figure 4.2(b)). It is evident from Figure 4.2(b) and eqn (1) that $\boldsymbol{F_m}$ is directly proportional to $\boldsymbol{B}$. In addition, both $\boldsymbol{B}$ and $\boldsymbol{F_m}$ decay rapidly as we move away from the permalloy edge. In order to demonstrate this point more clearly, we investigated the spatial distribution of the magnetic force in the XY plane ($|\boldsymbol{F_{m\_xy}}|$) at different heights (Figure 4.2(c)–(e)). Fig. 4.2(d) demonstrates the magnetic force exerted on 10 MPs located on the SU8 layer at different positions on the X-axis, as they move along Y-axis towards the permalloy edge. Figure 4.2(e) demonstrates the magnetic force ($|\boldsymbol{F_{m\_xy}}|$) applied to 10 MPs located at the edge of the permalloy (y = 0) at different positions on the X-axis at different heights. It is evident that a higher magnetic force is generated closer to the edge of the permalloy, which decays rapidly as we move away from the edge in the Y or Z direction. It should be noted that the magnitude of the magnetic force exerted on the MPs positioned at different X positions were different. For example, at the edge of the permalloy (y = 0, z = 0), MP #5 experience a magnetic force of ∼4.7 pN while MP #10 experiences a magnetic force of ∼0.5 pN. This behaviour is due to the non-homogeneity of magnetic flux density and field gradients along the permalloy layer in the X-direction.

Our goal was to use the simulation results discussed above to calculate the terminal velocity of the MPs inside a static solution. At equilibrium, the forces that are acting on a single MP suspended in a static solution in the XY plane are $\boldsymbol{F_{m\_xy}}$ and the viscous drag

force ($\boldsymbol{F_{d\_xy}}$) opposing the magnetic force. For a spherical particle, the viscous drag force is given by Equation (2):[43], [144]

$$\boldsymbol{F_{d\_xy}} = 6\pi\eta r\,(\boldsymbol{u_{xy}} - \boldsymbol{v_{xy}})\,f_d \tag{2}$$

where η, r, $\boldsymbol{u_{xy}}$, $\boldsymbol{v_{xy}}$, and f_d are the medium viscosity, particle radius, fluid velocity, particle velocity, and drag coefficient respectively.[145] Applying Newton's second law, the particle terminal velocity in the XY plane is calculated using Equation (3):[144]

$$\boldsymbol{v_{xy}} = \frac{\boldsymbol{F_{m\_xy}}}{6\pi\eta r f_d} + \boldsymbol{u_{xy}} \tag{3}$$

Applying equation (3) and assuming the solution is stationary ($\boldsymbol{u_{xy}} = 0$), the mean average terminal velocities of the near and far particles were calculated to be 5.4 ± 3.0 μm/s and 0.0010 ± 0.0003 μm/s respectively.

In order to understand the mechanism of transport of near and far MPs, and to determine whether other forces beyond magnetic and drag forces play a significant role in particle transport, we designed an experiment to monitor the movement of MPs in real-time. An aqueous solution of MPs was placed inside a covered reservoir bonded to the device, and a 30 mA DC current was applied to the electromagnet for 20 minutes. It was observed that MPs were attracted from distances larger than 100 μm and captured at the edge of the permalloy structures after applying the current (see the Supplementary Multimedia files). Figure 4.3(a) displays the position of MPs at time zero (before turning the current ON) and 20 minutes after the current was applied. The MPs were immobilized on the permalloy edge due to high field gradients in these regions[97]. The experimental terminal velocities of MPs were calculated by dividing the distance and duration of their travel. As shown in Figure 4.3(b), the mean average velocity ($\boldsymbol{v_{xy}}$) of the near particles was

4.0 ± 2.0 (µm/s), which is in the same order of the magnitude as the simulation results (5.4 ± 3.0 µm/s). More interestingly, the far MPs were driven toward the electromagnet with the mean average terminal velocity of 0.26 ± 0.06 (µm/s), which is two orders of magnitude larger than the simulation results (0.0010 ± 0.0003). These results demonstrate that the magnetic force dominates the attraction of the near MPs, while additional forces are considerable in driving the far MPs.

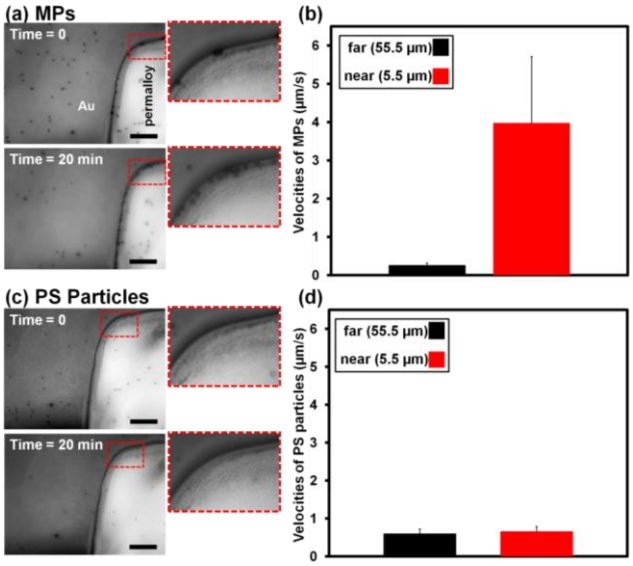

Figure 4.3 Experimental study of the motion of MPs and PS particles in the reservoir featuring the micro-electromagnet. (a) and (c) Display the optical microscopy images of the device before and after applying a DC current of 30 mA for 20 min for MPs and PS particles respectively. The scale bar represents 50 µm. The insets display the edge of permalloy before and after applying the current. The MPs were trapped on the edge of the permalloy while PS beads were not captured. (b) and (d) Show the mean average terminal velocities of MPs and PS particles respectively. The error bars represent standard deviation.

In order to understand the underlying reason for the deviation between the simulation and experimental results obtained for the terminal velocity of the far MPs, we designed an experiment where MPs were replaced with uncharged non-magnetic PS particles with an average diameter of 2.6 µm. Through these experiments, it was

observed that, similar to the MPs, the PS particles were initially stationary and began moving toward the electromagnet after applying the electrical current (see the Supplementary Multimedia files). However, there was one major difference between the interactions of these two types of particles with the electromagnet: unlike the MPs, the PS particles did not get immobilized at the edge of permalloy layer (Figure 4.3(c)). In addition, the mean average terminal velocity of PS particles was similar for near (0.66 ± 0.13 μm/s) and far (0.60 ± 0.12 μm/s) particles (Figure 4.3(d)), indicating that unlike MPs, PS particles did not experience larger forces as they became closer to the permalloy edge. The movement of PS particles under an applied current indicates that other forces are playing a significant role in moving the particles in the designed system. As a control experiment, the movement of MPs and PS particles were monitored when no current was applied (see the supplementary multimedia files). With the current off, the particles demonstrated a non-directional zig-zag motion, which indicates that the transport and/or capture of the particles are indeed current-controlled.

Heat driven fluidic flow[44], [179] and electrophoretic particle movement[173] have both been exploited in microfluidic systems for generating flow and manipulating particles. Since the PS particles are not designed to have a functional layer with a surface charge, and their movement direction does not change by varying the direction of the current (data not shown), we expect the influence of electrostatic forces to be negligible in particle manipulation. However, the generation of fluid movement as a result of the Joule

heating induced in this system is a plausible hypothesis, which we will further investigate with the aid of modelling and experimental studies.

4.4.3 Investigation of heat-driven fluidic flow

We hypothesized that the natural advection caused by Joule heating could be responsible for the transport of far MPs and PS particles.[45] In order to investigate this, a 3D multi-physics model was created to simulate the fluid flow caused by convective heat transfer in the fluid. The model involved two physics interfaces: the laminar flow for single-phase fluid flow and the heat transfer in fluids. The pressure (p) and velocity fields ($\boldsymbol{u}$) were solved using Navier–Stokes equations, while the temperature (T) was computed through the heat equation. The equations were coupled in both directions:

$$\begin{cases} \rho \frac{\partial \boldsymbol{u}}{\partial t} + \rho(\boldsymbol{u} \cdot \nabla)\boldsymbol{u} = -\nabla p + \eta \nabla^2 \boldsymbol{u} + \boldsymbol{F_b} \\ \nabla \cdot \boldsymbol{u} = 0 \end{cases} \quad (4)$$

where ρ is the fluid density and $\boldsymbol{F_b}$ is the buoyancy force. Since the model was solved in the steady state, the first term of the eqn (4) ($\partial \boldsymbol{u}/\partial t$) is set to zero. The buoyancy force ($\boldsymbol{F_b}$), responsible for lifting the fluid, was calculated as:

$$\boldsymbol{F_b} = g\rho\alpha\,(T - T_{in}) \quad (5)$$

where g and α are the gravitational acceleration and coefficient of thermal expansion (1.8×10^{-4} K^{-1} for water),[180] respectively. T_{in} is the steady state temperature of the portion of the fluid 1 mm away from the edge of the permalloy, which was experimentally measured using an infrared camera to be 18.5± 3.0 °C. The heat equation, accounting for convective heat transfer in the fluid, was utilized to calculate the temperature throughout the fluid (T):

$$\rho C_p \frac{\partial T}{\partial t} + \nabla \cdot (-k\nabla T + \rho C_p T\boldsymbol{u}) = Q \quad (6)$$

where C_p and k are the heat capacity at constant pressure and thermal conductivity of the fluid respectively, and Q represents the heat flux. Two boundary conditions, T_{in} = 18.5 ± 3.0 °C and T_{heat} = 24.8 ± 1.0 °C, were assigned as the fluid temperature 1 mm away from the permalloy edge and at the permalloy edge respectively. These values were recorded experimentally using an infrared camera. We assumed the temperature did not change with time, setting the first term ($\partial T/\partial t$) to zero. To explain the heat transfer through the PS substrate, we used a variant of the heat equation that describes the in-plane heat flux in the layer:

$$-\boldsymbol{n} \cdot (-k\nabla T) = d_s Q_s - \nabla \cdot (-d_s k_s \nabla T) \quad (7)$$

where d_s is the substrate thickness, Q_s (W/m^3) represents the internal heat source within the substrate, and k_s is the PS thermal conductivity at constant pressure (0.033 W/mK).

The result of the coupled thermal-fluidic model is shown in Figure 4.4. Due to symmetry, only a portion of the reservoir fluid, containing one half of a single (out of four) permalloy structure up to 1 mm away from the edge of the permalloy, was simulated to reduce the computational time and complexity. Figure 4.4 demonstrates a temperature difference of ~6.3 °C between the colder (1 mm from the permalloy edge) and warmer (at the permalloy edge) areas in steady state. In order to stay in equilibrium, the colder fluid needs to replace the warmer fluid continuously within the reservoir. The direction of the fluid velocity fields is shown using arrows in Figure 4.4, with the size of the arrows proportional to their magnitudes. Figure 4.4(a) demonstrates a 3D view of the fluid being forced to move from colder to warmer areas, generating a laminar flow. Figure 4.4(b) shows

the top view of the device surface and the motion of the fluid toward the electromagnet, which is in agreement with our experimental results. This can be justified by the temperature differences generated within the fluid as a result of current-induced Joule heating and poor thermal conductivity of the substrate (polystyrene), providing an explanation of the underlying mechanism behind the attraction of far MPs and PS particles towards the micro-electromagnet. It should be noted that the capture of MPs at the permalloy edge requires the cooperation of thermal and magnetic forces to drive and capture the MPs respectively.

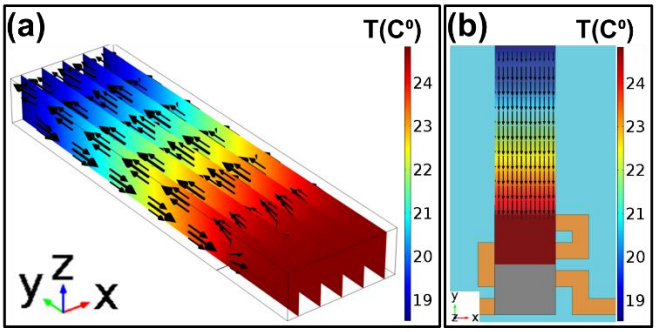

Figure 4.4 3D model of the coupled thermal-fluidic simulation within the reservoir. (a) 3D view and (b) 2D view of the reservoir and showing the fluid field velocities on the device surface using the arrows. In both (a) and (b) the color map indicates temperature distribution of the fluid on top of the device up to 1 mm away from the permalloy, and the arrows represent fluid velocity fields, where the size of each arrow is proportional to the magnitude of the fluid velocity in that region.

To further investigate the effect of heat-driven transport of particles, micro-electromagnets with identical footprints were fabricated on silicon substrates using photolithography, and an identical experimental setup was used to test these devices with MP and PS particles. The silicon wafers used were significantly thinner (360 μm) and more thermally conductive (1.3 W cm^{-1} $°C^{-1}$) compared to the shrunk polystyrene substrates used in this work, which was designed to decrease the temperature gradient induced as a

result of Joule heating. After applying the current of 30 mA to silicon devices, the PS particles remained stationary (see the supplementary multimedia files), whereas near MPs were captured at the device edge (see the supplementary multimedia files), further suggesting that natural advection was responsible for the attraction of non-magnetic particles.

4.5 Conclusions

We developed an active/passive on-chip electromagnet using rapid prototyping to investigate the thermal and magnetic forces exerted on micro-scale particles inside chip-based reservoirs integrated with miniaturized electromagnets. By measuring the terminal velocities of magnetic particles in this system, we observed that while the terminal velocities of the particles positioned near the electromagnet (~5 μm) were close to those predicted by multi-physics simulations, the particles positioned far from the electromagnet (~50 μm) moved with a terminal velocity that was about two orders of magnitude larger than predicted by simulation. We further measured the terminal velocities of non-magnetic particles and observed that their movement was also modulated by the applied current, and their terminal velocity was in the same order as the far magnetic particles. We hypothesized that thermal advection caused by the Joule heating of the electromagnet and the poor thermal conductivity of the device substrate was responsible for the movement of far magnetic and non-magnetic particles. To validate this hypothesis, we performed thermal-fluidic modelling and simulations, which confirmed the presence of advection-based fluidic flow in the system considering the measured temperature differences in the reservoir. Additional experiments using substrates that allowed enhanced heat dissipation, further

confirmed this hypothesis. The conclusions presented here demonstrate that thermally-generated fluidic flow can be combined with magnetic forces to thermally collect and magnetically capture magnetic particles at a low applied current (30 mA) from locations tens of microns away from the device as opposed to only a few microns in the case of solely relying on magnetic forces. This strategy is applicable for integration into biosensing systems, where passive transport of analytes and particles through diffusion is the limiting factor for reaching application-specific response time and limit-of-detection. In addition, we expect these devices to find applications in systems where biomolecules or cells need to be sorted, extracted, and/or enriched. These applications include the sorting and enrichment of circulating tumor cells,[20] extraction of analytes such as nucleic acids inside high background media (e.g. blood),[181] and magnetic bead-based immunoassays.[182]

4.6 Acknowledgements

This study was funded by Natural Sciences and Engineering Research Council of Canada (NSERC). LS is the Canada Research Chair in Miniaturized Biomedical Devices.

4.7 Supplementary Information

Authors: Amin Hosseini, David N. Philpott and Leyla Soleymani

Publication: Lab on a Chip, 17, 23, 4097-4104

Publication Date: October 2017

Reprinted from [171], with permission from The Royal Society of Chemistry, Copyright (**2017**). **Supplementary multimedia files (**http://dx.doi.org/10.1039/C7LC00825B):

S1-PS device with MPs: A 20 μL drop containing 2.8 μm magnetic particles was placed on a benchtop fabricated device having a polystyrene substrate, and a current of 30 mA was applied. The experiment was conducted under an optical microscope equipped with a scientific camera to record and monitor the motion of the particles in real-time. The video was expedited after recording by 32 times.

S2-PS device with PS particles: A 20 μL drop containing 2.6 μm non-magnetic polystyrene particles was placed on a benchtop fabricated device having a polystyrene substrate, and a current of 30 mA was applied. The experiment was conducted under an optical microscope equipped with a scientific camera to record and monitor the motion of the particles in real-time. The video was expedited after recording by 32 times.

S3-Silicon device with MPs: A 20 μL drop containing 2.8 μm magnetic particles was placed on a lithographically-fabricated device having a silicon substrate, and a current of 30 mA was applied. The experiment was conducted under an optical microscope equipped with a scientific camera to record and monitor the motion of the particles in real-time. The video was expedited after recording by 32 times.

S4-Silicon device with PS particles: A 20 μL drop containing 2.6 μm non-magnetic polystyrene particles was placed on a lithographically-fabricated device having a silicon substrate, and a current of 30 mA was applied. The experiment was conducted under an optical microscope equipped with a scientific camera to record and monitor the motion of the particles in real-time. The video was expedited after recording by 32 times.

S5-PS device with MPs-no applied current: A 20 μL drop containing 2.8 μm magnetic particles was placed on a benchtop fabricated device having a polystyrene substrate, and

no electrical current was applied. The experiment was conducted under an optical microscope equipped with a scientific camera to record and monitor the motion of the particles in real-time. The video was expedited after recording by 32 times.

S6-PS device with PS particles-no applied current: A 20 μL drop containing 2.6 μm non-magnetic polystyrene particles was placed on a benchtop fabricated device having a polystyrene substrate, and no electrical current was applied. The experiment was conducted under an optical microscope equipped with a scientific camera to record and monitor the motion of the particles in real-time. The video was expedited after recording by 32 times.

Chapter 5 Separation of Magnetically Labeled Baker's Yeast Cells through a Straight Microchannel using Benchtop Fabricated Micro-Electromagnets

Chapter Introduction (Objective C)

Capture and release of magnetically-labelled cells in a continuous flow is usually performed to either debulk heterogeneous cell populations[183] or separate target cells from biological fluids.[184] This chapter focuses on integrating the developed benchtop-fabricated active-passive magnetic device (chapter 3 and 4) with microfluidic channels to capture and release magnetically-labelled yeast cells under a continuous flow with an applied current of 30 mA. The active-passive device is composed of a permalloy strip coupled with a current-controlled micro-electromagnet. The electrodeposited permalloy layer, with high relative permeability, becomes magnetised when current passes through the micro-coil, and captures MPs-yeast complexes flowing in a direction perpendicular to the permalloy length. Due to the low magnetic coercivity of the permalloy structure, it becomes demagnetised when the current is OFF, and releases the MPs-yeasts in continuous flow. This study indicates the possibility of using these platforms for separation of rare cells such as CTCs by incubating cell suspensions with MPs, coated with specific antibodies that target epithelial or endothelial cells;[184] the magnetically labelled cells can be captured and released using the prototyped active-passive device.

Authors: Amin Hosseini and Leyla Soleymani

Publication: To be submitted in 2019

5.1 Abstract

On-chip cell separation is a crucial step of LOC devices. Magnetophoretic cell sorting in a continuous flow offers many advantages over marker-free and affinity-based separation techniques including the availability of MPs with various coatings and sizes, biocompatibility, high throughput, and integrability. The required magnetic force to separate magnetically tagged cells can be generated using permanent magnets, magnetized ferromagnetic micro/nano-structures (passive), micro-electromagnets (active), or a combination of these magnetic sources (active-passive). Here we combine active and passive devices, by coupling micro-electromagnets with ferromagnetic materials–to generate a sufficient magnetic force to tarp labelled cells in a free-flow with a relatively low current, while the captured cells can be easily released by turning off the current. We integrate the previously developed benchtop-fabricated active-passive magnetic device with microfluidic channel to capture and release magnetically labelled yeast cells in a continuous flow with an applied current of 30 mA.

5.2 Introduction

In many diagnostic laboratories, a primary step in sample preparation is the separation and enrichment of rare cells from a heterogenous sample (e.g. blood).[185] On-chip microfluidic bio-separation platforms have shown great promise in sorting and concentrating rare cells, due to many advantages including their miniaturized dimensions, small sample and reagent volume requirements, low cost, portability, and rapid sample-to-response time.[22], [186] On-chip cell separation mechanisms function based on the

distinguishing physical properties of cells or their carriers. Some of these physical criteria include size,[52] motility,[53] hydrodynamic,[22] electric charge,[54] electric dipole moment,[55] optical,[56] and magnetic properties.[43] Magnetophoretic cell separation has been demonstrated by employing permanent magnets,[187] ferromagnetic micro/nano-structures (passive devices),[27] current-carrying micro-electromagnets (active devices),[188] or a combination of these systems (active-passive devices)[189] to apply a force on magnetically labelled cells,[21] magnetically responsive cells,[184] or cells suspended in ferrofluid.[190] In the case of MP-based cell isolation, biomolecules on cell surfaces have been exploited to create binding events between cells and superparamagnetic particles.[183] Magnetic separation has some unique merits over other techniques. Since the magnetic field is applied externally, it can easily be removed, and thus this method can be used to capture and release target cells. Also, due to mild and non-destructive nature of the magnetic separation, this method can sustain cell viability for further analysis. In addition, the magnetic force is independent of surface charges, ionic strength, and pH of the sample solution. Furthermore, separation of magnetically labelled cells in a continuous flow enhances the device throughput and make it possible to integrate the system with other components of a lab-on-a-chip (LOC) systems.[78]

The idea of free-flow magnetic cell sorting (MACS) using permanent magnets was first developed by Miltenyi *et al.*[21] Due to advancements in microfabrication technologies, researchers have been able to miniaturize MACS systems into a single microchip to separate magnetically-tagged cells from unbound cells in a continuous flow.[191] Besant *et al.* developed a microfluidic separation platform for trapping

magnetically tagged cancer cells by locally reducing the linear velocities of the labelled cells using velocity valleys. These velocity valleys are composed of multiple X-shaped micro-barriers within the microchannels to momentarily slow down the movement of cells through the channel and capture the magnetically tagged cells using an array of permanent magnets.[187], [192] It has been shown that miniaturized magnetic materials can generate regions of high magnetic field gradient, which enhance the magnetic force acting on suspended magnetic objects.[27]–[30] Using this idea, researchers integrate microfabricated ferromagnetic structures, such as nickel or permalloy, with microfluidic channels to magnetically separate cells.[27] Adams *et al*. integrated arrays of micropatterned nickel structures into a microfluidic device to develop a multiplexed cell separation system. In this design, the dependence of the magnetic force on the volume of the MPs is exploited to capture cells tagged with larger or smaller MPs in separate zones. [193] Even though these passive devices are simple to operate, they have limitations such as reliance on permanent magnets and complexities involved in automation and integration into LOC systems.

Current-carrying micro-conductors also generate localized magnetic field gradients when electric currents flow through them.[109] Lee *et al.* implemented a miniaturized integrated circuit chip comprising a matrix of spiral-shaped micro-electromagnets, current sources and control electronic components; the chip was able to manipulate each magnetically tagged cell individually with high spatial resolution.[188] Although active devices are applicable for integration into LOC devices, the magnitude of the generated magnetic force is only effective on the surface of the device. One way to enhance the

magnetic force beyond the device surface is to increase the applied current.[110] However, increasing the applied current presents a trade-off between increasing the magnetic force and the amount of Joule heating. Combining current-carrying micro-electromagnets with ferromagnetic materials on a single chip (active-passive devices) can potentially enhance the magnetic force at a relatively low current (e.g. 30 mA). Ferromagnetic materials, with high relative permeability, behave as magnetic flux guides to concentrate magnetic field lines (generated by micro-coils) to narrow and sharp regions of the ferromagnetic structures (e.g. the edges), creating regions of high magnetic flux densities and gradients, and thus increasing the magnetic force. Song *et al.* combined the active and passive magnetic elements to develop a multilayer magnetic cell sorting device, composed of six spiral micro-coils semi-embedded in an electrodeposited nickel structure. This microfluidic magnetic sorting device offers a separation efficiency of up to 95.3%, under flow rate of 5 µl/min. Despite of the its high sorting efficacy, this device requires a relatively large current to function (0.5-1.5 A). To avoid a thermal breakdown as a result of Joule heating, they integrated a microfluidic cooling system into the device. The device was fabricated on a silicon wafer using standard techniques such as photolithography, lift-off, and electroplating.[117]

Previously, we employed the heat shrinking principle to fabricate a low-powered miniaturized active-passive magnetic separation device using simple, low-cost, rapid, and benchtop prototyping techniques.[97], [171] In this paper, we successfully integrated the device with polydimethylsiloxane (PDMS)-based microchannel and were able to capture magnetically labelled yeast cells under flow rate of 1 µl/min with an applied current of 30

mA. Such a low-current of operation is achieved through addition of micro/nano-wrinkled structures onto the surface of the current-carrying micro-electromagnet, which generates region of high magnetic field gradients. Moreover, integration of the micro/nano-structured electromagnet with a permalloy ($Ni_{80}Fe_{20}$) layer (with relative permeability of ~ 4000) results in rapid magnetization of the permalloy as the current passes through the micro/nano-textured conductor. The permalloy layer concentrates the magnetic field lines to its edges and creates regions of high magnetic flux densities and field gradients, where magnetically tagged cells are captured.[97] Due to the small operational current and free-flow of MPs-yeast suspension through the channel, no cooling system was required for heat dissipation.

5.3 Experimental

5.3.1 Yeast Cells Preparation and Modification with Magnetic Particles

The experiments were implemented by suspending 1.6 mg/ml of Fleischmann's traditional active dry yeast, also known as *Saccharomyces cerevisiae* yeast cells (Fleischmann's, Mississauga, Ontario), in 50 ml of 1X PBS (phosphate buffered saline) solution containing 1.6 mg/ml of tris(hydroxymethyl)aminomethane. pH of the buffer was adjusted to ~7.4 using 2 M of hydrochloric acid. The suspension was incubated for one hour at 30°C.

Meanwhile, 1.05 µm Dynaebeads MyOne Carboxylic Acid MPs (Invitrogen Corporation, Burlington, Ontario) were activated using Concanavalin-A (Sigma-Aldrich, Saint Louise, Missouri), a protein from lectin family that binds to sugar molecules (α-D-mannose) on the yeast cell's surface,[194] according to the following procedure: 30 µl of

MyOne MPs stock solution (10 mg/ml) was washed twice with 0.01 M sodium hydroxide (NaOH) and three times with Milli-Q water at room temperature. All the washing steps mentioned in this section include centrifugation for 4 minutes at 13K rpm followed by removing the supernatant using an external magnet and resuspending the MPs/MPs-yeast cells in a fresh buffer. Meantime, 20 mg/ml solution of EDC (N-(3-dimethylaminopropyl)-N′-ethylcarbodiimide) was prepared in cold (~ 4 °C) 25 mM MES (2-(N-morpholino) ethanesulfonic acid) buffer with pH of 6 (pH of 25 mM MES was adjusted using 2 M of NaOH). The prepared EDC solution was then added to the MPs solution and vortexed for 30 minutes at room temperature. After that the supernatant was removed using an external magnet and the MPs were washed once with Milli-Q water and twice with the cold 25 mM MES buffer with pH of 6. Shortly after that 1.8 mg of Concanavalin-A was dissolved in 1 ml of the cold 25 mM MES (pH ~ 6), then incubated and gently agitated with the MPs for two hours at room temperature. Subsequently, the functionalized MPs were washed with 1X PBS buffer (pH ~ 7.4) containing 0.05% Tween-20 (BioShop, Burlington, Ontario).[195]

Finally, 500 µl of the prepared yeast cell suspension was mixed and incubated with the Concanavalin-A labeled MPs for at least 20 minutes at room temperature on an orbital shaker at 350 rpm. After that, the suspension was washed three times with 1X PBS buffer to filter out the unbound yeast cells.[195] Prior to experiments, the MPs-yeast solution was diluted 10 times with 1X PBS buffer containing 1% Tween-20.

5.3.2 Fabrication and Integration of the Micro-electromagnet and Microfluidic Channel

The fabrication process of the micro-electromagnet is shown in Figure 5.1. First, 55 × 55 mm^2 pre-strained polystyrene (PSPS) sheets (Graphix Shrink Film, Graphix, Maple Heights, Ohio) were cleaned by shaking the films for 10 minutes in isopropanol and Milli-Q water, and dried with clean dry air (Figure 5.1, i). Next, self-adhesive vinyl sheets (FDC 4304 Easy Removable sign vinyl, BDF, Graphics, Toronto, Ontario) were laid and flatten on the PSPS using a hand roller (Figure 5.1, ii). The mesh-shaped meandering design of the micro-electromagnet with minimum feature size of 200 μm was patterned into the attached self-adhesive vinyl using the Robo Pro CE5000-40-CRP cutter (Graphtec America Inc., Irvine, California) (Figure 5.1, iii). A copper thin film (100 nm) was sputtered onto the masked PSPS from 99.999% purity copper target (Kurt J. Lesker Company, Concord, Ontario) using a Torr Compact Research Coater CRC-600 manual planar magnetron DC sputtering system (Torr International Inc., New Windsor, New York) (Figure 5.1, iv). After peeling off the vinyl masks the macro-scaled meandering electromagnet was obtained (Figure 5.1, v). The meandering copper-coated substrates were placed on a pre-heated (160 °C) flat aluminum block inside an oven (BINDER, GENEQ Inc., Tuttlingen, Germany), heat treated and shrunk for 3 minutes (Figure 5.1, vi). After shrinking, the contact pads were covered using scotch tapes and the devices were rinsed with ethanol and Milli-Q water, dried with nitrogen stream, and placed on a hotplate at 60 °C for 30 minutes. After cooling down the device to the room temperature, the negative photoresist SU-8 2007 (MicroChem, Newton, Massachusetts) was spun on the device surface at 1000 rpm for 30 seconds. The devices were soft baked at 95 °C for three minutes, and then UV light exposed

with dosage of 140 mJ/cm^2. The devices were post exposure baked for 20 minutes at 95 °C. Next, second SU-8 2007 layer was spun at 2500 rpm for 30 seconds, and soft baked at 95 °C for two minutes. The UV expose and thermal cross-linking of the SU-8 was done as it was explained before. Following that, an adhesion promoter, Hexamethyldisilazane (HMDS) (Technic, Cedex, France) was spun on top of the cured SU-8 at 3000 rpm for 30 seconds and soft baked for three minutes. After fabricating the insulating layer (SU-8), the tapes covering the contact pads were carefully removed using tweezers (Figure 5.1, vii). To fabricate the passive portion of the device, a rectangular shaped mask (2.28 × 18.16 mm^2) was patterned on the self-adhesive vinyl using the craft cutter, peeled off, aligned, and laid precisely on the device surface (Figure 5.1, viii). Next, 20 nm of gold was sputtered onto the device surface creating a conductive patterned seed layer (Figure 5.1, ix-x). This conductive seed layer defined the base for electroplating the permalloy layer. A new self-adhesive vinyl mask with a rectangular window (2.28 × 0.61 mm^2) was patterned, carefully aligned with the underlaying seed layer, and laid on the device surface for permalloy electrodeposition (Figure 5.1, xi). A thin (~ 1 µm) permalloy layer was electroplated through the window using a CHI660D electrochemical workstation (CH Instrument, Austin, Texas) and a standard three-electrode set-up consists of an Ag/AgCl reference electrode, a platinum mesh counter electrode, and the PS device as the working electrode (Figure 5.1, xii). The electrolyte, used for the permalloy electrodeposition, contained 0.95 M nickel(II) sulfate hexahydrate, 18 mM iron(II) sulfate heptahydrate, 0.4 M boric acid, 4.87 mM sodium saccharin, and 0.35 mM sodium dodecyl sulfate (Sigma-Aldrich, St. Louis, Missouri). The permalloy electroplating was performed at room temperature using

chronopotentiometry technique with a constant current density of 5 mA/cm^2 for 470 seconds. After the plating, the vinyl mask was gently removed, the device surface was rinsed with Milli-Q water and dried with clean dry air. Finally, A 50 nm of silicon dioxide was sputtered on the patterned structures of the device as a protective layer (Figure 5.1, xiii).

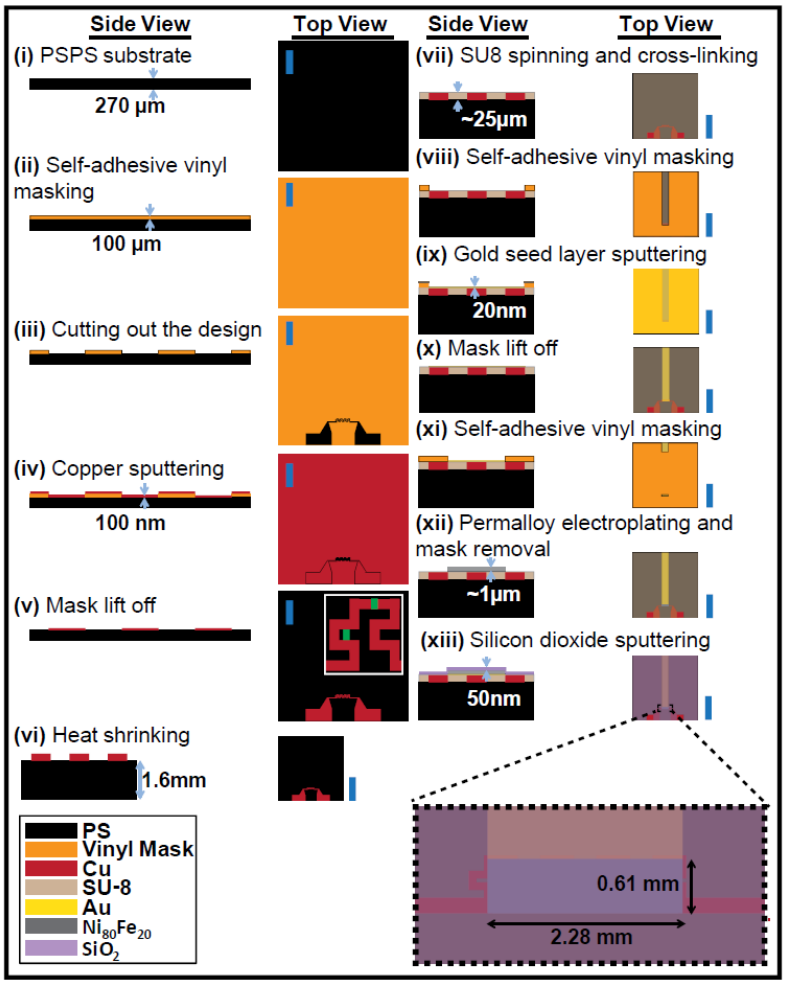

Figure 5.1 Top-and side-view schematic of the device fabrication process. All scale bars represent 10 mm, except the scale bars in the insets which represent 200 µm (step v).

The micro-channel fabrication and integration process is shown in Figure 5.2. PDMS micro-channels were fabricated from Sylgard 184 Silicon Elastomer Kit (Dow

Corning Corporation, Midland, Michigan). The elastomer base and the curing agent were fully mixed in 10:1 ratio, then degassed using a desiccator and a pump. To prepare the mold, two sheets of self-adhesive vinyl were laid over a cleaned PSPS sheets and evenly flattened with a hand roller (Figure 5.2, i-ii). The channel was designed in Adobe Illustrator, patterned on top of the attached vinyl sheets using the craft cutter, and carefully peeled off using tweezers (Figure 5.2, iii). The length, width, and height of the channel were designed to be ~ 15.5, 1, and 0.2 mm respectively. The prototyped mold was immobilized inside a Petri dish using double sided tape and the degassed PDMS mix was poured evenly on top of the mold and cured inside a vacuum chamber at room temperature for > 24 hours (Figure 5.2, iv). After PDMS was cured, a ~ 1 mm hole was made at the inlet of the channel while still sitting on the mold. Next, the cured PDMS was carefully cut out and lifted from the mold using a razer blade, (Figure 5.2, v). To bond the channel and device together, the cured PDMS bonding side along with the device surface were air plasma treated using Harrick Plasma machine (Ithaca, New York) on HIGH RF setting, at the air flow of 30 sccm for 60 seconds. The treated device and PDMS channel surfaces were brought into physical contact shortly after the plasma cleaning (Figure 5.2, vi). A 1 mm (OD) tube was inserted into the 1 mm hole and secured using epoxy glue.

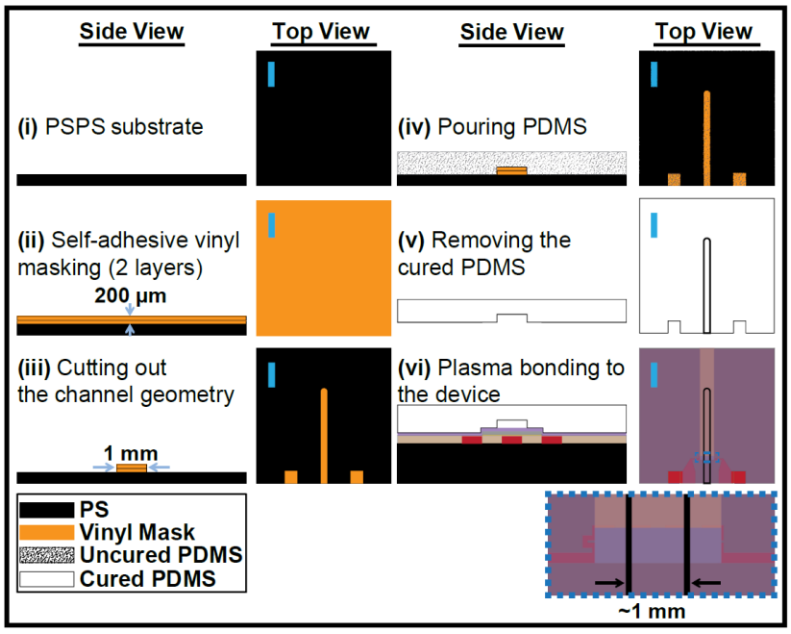

Figure 5.2 Top-and side-view schematic of the channel fabrication and bonding process. All scale bars represent 10 mm.

5.3.3 Experimental Setup for Separation of the Magnetically Labeled Yeast Cells

Prior to experiments, the channel was filled with 1% bovine serum albumin (BSA) (Sigma Aldrich, Germany) mixed with 1% Triton X-100 (Sigma-Aldrich, Saint Louise, Missouri), in 1X PBS (pH ~ 7) for 2 hours at room temperature. After treating the channel walls and device surface with the blocking agents, the channel was flushed with the Milli-Q water. Next, MPs-yeast cells suspension was injected into the channel using a syringe pump at a constant flow rate of 1 µl/min. When the flow within the channel became stable, we started recording the motion of magnetically tagged yeast cells for 10 minutes with the current OFF, and subsequently for another 10 minutes with the current ON (30 mA). The current was applied to the contact pads of the device using a power supply (Keithley Instruments, Cleveland, Ohio). The entire experiment was conducted under an optical microscope (Nikon, Mianto, Tokyo, Japan) equipped with a Retiga 2000R scientific camera

(Q Imaging, Surrey, British Colombia) to record and monitor the flow of the MPs-yeast cells in real time. Next, we turned off the current and washed off the captured magnetically labelled yeasts by flowing Milli-Q water through the channel. The control experiment was performed on the same device using unbound yeast cells in the same manner as explained before.

5.4 Results and Discussion

5.4.1 Device Architecture

In order to effectively separate magnetically labeled yeast cells in a continuous flow, the active-passive devices and PDMS channels were fabricated and integrated using the previously explained benchtop methods.[171], [196] Figures 5.1 and 5.2 summarize the fabrication steps. The devices were fabricated on square-shaped shrinkable PSPS sheets. The active part of the device consists of a meandering current-carrying copper structure. To miniaturize the device foot print (width and inter-electrode spacing) and generate the desired micro/nano copper structures, the devices were heated above the glass transition temperature of PSPS (100°C). This heat treatment results in lateral shrinkage of the device to 40% of its original size, due to polymer chain relaxation, which causes the copper film to crumple while keeping the meandering design intact.[97], [160] The induced micro/nanoscale wrinkles on the surface of the micro-electromagnet enhance the generated magnetic force due to existence of high magnetic field gradients in the vicinity of the narrow and sharp regions of the wrinkles.[29], [97] The active part of the device is isolated from the passive part (permalloy thin layer) using an insulating layer (SU-8). The thickness of the SU-8 was previously measured to be ~25 μm.[171] As the electric current passes

through the meandering micro/nano-structured copper, it magnetizes the permalloy layer.[159], [165], [178] The high relative permeability of the permalloy amplifies the magnetic flux density, magnetic field gradients, and consequently the acting force on the magnetically labelled yeast cells.[97] After permalloy electrodeposition,[97], [161], [162], [164] a 50 nm of silicon dioxide was sputtered on the device surface to protect the electrodeposited permalloy from direct physical contacts with the sample mixture, reduce the non-specific adhesion of both MPs and yeasts to the device surface[195], and simplify the bonding procedure between the PDMS channel and the device surface.

To effectively transport the magnetically labelled yeast cells toward the localized magnetic field gradient hotspots, a PDMS fluidic system was designed, prototyped, and bonded to the device surface. PDMS is extensively employed to fabricate the micro-channels because of its benign mechanical/optical properties and its straightforward casting using rapid prototyping.[197] Here, we used a benchtop fabrication method to create the mold for creating fluidic channels into PDMS.[196] A plastic sheet masked with self-adhesive vinyl was patterned using the craft cutter to define the fluidic channel. After casting the PDMS layer onto the vinyl mold, curing it, and removing it from the mold, it was plasma bonded to the silicon dioxide layer of the device and the system's inlet and outlet were defined. The channel was aligned with the device such that the flow direction was perpendicular to the length of the permalloy edges (capturing site) as shown in the inset of Figure 5.2 vi.

5.4.2 Separation of magnetically-labeled yeast cells in a continuous flow device

To test the performance of the benchtop-fabricated microfluidic device, we designed an experiment to capture magnetically-tagged yeasts in a continuous flow. Saccharomyces cerevisiae yeast cell is a eukaryotic organism, which is used in pharmaceutical and chemical industries in the areas of drug discovery[198] and chemical production.[199] Each yeast cell was tagged with multiple MPs (Figure 5.3b-inset). Having multiple MPs per cell is expected to enhance the magnetic force acting on the tagged cell. Figure 5.3(a) displays the top and side views of the device. The solution containing the MPs-yeasts complex was injected into the channel at a flow rate of 1 µl/min. For the first 10 minutes, no electric current was applied to the device and MPs-yeasts were freely passing the capturing sites. Immediately after, a 30 mA DC current was applied to the micro-electromagnet, which resulted in changing the trajectories of the magnetically labeled cells and trapping them along the lengths of the permalloy (see the supplementary multimedia files). After 10 minutes with current ON, a clear aggregation of MPs-yeasts composite was observed on both sides of the permalloy (Figure 5.3b). This behaviour was expected due to the high magnetic flux density and field gradient along the edges of the permalloy.[97], [171] Moreover, gradual accumulation of MPs-yeasts along the edges of the permalloy boosted the capturing rate due to summation of the magnetic moments. Afterwards, we turned off the current and released the captured MPs-yeasts by applying a flow of DI water into the channel. Due to superparamagnetic nature of MyOne beads, their average magnetization returned to zero shortly after the external magnetic field was turned off. The ability of releasing the cells after trapping them is particularly important for

downstream biosensing and analysis.[187] For the control, the same experiment was repeated but this time with unbound yeasts (Figure 5.3c). As it was expected, no yeast cells were trapped. These results indicate that this microfluidic magnetic device can be used for the applications that require capture and release of the target cells or biomolecules. Most of the reported micro-electromagnetic devices require an additional cooling component to control the effect of Joule heating, however the system reported here does not need the cooling system due to the constant flow of the sample fluid and relatively low operational current (30 mA).

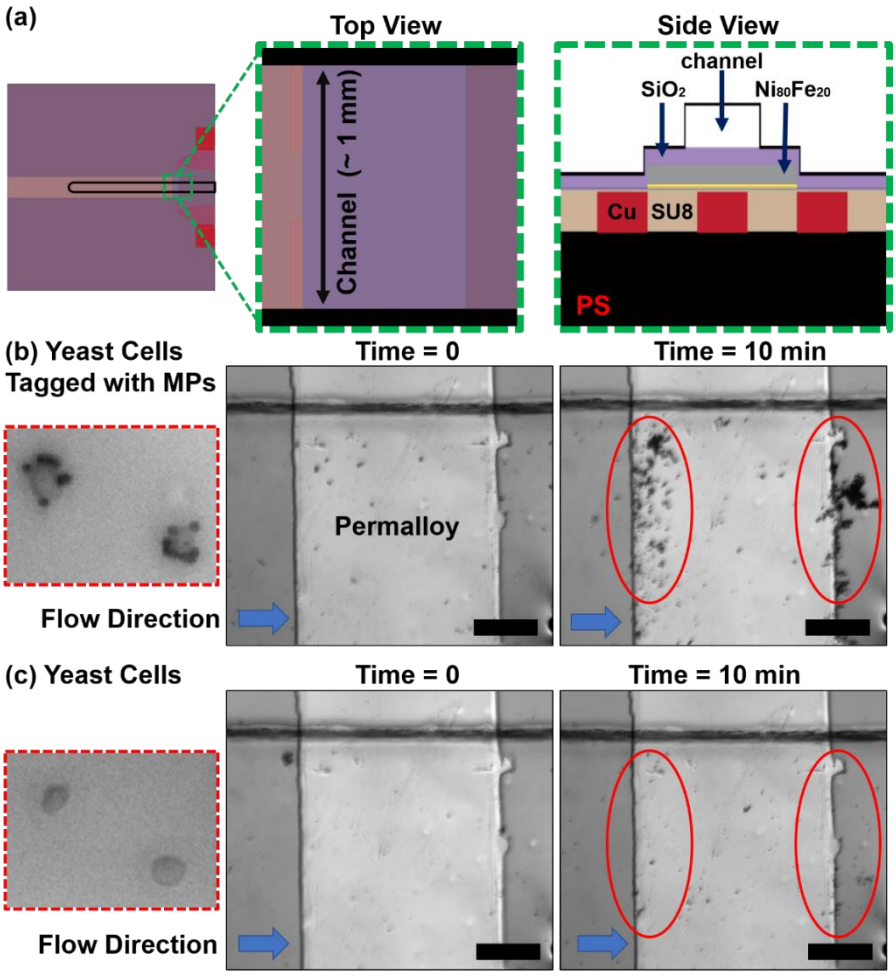

Figure 5.3 Capturing the magnetically tagged yeast cells in a continuous flow using the benchtop fabricated micro-electromagnet. (a) schematic of the device. The insets are the top and side view schematic of the device capture site. (b) and (c) display the optical microscopy images of the device capture site before (*time = 0*) and after applying the current (30 mA) for 10 minutes, while suspended magnetically labelled yeast cells (b) or unbound yeast cells (c) were flown into the channel at the flow rate of 1 µl/min. The insets are the zoomed-in images of yeast-MPs complex (b) and unbound yeast cells (c). The scale bar represents 100 µm.

5.5 Conclusions

In summary, we effectively integrated the previously reported benchtop-fabricated active-passive magnetic device with microfluidics to capture and release magnetically

tagged yeast cells in a continuous flow with an applied current of 30 mA, while unlabeled yeasts were freely flown through the channel without being trapped. The effect of Joule heating was insignificant because of the relatively low current and continuous flow of the sample buffer over the surface of the micro-electromagnet. For the next step, the optimum throughput and capture efficiency of these devices will be determined. To improve the throughput and capture efficiency of the device, we can decrease the height of the channel to bring the flowing analytes closer to the capture sites. However, since the linear velocity is increased by reducing the cross-section of the channel, the generated magnetic force may not be large enough to immobilize the tagged cells. To compensate for that we envision to integrate permalloy micro/nano-structures into the channel walls to enhance the capture efficiency of the device. Although the obtained experimental results are preliminary, they indicate the possibility of using these platforms for separation of rare cells such as CTCs. One major challenge of working with body fluids is the non-specific adhesion of cells or proteins to the device and channel surfaces. In the next chapter, we introduce a lubricant-infused coating which decreases the non-specific adhesion of proteins or cells. This lubricant-infused coating can potentially be applied to the magnetic device surfaces and channel walls to prevent blockage of the microfluidic device.

Chapter 6 Conductive Electrochemically Active Lubricant-Infused Nanostructured Surfaces Attenuate Coagulation and Enable Friction-Less Droplet Manipulation

Chapter Introduction (Objective D):

Separation of magnetically labelled cells from a heterogeneous biological sample with high viscosity using the benchtop fabricated magnetic device, can be challenging due to the non-specific adhesion and high magnetic force requirement. This chapter looks into developing lubricant-infused slippery surfaces, which can solve these problems. The principle of this slippery surfaces is based on locking biocompatible lubricants onto self-assembled monolayers (SAMs) of hydrophobic fluorosilane. We create two classes of fluorosilanized conductive wrinkled surfaces fabricated on PSPS substrates; one is used for electrochemical measurements, and the other one contains an additional integrated ferromagnetic (permalloy) structures for manipulation of magnetic microdroplets. PSPS sheets were employed due to their shrinking property, which results in generation of electrochemically active wrinkled metallic micro/nano structures. The slipperiness of these surfaces is verified through sliding angle measurements (<5°) and manipulation of superparamagnetic microdroplets. The electrochemical and charge transfer properties of the fluorosilanized lubricant-infused gold surfaces are evaluated through cyclic voltammetry (CV) and electrodeposition of palladium micro/nanostructures, respectively. The obtained CV curves show the distinct redox signature of ruthenium hexamine complex within the electrolyte solution. Successful electrochemical measurements and electrodeposition of palladium through lubricant layers indicate the possibility of using these surfaces for electrical sensing applications. The self-cleaning property of these

surfaces is confirmed using a blood plasma coagulation assay. These modified surfaces can be applied to LOC components such as microfluidics, magnetic separation, and biosensing devices to reduce non-specific adhesion of unwanted analytes when dealing with complex physiological samples.

Authors: Amin Hosseini[Ψ], Martin Villegas[Ψ], Jie Yang, Maryam Badv, Jeffrey I Weitz, Leyla Soleymani, and Tohid F Didar

[Ψ] These authors contributed equally to this work.

Publication: Advanced Materials Interfaces, 5, 1, 1800617

Publication Date: July 2018

6.1 Abstract

Micro/nanostructured materials and lubricant-infused surfaces, both inspired from structures found in nature, are ideally-suited for developing self-cleaning and high surface area transducers for biosensing. These two classes of bio-inspired technologies are integrated to develop lubricant-infused electrodes designed to reduce biofouling. Chemical vapor deposition is used to create self-assembled monolayers of fluorosilane on gold-modified pre-strained polystyrene substrates. After heat shrinking of the substrate, a lubricant is applied to produce a lubricant-infused nanostructured gold wrinkled surface with hydrophobic properties. These electrically conductive surfaces demonstrate high water contact (~150°) and low sliding angles (<5°). Moreover, combining these surfaces with passive magnetic actuators, enables the actuation of superparamagnetic microdroplets in frictionless and open channel conditions without needing full droplet submersion in an

immiscible fluid. The fabricated nanostructured surfaces resist protein adhesion in a human plasma coagulation assay and significantly prolong clotting times and retain electrical conductivity, which is essential for electrical sensing applications. The developed hybrid interfaces are expected to have a wide range of applications in biosensing and biological sample preparation involving complex clinical and environmental samples.

6.2 Introduction

Electrical sensors and transducers are essential components of a wide range of biomedical systems such as point-of-care diagnostics, wearable/implantable sensors, lab-on-a-chip, organs-on-chips, and various biosensing platforms, most of which are subject to complex biological samples and prone to non-specific adhesion of biological matter (*e.g.*, proteins, cells, *etc.*). Non-specific adhesion of undesired biospecies is associated with complications such as blood clot formation, false positive diagnostic results, decreased signal-to-noise ratios of sensors, and biofouling,[120], [201]–[209] and has complicated the commercialization of biosensors and lab-on-chip devices.

Lubricant-infused coatings developed based on tethering biocompatible lubricants onto self-assembled monolayers (SAMs) of hydrophobic organosilanes have proven to be highly effective for minimizing non-specific adhesion.[119], [120] These lubricant-infused surfaces were first reported by Wong *et al.*,[121] where a lubricant layer was locked on the surface using a combination of surface topography and chemical modification. Leslie *et al.*[122] reported generating lubricant-infused surfaces solely based on chemical modification with fluorine-based silanes, independent of surface topography. Since the conception of these ideas, researchers have investigated different materials, strategies and

applications for the fabrication and utilization of lubricant-infused surfaces. The typical strategies involve: rendering a material hydrophobic through chemical coatings, inducing micro/nano textures on low-surface-energy materials, or a combination of these methods.[123] These strategies have proved to be compatible with several classes of materials, including polymers,[121], [122], [210]–[212] wood,[213] silicon,[125], [214]–[216] glass,[211], [217] metals[126], [218]–[223] and metal oxides.[125], [224], [225] These surfaces have displayed exceptional self-cleaning and self-healing properties,[121], [124], [226] with additional functionalities for practical applications, for example: increased mobility for acoustic actuation[125] and electrowetting;[220], [225] enhancing surface quality,[227] anti-corrosion,[126], [219] anti-icing,[215], [221], [228] enhanced condensation,[229] as well as, anti-fouling implementations.[230]–[232] Furthermore, these coatings significantly outperform the most widely-used FDA-approved surface treatments, including heparin-coated surfaces, as well as a range of different hydrophilic coatings developed to resist blood clot formation;[233] surpassing the performance of poly(ethylene glycol) (PEG),[234] bovine serum albumin (BSA), and fetal bovine serum (FBS), all of which have poor performance as coatings for preventing blood coagulation.[235] Therefore, evidence from the scientific literature on the prevention of nonspecific adhesion in complex environments suggests that lubricant-infused surfaces are a viable option for adoption into interfaces used in biomedical devices.

In this paper, we introduce for the first time, lubricant-infused coatings applicable to electrical sensing. Since surface topography plays an important role in locking the lubricant layer, we predicted that conductive lubricant-infused surfaces based on

micro/nanostructures would serve a dual purpose: they will enhance the electrode surface area[236] and contribute to the hydrophobic properties of the surface. To better understand the physical and electrical properties of micro/nanostructured electrodes with an integrated liquid-infused coating, we used wrinkled gold electrodes created on shape memory polymer substrates as the conductive layer. These electrodes were previously shown to have features that were tunable in the micro/nanoscale,[237] and were used to enhance the signal-to-noise ratio and sensitivity of biosensors.[160], [238]–[240] Using these wrinkled electrodes, we developed conductive lubricant-infused nanostructured surfaces (henceforth referred to as CLINS) and characterized their physical and chemical surface properties using x-ray photoelectron spectroscopy (XPS), contact and sliding angle measurements, surface-based magnetic droplet manipulation, and electrochemical methods. After confirming the hydrophobicity, slippery and electrical conductivity of these surfaces, hemocompatibility was assessed using human blood plasma. These studies demonstrated that CLINS significantly attenuate non-specific protein adhesion and blood clot formation while providing adequate charge transfer for electrochemical assays. With these properties, we expect that CLINS will provide an innovative platform for settings where electrodes come in direct contact with complex biological samples, such as, lab-on-chip and wearable diagnostic devices.

6.3 Results and Discussion

6.3.1 Fabrication of CLINS

A fabrication process was developed that integrates nanostructured metallic surfaces with perfluorinated coatings. For this purpose, two different material architectures were implemented on shape memory polymer substrates (**Figure 6.1)**. The first combined wrinkled gold films with perfluorinated coatings (Figure 6.1, left), whereas, the second included an additional ferromagnetic layer (Figure 6.1, right). To achieve the first material architecture, a 20 nm gold film was sputtered onto a pre-strained polystyrene (PSPS) substrate, and both the structural and chemical properties of the gold film were modified in order to engineer its slippery properties (high water contact angle ~150º and low sliding angle <5º). First, chemical modification was performed by treating the samples with oxygen plasma to activate the gold surface and enable its reaction with fluorosilane. Chemical vapor deposition (CVD) was then employed to deposit a SAM of Trichloro (1H,1H,2H,2H-perfluorooctyl) silane (TPFS) onto the gold surfaces for a minimum of 1 hour. Thereafter, the devices were heated at 60ºC overnight to create covalent bonds between the silane and the gold substrate. Subsequently, to generate the wrinkled micro/nano-structured gold surfaces, fluorosilanized gold-coated PSPS films were heated at 160 °C for three minutes. Heating PSPS above its glass transition temperature of 100 °C laterally shrinks the substrate to about 40% of its original size and increases its thickness over 6-fold due to polymer chain relaxation. The generated stress from shrinking causes the thin gold film to crumple, thereby creating wrinkled micro/nano structures.[97], [160] Previous scotch tape adhesion tests demonstrated that the wrinkled gold layer on

polystyrene could not be removed after the shrinking and wrinkling process. In addition cross sectional characterization using transmission electron microscopy (TEM) demonstrated a conformal wrinkled interface between the polystyrene and gold.[236] After the shrinking process, a biocompatible lubricant (perfluorodecalin (PFD) or perflourorperhydrophenanthrene (PFPP)) was added to the substrate to create the CLINS. The chemically-modified micro/nano-textured wrinkled gold film is expected to tether the lubricant onto the surface, creating a slippery and non-sticky interface.[121] The choice of lubricant was assessed based on the nature of each experiment, for example, for high droplet mobility, a low viscosity lubricant is preferred (kinematic viscosity at 25º C; PFD 2.94 cSt, PFPP 8.0 cSt).[214] On the other hand, for applications where long term stability is required, more viscous lubricants with low vapor pressure are ideal.[223]

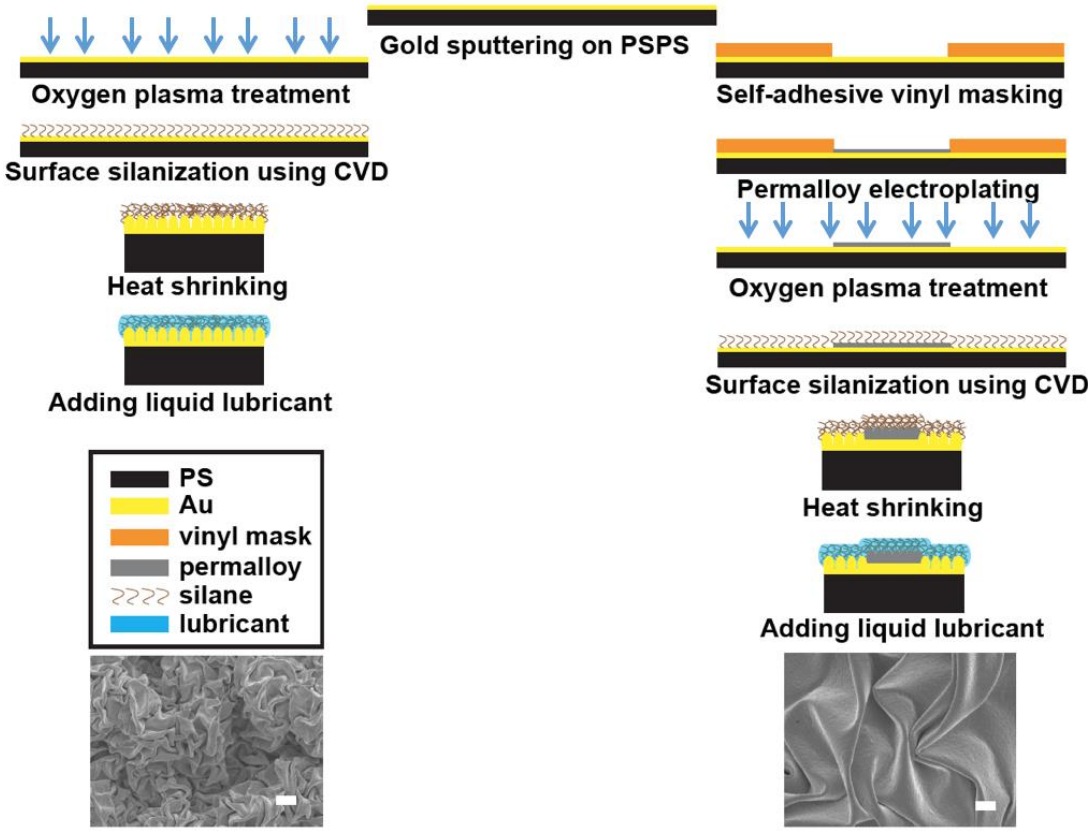

Figure 6.1 Side-view schematic of the fabrication process used in creating the conductive lubricant-infused nanostructured surfaces. The left column represents the process flow for fabricating the conductive lubricant-infused nanostructured electrodes with the SEM image showing wrinkled gold nanostructures. The right column displays the fabrication process flow of the ferromagnetic conductive lubricant-infused nanostructured electrodes with the SEM image showing wrinkled permalloy microstructures. All scale bars represent 1 µm.

The second material architecture, which included a ferromagnetic top layer, was implemented to examine the effect of CLINS on reducing interfacial friction in open channel superparamagnetic droplet manipulation. In this architecture, a triangular ferromagnetic permalloy layer was electrodeposited onto a masked planar gold surface prior to chemical modification or substrate shrinking (Figure 6.1). Triangular-shaped permalloy was chosen because magnetic field gradients were found to be enhanced at the

tip of the triangle, resulting in the generation of magnetic forces for droplet manipulation.[30], [241] The surfaces of the permalloy and gold layers were then fluorinated as described above. Heat shrinking of the PSPS causes both the gold and the permalloy layers to crumple, generating nano-sized wrinkles in the gold film and micro-sized wrinkles in the thicker permalloy-coated film (Figure 6.1). This is in line with previous reports that increasing film thickness increases the size of the wrinkles.[160], [242] In addition, higher magnetic field gradients are expected at the sharp and narrow edges of the wrinkles due to the concentrated magnetic field lines in these regions.[29] Finally, the lubricant layer was added to the chemically-modified and wrinkled metallic layers to create the CLINS substrates. Substrates of both architecture were then subjected to magnetic droplet manipulation characterization studies.

6.3.2 Chemical and Surface Characterization of CLINS

Surface functionalization with silanes has been previously reported using liquid phase deposition (LPD) or CVD.[123], [124], [223], [243]–[247] In this work, we chose the CVD process because it generates a more uniform surface coatings, it has higher effectiveness at coating the inner surfaces of porous materials such as nanowrinkles, and uses a smaller solution volume compared with the LPD process.[247]–[250] To characterize the chemical composition of the surface throughout the fabrication process and validate the functionalization of wrinkled surfaces, the gold surfaces were investigated using XPS (**Figure 6.2a**). Bare gold substrates demonstrated an abundance of gold (~38% wrinkled, ~32% planar) and carbon (~53% wrinkled, ~54% planar atoms on the surface. After treating the gold substrates with oxygen plasma, the spectra revealed a noticeable

decrease in carbon content, as well as a two-fold increase in oxygen content, indicating activation of the surface through the formation of oxygen-containing groups such as hydroxyl groups. After fluorosilane deposition, the dominant atoms on the surface were carbon (~32% wrinkled, ~35% planar) and fluorine (~56% wrinkled, ~53% planar). These findings confirm a successful CVD process for generating SAMs of TPFS, which contain long carbon chains with 13 fluorine atoms. Furthermore, the oxygen level is markedly reduced following the silanization step, which validates the reaction between hydroxyl groups and the fluorosilane. In addition, the results in Figure 6.2a display a comparable chemical composition in the planar and wrinkled surfaces, indicating that coating the surfaces prior to the wrinkling process did not affect the stability of the fluorosilane monolayer upon heat treating the samples at 160 °C. In other words, the SAM of fluorosilane remains stable on the gold surfaces following a high temperature annealing step which could be due to the fact that silane based SAMS have a high thermal stability (above 200 °C).[251]

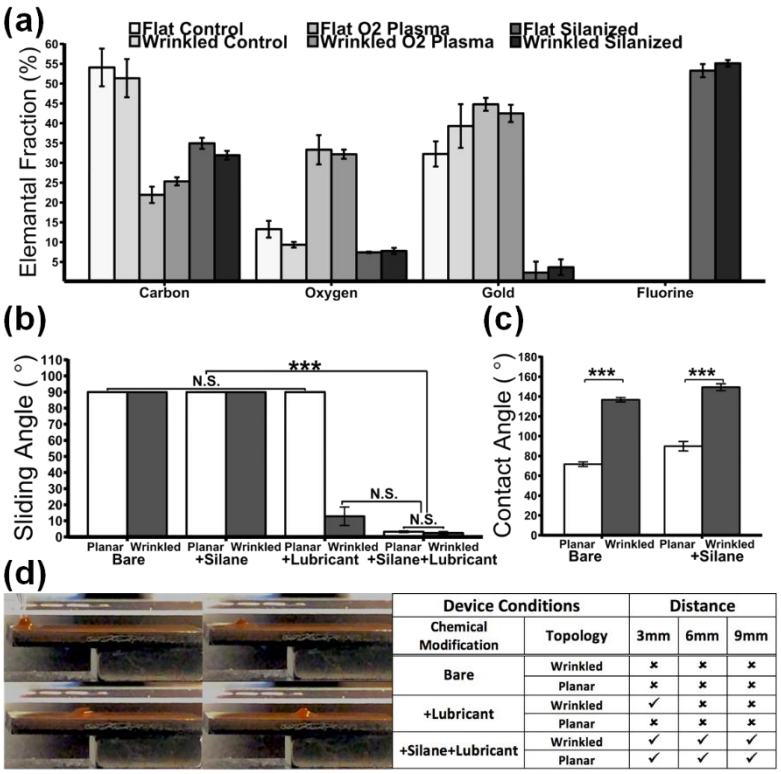

Device Conditions		Distance		
Chemical Modification	Topology	3mm	6mm	9mm
Bare	Wrinkled	×	×	×
	Planar	×	×	×
+Lubricant	Wrinkled	✓	×	×
	Planar	×	×	×
+Silane+Lubricant	Wrinkled	✓	✓	✓
	Planar	✓	✓	✓

Figure 6.2 Surface characterization of CLINS. (a) Elemental analysis of the surface of the device through x-ray photoelectron spectroscopy; using control, oxygen plasma treated and fluorosilanized samples. (b) Water sliding angles for planar and wrinkled surfaces; surfaces were tested bare, silanized only, lubricated only or silanized and lubricated, using a 5 µl water droplet. (c) Water contact angle values for planar and wrinkled surfaces; surfaces were tested bare and after silanization using a 2 µl water droplet. Significant levels are defined as: not significant 'N.S.' p-value > 0.05; significant '*' p-value< 0.05; highly significant '**' p-value<0.01; and very significant '***' p-value <0.001. (d) Timed video-frames for the superparamagnetic micromicrodroplet manipulation (left); distance of superparamagnetic microdroplet movement from triangular permalloy (right). Results in the right table were presented by successful droplet acceleration (√) or unsuccessful pinning (x). All error bars represent standard deviations.

We investigated the hydrophobic properties of CLINS using sliding and contact angle measurements. The sliding angle results (Figure 6.2b) show that surfaces lacking a lubricant layer present no droplet mobility (sliding angles above 90°) on both planar and wrinkled devices. Furthermore, when we compared planar and wrinkled surfaces

containing a lubricant layer but lacking fluorosilanization, the sliding angle was significantly lower on wrinkled surfaces than on planar devices and were partially slippery in character (sliding angles under 20° vs 90°). We suspect that this difference reflects increased surface roughness as a result of wrinkling, which creates a physical barrier that minimizes lubricant loss. Moreover, the peaks on the wrinkled surface may shield the crevices, thereby allowing the macro-sized droplets to slide with minimal interaction with the surface.[243], [252], [253] The hydrophobic characteristics were significantly enhanced on all surfaces that were fluorosilanized. The sliding angle results in Figure 6.2b demonstrated that CLINS (fluorosilanized and lubricated surfaces) exhibit excellent slippery properties as evidence by sliding angles ranging from 1 to 5°. The XPS results demonstrate that by adding the fluorosilane coating, the chemical properties closely resemble those of the lubricant. Consequently, matching the surface energy of the surface to the lubricant through fluorosilanization is expected to result in the tethering of the lubricant to the surface. The average thickness of the lubricant layer on the gold surfaces was determined based on the measured weight of the lubricant, its density, and the wetted area. The estimated thicknesses of the lubricant were 52±4.6 μm, 47±2.9 μm, 45±3.7 μm, and 39±1.3 μm for fluorosilanized wrinkled, wrinkled, silanized planar, and planar gold surfaces, respectively. The thicker lubricant layer observed on the fluorosilanized wrinkled gold surfaces indicates a higher chemical and physical affinity for the lubricant on these surfaces.

Figure 6.2c displays the water contact angles of the fabricated surfaces. These results show that creation of micro/nanoscale wrinkles significantly increases the contact

angle from less than 90° to over 140°. Micro/nanostructured gold surfaces have previously shown similar trends, whereby, a planar gold film displaying contact angles below 90° (slightly hydrophilic) become hydrophobic upon wrinkling.[160] According to Wenzel's equations, the incorporation of surface roughness should enhance the surface wettability properties (*i.e.* creating superhydrophilic surfaces from hydrophilic material).[254] We hypothesis that the surfaces become hydrophobic due to air entrapment, resulting in a Cassie-Baxter wetting profile.[255], [256] Another possibility is that the limit between hydrophilic and hydrophobic is not 90° as expected by Young' equations. Berg *et al.* suggested that this limit lies around 65°, based on attraction-repulsion forces of physical chemistry.[123], [257]

The previous results are in agreement with the sliding angles reported above, whereby the creation of micro/nanostructured topographies increases the hydrophobicity of the surface, aiding in the retention of the fluorocarbon lubricant while decreasing droplet pinning. Additionally, coating the surfaces with SAMs of fluorosilane produces an even higher contact angle compared with untreated surfaces, which is expected because fluorocarbon compounds are highly hydrophobic.[258] In summary, these hydrophobic traits produced by the creation of a nanostructured topography and chemical affinity through the fluorosilanization process, both inhibited the aqueous solution from getting pinned, while at the same time retained the hydrophobic lubricant layer. Furthermore, similar observations are highlighted in the following section where droplets containing magnetic particles were manipulated via a patterned permalloy layer on the CLINS.

6.3.3 Magnetic Droplet Manipulation on CLINS

We characterized the developed surfaces by measuring their capacity to reduce the interfacial friction involved in manipulating superparamagnetic droplets using magnetized ferromagnetic structures. We hypothesized that magnetic droplet manipulation would be more efficient with the CLINS compared with untreated surfaces. Moreover, we expected that surfaces displaying low sliding angles would permit longer range droplet manipulation because of reduced friction. This hypothesis was tested by actuating the magnetic droplets at different distances from the tip of the triangular-shaped magnetized permalloy layer and recording at which distances the magnetic field gradients applied sufficient attractive force to slide the superparamagnetic droplets. We characterized the following gold surfaces: bare planar, bare wrinkled, lubricated planar, lubricated wrinkled, silanized lubricated planar, and silanized lubricated wrinkled surfaces. In all cases, a permanent magnet was employed to magnetize the triangular-shaped permalloy structure, and to achieve magnetic actuation of a 1 µL superparamagnetic droplet (2×10^9 mL^{-1}) positioned at different distances (3, 6, and 9 mm) from the tip of the triangular-shaped permalloy (**supplementary videos S1-S3**). Figure 6.2d presents the results of this magnetic droplet manipulation on various gold surfaces. As expected, there was droplet pinning on the surface of both the bare planar and wrinkled surfaces. Lubricated wrinkled surfaces that were not treated with fluorosilane displayed partial slippery characteristics, depicted by attraction of the droplets only from the nearest position (3 mm). This could be explained by the physical entrapment of the lubricant, acting as an intermediate phase between the droplet and the gold micro/nanotextured surface such that by filling the gaps within the wrinkles, the lubricant

promotes sliding of the magnetic droplet toward the magnetized permalloy. Furthermore, due to the lack of chemical affinity, the lubricant only partially adheres to the wrinkled gold surface, exposing features of the wrinkles for the droplet to attach to, resulting in the observed intermediate slippery behavior. Finally, gold-based CLINS provided slippery characteristics by attracting droplets placed 9 mm away from the permalloy tip. The magnetic droplet manipulation results are in line with the sliding angle results shown in Figure 6.2b. These rapidly prototyped gold/permalloy material architectures can be further utilized to design microchips for magnetic droplet manipulation, mixing and separation (**supplementary video S4**).

6.3.4 Electrochemical Characterization of CLINS

The continuity and the resultant conductivity of the wrinkled gold surfaces were verified previously by measuring the sheet resistance of the patterned gold films.[160] In addition, the SEM image presented in **Figure 6.3a-**inset shows the side view of the wrinkled gold structures, which are composed of continuous hills and valleys having micrometer/sub-micrometer length scales. The electrochemical and charge transfer properties of the gold surfaces were assessed to determine their suitability for use in electrochemical applications. Cyclic voltammetry (CV) was used to compare the electrochemical behavior of bare, fluorosilanized, lubricated, and fluorosilanized and lubricated wrinkled gold surfaces (Figure 6.3a). The CV curves obtained from all four classes of electrodes displayed the well-defined redox signature of ruthenium hexamine complex present in the electrolyte solution. However, compared with bare wrinkled surfaces, all of the treated surfaces exhibited lower redox peaks due to the blocking of

electron transfer by fluorosilane SAMs and lubricant layers on the electrode surface. Fluorosilanized wrinkled electrodes exhibited a ~27% decrease in the reduction peak, while the fluorosilanized and lubricated electrode demonstrated a ~41% decrease in the reduction peak compared with the bare gold electrodes. Interestingly, lubricated electrodes, with or without the fluorosilane, displayed almost identical peak current values, indicating comparable accessibility of the surfaces to the solution, and similar charge transfer properties. The well-defined redox peaks after the addition of SAM and lubricant layers suggests that CLINS can be effectively used in electrochemical applications. Effect of scan rate on the peak currents was studied for bare and modified wrinkled electrodes (**Figure S6.1**). For the bare wrinkled electrodes, the reduction peaks vary linearly with square root of scan rate (Figure S6.1a). This linear behavior, however, was not observed in case of treated wrinkled electrodes (Figure S6.1b). In addition, the stability of hydrophobic slippery and electrochemical properties of the wrinkled fluorosilanized/lubricated gold surfaces were examined by measuring the contact and sliding angles before and after 50 CV cycles. **Figure S6.2** demonstrates the shape of the 1^{st}, 10^{th}, 20^{th}, 30^{th}, 40^{th} and 50^{th} CV scans. The 10^{th} CV cycle exhibited a ~24% increase in the reduction peak compared with the first scan. The increase in the reduction peak becomes insignificant after the 10^{th} scan; The 20^{th} and 50^{th} CV scans show a ~29% and ~32% increase in the reduction peak in compared with the first CV. The sliding and contact angles remained intact after the vigorous electrochemical experiments, sliding angles <5 degrees (not shown), contact angles ~150 degrees, displayed in **Figure S6.3**.

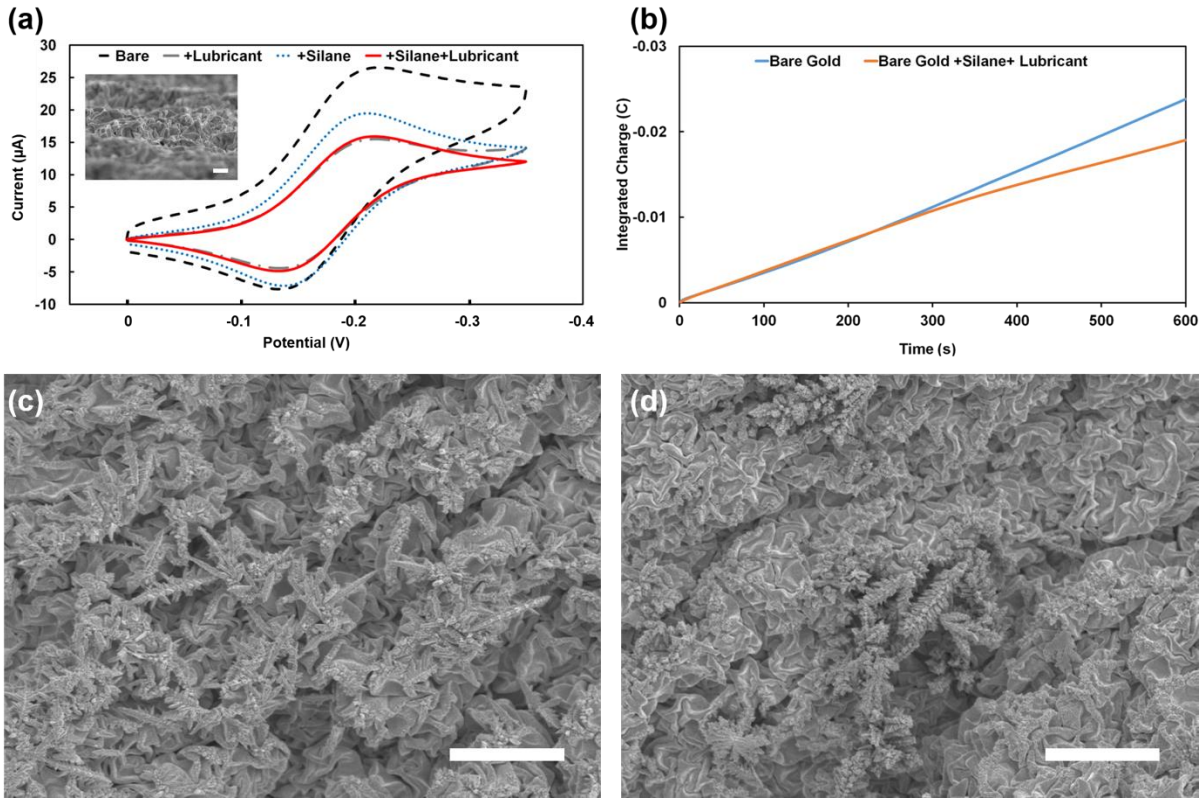

Figure 6.3. Electrochemical characterization of CLINS. (a) A comparison of CVs for four sets of electrodes: bare (black dashed line), fluorosilanized (blue dashed line), lubricated (grey dashed line), and fluorosilanized and lubricated (solid red line) wrinkled gold electrodes, obtained in a solution of 2 mM of ruthenium hexamine and 0.1 M of sodium chloride. The CV scans were run at a scan rate of 100 mV s^{-1}. The inset represents the side-view SEM image of the wrinkled gold structures. The scale represents 1 μm. (b) The integrated charge transferred for 10 minutes of palladium electrodeposition on bare (blue) and fluorosilanized and lubricated (orange) wrinkled gold electrodes. SEM images of the bare (c) and fluorosilanized and lubricated (d) wrinkled gold electrodes (CLINS) following palladium electrodeposition. The scale bars represent 5 μm.

The ability of CLINS to participate in electrochemical reactions that rely on charge transfer between solution-borne species and electrodes was further investigated by electrodepositing palladium micro/nanostructures on the fluorosilanized and lubricated gold wrinkles. Chronoamperometry was used to deposit palladium on the gold wrinkles, and the integrated charge transferred during 10 minutes of electrodeposition was calculated

for both bare and CLINS (Figure 6.3b). It is evident that the amount of integrated charge involved in electrodeposition on CLINS is lower (by about 20 %) compared with bare surfaces, which follows the same trend observed in the CV measurements.

Figures 6.3c and 6.3d show the scanning electron microscopy (SEM) images of the bare surfaces and CLINS after 10 minutes of palladium electrodeposition, respectively. Palladium electrodeposits were seen as fractal structures that extrude from the wrinkled gold surfaces. These structures were observed on both bare and fluorosilanized and lubricated wrinkled films; however, slightly fewer deposits were seen on the treated surfaces. This observation is in line with the results obtained from the CV curves and the integrated charge measured during electrodeposition. These results suggest that CLINS are applicable to electrochemical sensing where the need for anti-fouling and self-cleaning properties is paramount.

6.3.5 Plasma Coagulation Assay

We performed a plasma coagulation assay to assess the capacity of CLINS in preventing protein adsorption and blood clot formation. For this experiment, bare wrinkled, lubricated wrinkled, or fluorosilanized and lubricated wrinkled surfaces were glued to the inner walls of a 96-well plate. The lubricated surfaces were saturated with PFPP for 1 minute, then, the excess lubricant was removed by decanting the lubricant from the wells. The clotting assay was performed by adding the citrated human plasma to the wells containing the gold surfaces and empty wells used as control. Clotting was initiated by the addition of calcium chloride as explained in the methods section and absorbance measurements were performed. As shown in **Figure 6.4**, the bare surfaces elicited the

shortest clotting time of 685 seconds, while clotting times with wrinkled-lubricated and fluorosilanized wrinkled-lubricated surfaces were 887 seconds and 1106 seconds, respectively. In addition, it is evident from the SEM images that compared with the dense protein network formed on bare wrinkled surfaces, there was less protein deposition on lubricated surfaces and little to no protein deposition on CLINS (fluorosilanized and lubricated surfaces, Figure 6.4b-d). It should be noted that clots eventually formed on all surfaces; however, it is worth considering that the CLINS surface area represents less than 8% of the total surface area exposed to the plasma. Therefore, the coagulation of the plasma is likely due to the contact of the plasma with the polystyrene surface of the wells. In summary, CLINS significantly enhances anti-fouling and self-cleaning properties by reducing protein adhesion onto the surface as shown by the increase in coagulation time in the assay and qualitatively by comparing the SEM images.

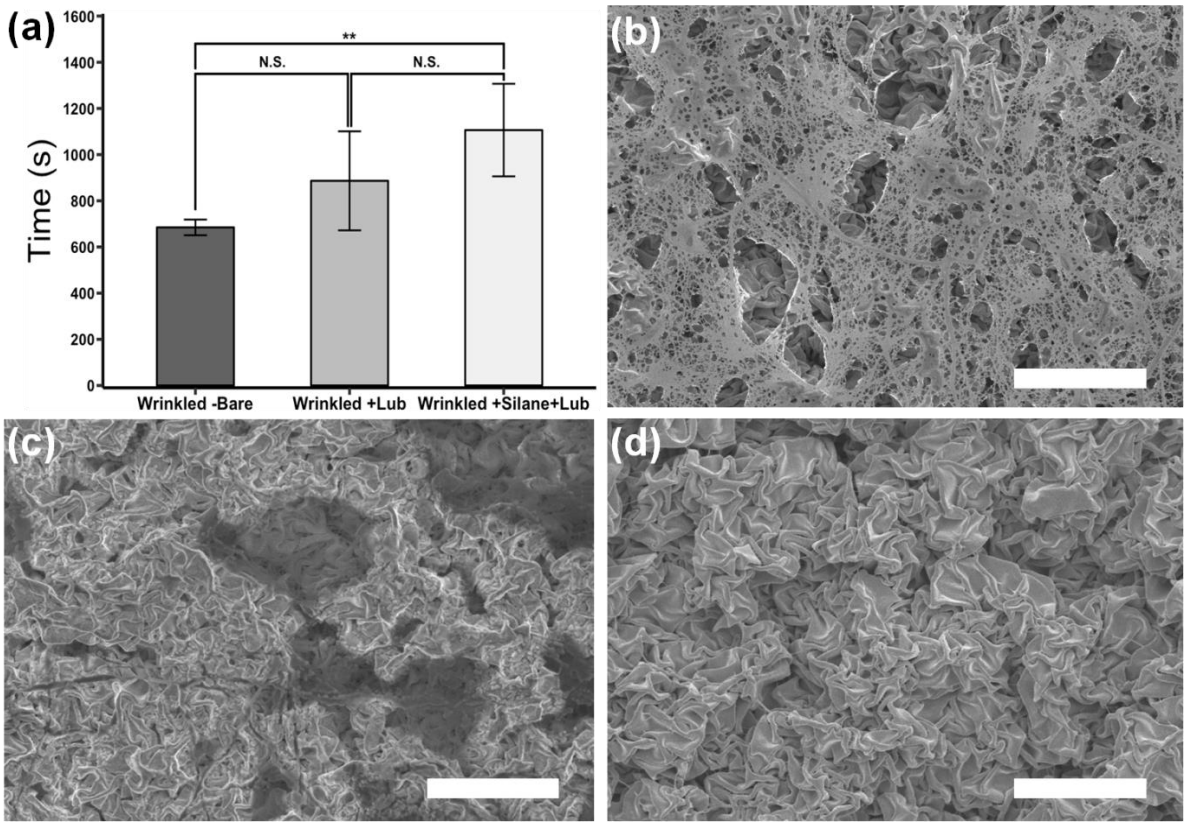

Figure 6.4 The plasma coagulation assay. (a) Mean coagulation time to reach half-max opacity, upon the initiation of the coagulation cascade on: wrinkled surfaces without lubricant, lubricated wrinkled surfaces and fluorosilanized and lubricated wrinkled surfaces (CLINS). (b) SEM image of clot formation on a bare wrinkled gold surface displaying full coverage of the surface with protein networks. (c) SEM image of a wrinkled and lubricated (without fluorosilanization) surface after the coagulation assay, displaying some protein adhesion. (d) SEM image of a CLINS after coagulation assay with no visible signs of protein adhesion and clot formation. All scale bars represent 5 μm.

6.4 Conclusion

In this work, we developed a new class of micro/nanotextured, conductive, and hydrophobic slippery surfaces by combining wrinkled gold electrodes with perfluorinated lubricant-infused coatings. We demonstrated that the slippery properties of these surfaces could be enhanced by introducing an intermediate fluorosilane layer between the gold and

the lubricant. Applying a lubricant layer directly onto the gold electrode resulted in moderately slippery electrodes (sliding angle < 20°), whereas the addition of an intermediate fluorosilane layer decreased sliding angles to < 5°). Both the lubricated-wrinkled and fluorosilanized and lubricated winkled surfaces (CLINS) exhibited reduced interfacial friction experienced by superparamagnetic aqueous droplets manipulated by on-chip magnetized ferromagnetic layers. However, interfacial friction was reduced to a greater extent on CLINS than on lubricated surfaces. Importantly, the hydrophobic slippery gold surfaces were characterized electrochemically to evaluate their utility in applications where charge transfer between the metallic layer and redox species in solution is necessary. First, cyclic voltammetry was used to observe the redox signature of ruthenium hexamine. These experiments demonstrated that while the addition of the fluorosilane layer and/or the lubricant slightly reduced the observed redox peaks, the electrodes were capable of participating in charge transfer while possessing hydrophobic slippery properties. Second, these electrodes were used as substrates for the electrodeposition of palladium. Palladium electrodeposition was possible on the newly developed surfaces; however similar to the first set of electrochemical experiments, the charge transfer on the coated surface was reduced compared with that on the bare wrinkled substrates. Finally, the lubricant-infused wrinkled gold electrodes developed here significantly reduced the adsorption of blood proteins and prolonged the clotting times compared with bare surfaces. The CLINS described in this work are expected to be used in conductive biosensors or other medical devices that operate in complex biological environment.

6.5 Experimental Section

Fabrication of CLINS: Figure 6.1 summarizes the fabrication process. PSPS (Graphix Shrink Film, Graphix, Maple Heights, OH) were cleaned in isopropanol and in a deionized (DI) water bath under orbital agitation for 10 minutes, and then dried by air stream. A thin gold film (20 nm) was sputtered onto the PSPS from a 99.999% purity gold target (LTS Chemical Inc., Chestnut Ridge, NY) using a Torr Compact Research Coater CRC-600 manual planar magnetron sputtering system (New Windsor, NY). The argon (99.999% purity, AlphaGaz, Air Liquide, Montreal, QC) plasma was created using a DC current of 50 A and a deposition rate of 0.9 Å s^{-1} monitored using a quartz crystal sensor. For chemical modification, the samples were first treated with oxygen plasma for 3 minutes on high RF power (18W) to activate the gold surface and enable its reaction with fluorosilane. CVD was then employed to deposit a SAM of Trichloro (1H,1H,2H,2H-perfluorooctyl) silane (TPFS) (Sigma–Aldrich, Oakville, Canada) onto the gold surfaces, and the devices were heated at 60 °C to create covalent bonds between the silane and the gold substrate. Next, in order to generate the wrinkled micro/nanostructured gold surfaces, gold-coated PSPS films were heated at 160 °C for three minutes. After the shrinking process, a biocompatible lubricant (PFD or PFPP) was added to the substrate to create the CLINS.

Electrodeposition of Permalloy: The permalloy electroplating was performed using a CHI660D electrochemical workstation (CH Instrument, Austin, TX) and a standard three-electrode set-up. The electrochemical system consisted of an Ag/AgCl reference electrode, a platinum mesh counter electrode, and the gold coated polystyrene substrate as the working electrode. The permalloy electrodeposition bath solution contained 0.95 M nickel

(II) sulfate hexahydrate, 18 mM iron (II) sulfate heptahydrate, 0.4 M boric acid, 4.87 mM sodium saccharin, and 0.35 mM sodium dodecyl sulfate (Sigma-Aldrich, St. Louis, MO). The permalloy plating was performed at room temperature using chronopotentiometry with a current density of 5 mA cm^{-2} for 44 seconds (~60 nm).[97], [161]–[164]

Surface Characterization: The wrinkled gold surfaces were tested for hydrophobic characteristics and surface chemistry through water contact angles, sliding angles and XPS, respectively. Elemental fraction percentages were measured from the XPS spectra, obtained using a Physical Electronics (PHI) Quantera-II spectrometer. The x-rays were created from an aluminum anode soure and focused onto the surface using a quartz crystal monochromator. The survey spectra were produced with an operating pressure less than 2.0×10^{-8} Torr, a monochromatic Al K-α X-ray (1486.7 eV) source at 50 W using a voltage of 15 kV, and a pass energy of 280 eV. All spectra were obtained using dual beam charge compensation to neutralize the samples and a take-off angle of 45 degrees. Data analysis was performed using PHI MultiPak version 9.4.0.7 software.

Contact angle measurements were performed using an Optical Contact Angle goniometer (Kruss DSA10-Mk2, DSA1 software) using a 2 µL droplet of DI water placed onto the surfaces. Sliding angles were measured by placing the samples onto a digital scale, which measures the angle of inclination. After a 5 µL droplet of DI water was pipetted onto the PFD (Sigma-Aldrich, St. Louis, MO) lubricated surfaces, the platform was slowly raised, and the sliding angle was defined as the angle of inclination where the droplet started to move. A minimum of five substrates were tested per condition. It should be noted that for all experiments requiring a lubricant layer, samples were first impregnated with an

abundant amount of lubricant, followed by tilting the samples 90 degrees to the horizontal plan decanting all excess lubricant not entrapped by physical/chemical forces. The thickness of the remaining lubricant layer on the surfaces was calculated using the measured lubricated area of the substrates and weight and density of the lubricant. The weight of the lubricant layer was determined by subtracting the weight of the bare substrate (no lubricant) from the weight of the lubricated substrate. All the weight measurements were performed using an analytical balance (AL54 Analytical Balance, Mettler Toledo, Mississauga, ON) with a readability of 0.1 mg. The density of the lubricant was provided by the manufacturer specifications (PFD 1.908 g ml^{-1}).

Electrochemical Characterization: CV was performed using a CHI660D electrochemical workstation (CH Instrument, Austin, TX) and a standard three-electrode set-up. The system consisted of a platinum wire as the counter electrode, an Ag/AgCl reference electrode, and the gold coated PS substrates as the working electrodes. Four sets of working electrodes (four test cases), with the same geometric active area (2 × 2 mm^2), were prepared: (*i*) bare wrinkled gold (control), (*ii*) silanized wrinkled gold, (*iii*) lubricated wrinkled gold, and (*iv*) silanized and lubricated wrinkled gold. The electrochemical bath used for CV consisted of 2 mM hexaammineruthenium (III) chloride and 0.1 M sodium chloride (Sigma-Aldrich, St. Louis, MO). The working electrode was immersed in the electrochemical bath along with the counter and reference electrodes, and the CV scans were run at a scan rates of 20, 40, 80, 100, and 160 mV s^{-1}. The working electrodes that require lubrication (test cases iii and iv) were lubricated right before their immersion into the bath solution.

Scanning Electron Microscopy: SEM imaging (JSM- 7000F) was performed in secondary electron image (SEI) mode with voltages of 1.0 kV at 10,000x magnification or 2.0 kV at 1000x magnification. Samples used for plasma coagulation testing, were washed three times, fixed in 4% formaldehyde in PBS for 2 hours, and washed with PBS (0.1 M) prior to imaging.

Electrodeposition of Palladium: A standard three electrode electrochemistry set up was used for the electrodeposition of palladium with platinum as the counter electrode and a Ag/AgCl electrode as the reference electrode. Palladium structures were deposited from a 5 mM hydrogenchloropalladate solution at a potential of -0.2 V (vs. Ag/AgCl reference electrode) for 150 s using a Gamry potentiostat (Gamry Reference 600, Gamry Instruments Inc., Warminster, PA).

Plasma Coagulation Assay: In preparation for the clotting examination, human citrated plasma was thawed and placed in an ice bath. Pooled citrated plasma was generated from blood samples collected from 10 healthy donors as previously described by Yau *et al*.[259] The gold wrinkled surfaces were glued to the inner surface of a 96-well plate, using a medical grade silicon adhesive (Silbione, Bluestar Silicones, Burlington, ON) without obstructing the center of the well. The gold surfaces were impregnated with 150 μl of PFPP lubricants for one minute, followed by the decanting of any excess lubricant and immediately introducing 100 μl of citrated human plasma to cover the surfaces. The well-plate containing the sensors was incubated for five to seven minutes at 37 °C to mimic physiological conditions, then, 100 μl of a pre-warmed 25 mM calcium chloride solution (HEPES 20 mM, pH 7.4 and 1 M) was added to each well to commence the clotting of the

plasma. The clotting time was measured using a SPECTRAmax plate reader (Molecular Devices, San Jose, CA) by measuring absorbance at 405 nm at 10 second intervals. The clotting time was defined as the half-max point obtained from the absorbance *versus* time plots.

Magnetic Microdroplet Manipulation: Magnetic microdroplet actuation was explored on six different gold coated PS surfaces: (i) planar gold, (ii) wrinkled gold, (iii) lubricated planar gold, (iv) lubricated wrinkled gold, (v) silanized lubricated planar gold, and (vi) silanized lubricated wrinkled gold (CLINS). In all the above scenarios, thickness of the sputtered gold was 20 nm before shrinking. In addition, all the surfaces consisted of a triangular-shaped electroplated permalloy with thickness of ~60 nm (before shrinking). The system employs an external NdFeB permanent magnet (Standex-Meder Electronics Inc., Oakville, ON), with a dimension of 5 mm × 10 mm × 3 mm. The magnet was secured using double-sided tape beneath the substrates and aligned with the triangular-shaped permalloy on top of the device, as shown in Figure 6.2(d). For the scenarios where lubricant was required, the surfaces were covered with the lubricant before applying the magnetic droplet. Next, a 1 µl drop of a superparamagnetic aqueous solution with a bead concentration (2.8 µm Dynabead M-270, Invitrogen, Carlsbad, CA) of 2×10^9 ml^{-1} was placed on the gold surface, 3 mm away from the tip of the triangular-shaped permalloy. The movement of the droplets was recorded using a camera. The experiment was repeated by placing the droplet at 6 mm and 9 mm away from the permalloy tip for each test case scenario (total of 18 experiments).

Statistical Analysis: All statistical analyses were performed using the open source software R version 3.3.2 (www.r-project.org). Parametric data was tested with a one-way ANOVA, with additional post-hoc Tukey Honest Significant Difference test from the R package stats version 3.3.2. Non-parametric data was tested with Kruskal-Wallis Rank Sum Test from the R package stats version 3.3.2 followed by a multiple comparison test from R package pgirmess version 1.6.5. Significance levels were defined as significant (*) p-value < 0.05, highly significant (**) at p-value < 0.01 and very significant (***) at p-value < 0.001.

6.6 Supporting Information

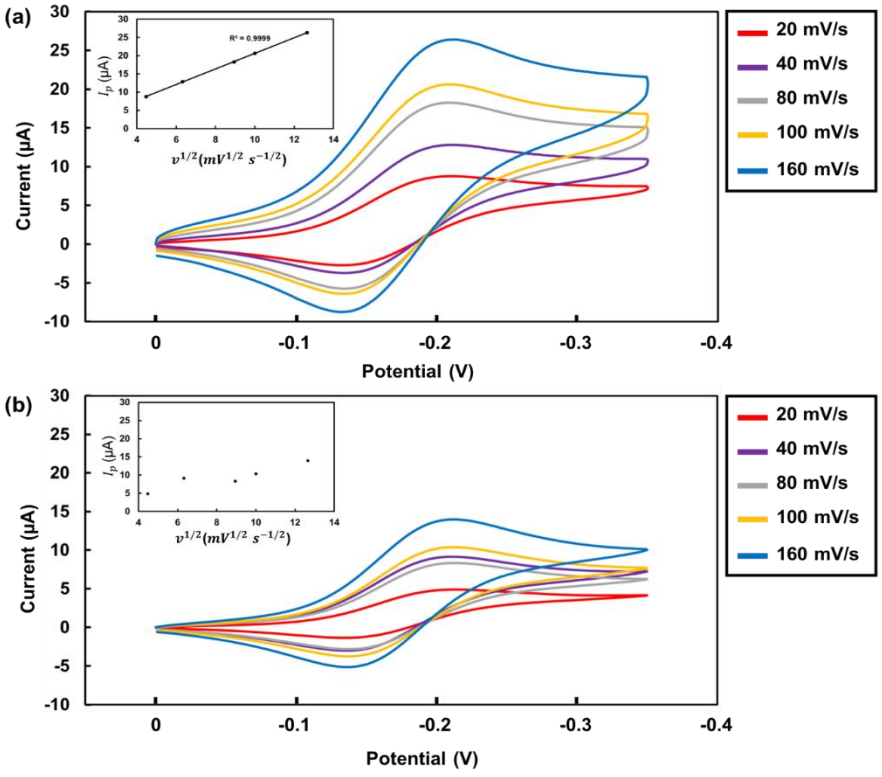

Figure S6.1 Effect of scan rate on the peak currents of the CV scans for (a) bare wrinkled and (b) wrinkled fluorosilanized/lubricated electrodes obtained in a solution of 2 mM of ruthenium hexamine and 0.1 M of sodium chloride. The insets show the plot of reduction current versus square root of scan rate.

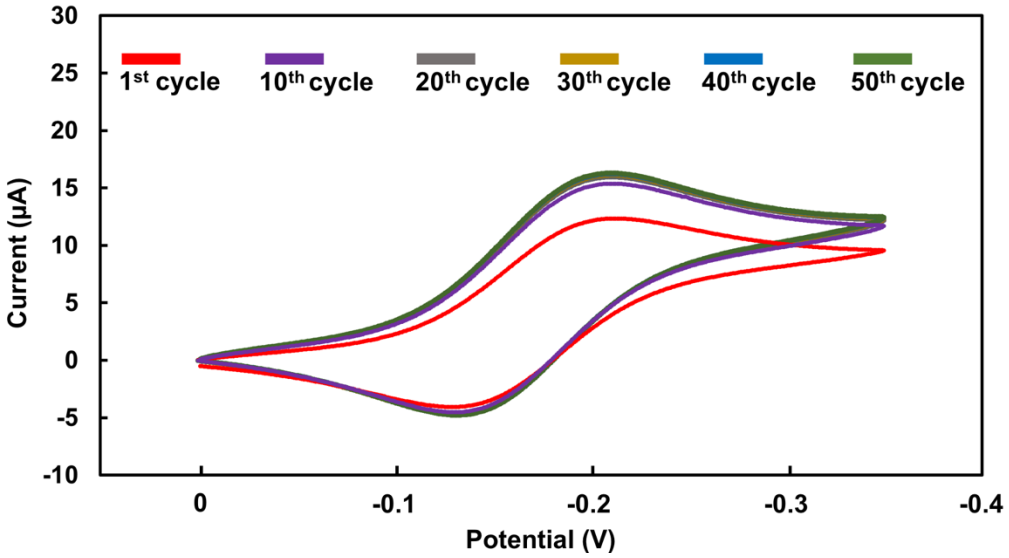

Figure S6.2 The stability of electrochemical properties of CLINS after 50 CV cycles obtained in a solution of 2 mM of ruthenium hexamine and 0.1 M of sodium chloride. The CV scans were run at a scan rate of 100 mV/s.

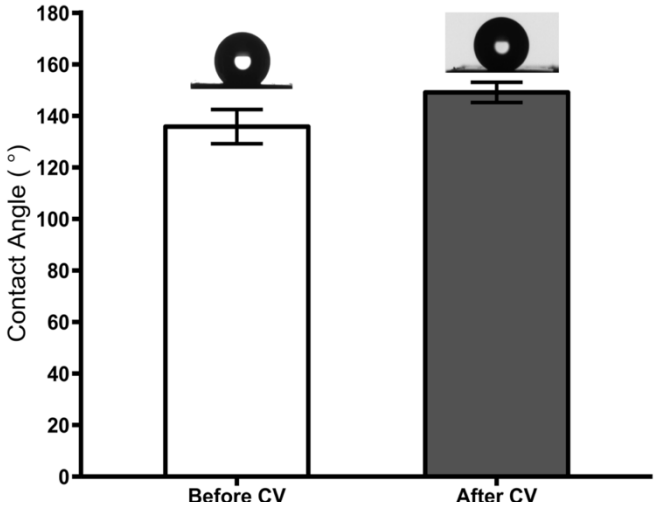

Figure S6.3 The stability of perfluorinated SAM after 50 CV cycles obtained in a solution of 2 mM of ruthenium hexamine and 0.1 M of sodium chloride. Inset displays droplet morphology on the surfaces before and after CV cycles.

6.7 Acknowledgements

The Scanning electron microscopy was carried out at the Canadian Centre for Electron Microscopy (CCEM), a national facility supported by NSERC and McMaster University. The authors would like to thank Danielle Covelli for XPS support at McMaster's BioInterfaces Institute. Additional thanks to Kim Rivera and Emma Rogers for collaboration on the project. TFD acknowledges support from Natural Science and Engineering Research Council of Canada (NSERC) Discovery grant and start-up funds from McMaster University.

Chapter 7 Summary, Conclusions, Limitations, Future Work, and References

In this last chapter, the findings of this thesis work are summarized, and their contribution to the development of microfluidic magnetic bio-separators for integration in LOC systems are discussed. Lastly, the drawbacks of the current discoveries and the anticipated future works that build on these results are discussed.

7.1 Thesis Summary

The main objectives of this work were to design, fabricate, and characterize micro-electromagnetic devices for manipulation of suspended MPs, and to demonstrate their applicability for integration with LOC systems used in POC settings.

The design and optimization of the magnetic devices were conducted through extensive computer modeling. We investigated the effect of the copper micro-coil geometry, dimensions, and surface texturing, in addition to contribution of permalloy thin films and applied currents, on the generated magnetic force. Moreover, the outcome of Joule heating, generated by the micro-electromagnet, on the movement of fluid within a microfluidic channel was studied. The simulated active-passive devices were fabricated on shrinkable polymers using lithography-free and rapid benchtop techniques such as xurography, thermal shrinking, wrinkling, spin coating, and electroplating. The wrinkled copper micro-coil was characterized using SEM, and the thin film electrodeposited permalloy was analyzed using profilometer, EDX, and SQUID. The application of the multi-scale active-passive magnetic device was demonstrated through low current (~30

mA) capturing of different size MPs. Furthermore, we successfully integrated these devices into microfluidic systems for cell separation purposes in a continuous flow.

We have shown that a fully integrated microfluidic magnetic device can be fabricated using rapid and simple benchtop methods in a matter of a few hours. We have also demonstrated that the prototyped device can attract particles from far distances and magnetically trap them. It was realized that the thermal advection caused by Joule heating was responsible for the movement of far particles. Upon successful integration with microfluidic channels, the device can be applied for free-flow capture and release of magnetically tagged cells.

7.2 Thesis Conclusions

1. Multi-scale polymer-based micro-electromagnetic devices can be fabricated using lithography-free benchtop techniques such as xurography, PSPS heat shrinking, metallic thin film wrinkling, spin coating, and electroplating. These devices are ideal for addressing the rapid prototyping needs of industry and academic researchers as they can be fabricated in a matter of hours.
2. By taking advantage of micro/nano-wrinkled structures it is possible to enhance the generated magnetic force while keeping the applied current relatively low (~ 30 mA).
3. Due to active-passive nature of these devices, the electroplated permalloy layers become magnetized by the induced magnetic field using the micro-structured wrinkled copper conductors with an applied current of 30 mA.
4. Through thermal-fluidic computer simulations and experiments, we found that thermal advection caused by Joule heating can guide particles in certain directions if the channel

or reservoir dimensions were designed properly. Poor thermal conductivity of the thick PS substrate also enhances the thermal advection. This was confirmed by additional experiments using silicon substrates with high thermal conductivities. Using the combination of magnetic field gradient and temperature gradient, we can collect suspended MPs that are located tens of microns away from the micro-electromagnet.

5. The benchtop-fabricated active-passive magnetic device can be integrated with microfluidics to selectively capture and release magnetically tagged cells in a continuous flow with an applied current of 30 mA and a flow rate of 1 µl/min. The obtained experimental results indicate that this microfluidic device can be potentially used for separation of rare cells such as CTCs from heterogeneous samples.
6. Using the same rapid prototyping techniques, we developed a new category of conductive, micro/nanotextured, friction-less, and self-cleaning surfaces by combining wrinkled gold structures with perfluorinated lubricant-infused coatings. The intermediate fluorosilane SAM is important for locking in the lubricant on the wrinkled gold surfaces. The sliding angles of the lubricant infused flat and wrinkled surfaces were measured to be $< 20°$ and $< 5°$ respectively. This lubricant infused wrinkled surface can be used as a substrate for an open-channel manipulation of superparamagnetic microdroplets. Moreover, the developed surface can be used as an electrochemical transducer while keeping its hydrophobic slippery properties, even though the addition of the fluorosilane layer and/or the lubricant slightly reduce the amplitude of the electrochemical signal. Finally, the lubricant-infused wrinkled gold electrodes developed here can significantly attenuate the non-specific adhesion of blood

proteins and delay the clotting time compared with untreated surfaces. Therefore, these chemical and physical surface modification techniques can be applied to LOC components such as microfluidics, magnetic separation, and biosensing devices to avoid non-specific adhesion of proteins and cells when dealing with complex biological samples.

7.3 Contribution to the Field

The research described in this thesis led to the following contributions to the field:

The development of benchtop fabricated multi-scale active-passive magnetic devices for capturing magnetic particles at low operational currents:

To best of my knowledge, this work was the first example of a current-controlled micro-electromagnetic device that was fabricated on shrinkable polymers using benchtop techniques such as xurography, thin film wrinkling, spin coating, and electrodeposition. The prototyped microsystem is ideal for addressing the needs for rapid prototyping in industrial or academic settings. These devices are capable of trapping MPs that are suspended tens of microns away from the device capturing sites with a relatively low current of 30 mA; to best of my knowledge, this is the lowest reported current that is capable of capturing MPs. In addition to the active-passive nature of these devices, the micro/nano-wrinkled features of the electromagnet aid to enhance the magnitude and spatial resolution of the magnetic force at such a low applied current.

Manipulation and concentration of MPs using the combination of temperature gradients and magnetic field gradients:

We studied the effect of localized temperature gradients caused by the Joule heating on the movement of suspended microparticles. Towards this goal, we completed full numerical simulations and experiments to evaluate the terminal velocities of magnetic and non-magnetic beads at diverse positions on the fabricated magnetic device. We observed that while the calculated terminal velocities of the MPs located at the vicinity of the magnetic traps (~5 μm) were similar to those foreseen by the computer simulations, the MPs located distant from the magnetic capture sites (~50 μm) were attracted with a terminal velocity that was about two orders of magnitude greater than simulated results. By further experiments with non-magnetic particles, simulation of the thermal-fluidic flow, and tests with thermally conductive substrates, it was concluded that due to poor thermal conductivity of the polymeric substrates, the heat advection generated by the PS-based electromagnet transport suspended MPs towards the magnetic traps, and magnetically capture them. These results clear up the discrepancies that exist between theoretical and experimental thermal velocities.

Capture and release of magnetically tagged cells in a continuous flow:

We successfully integrated the benchtop-fabricated active-passive magnetic device with microfluidics to selectively capture and release magnetically tagged yeasts in a continuous flow with a relatively low current of 30 mA. To best of my knowledge, this is the first rapidly prototyped active-passive device that can selectively trap MPs-Cells complexes, at such a low current with no need for cooling system and release them in a free-flow and automated fashion.

Development of electrochemically active, slippery, and self-cleaning micro/nano-structured surfaces:

We introduced a new class of micro/nanotextured, conductive, frictionless surfaces by integrating wrinkled gold structures with fluorosilanized lubricant-infused coatings. This is the first reported lubricant-infused coating, which can be applied to electrical sensors. The physical and chemical properties of the coated surfaces were verified using XPS, contact and sliding angle measurements, surface-based magnetic droplet manipulation, and electrochemical techniques. In addition, hemocompatibility of the coating was confirmed using human blood plasma.

7.4 Limitations and Future Works

This section addresses some of the challenges and possible future directions of this work in terms of characterization, optimization, integration, and applications of the fabricated microfluidic magnetic devices.

First, we need to benchmark the specifications of the developed integrated system explained in Chapter 5, including the capture efficiency, throughput, and cost of production per device against commercially available systems and those under investigation. To further optimize the device functionalities, we need to improve the throughput and capture efficiency of the device. As it was explained before, the generated magnetic force decays rapidly going from bottom (device surface) to the top of the channel. In addition, increasing the flow rate in a microfluidic channel generates a velocity profile that is maximized in the center of the channel. This means that a large portion of the suspended analytes will be effectively flown through the middle of the channel,[36] which is problematic for low-

current on-chip magnetic separation, since the acting magnetic force is only effective closer to the bottom of the channel, and we may lose a large portion of the target cells/biomolecules at higher flow rates. One way to overcome this issue is to estimate the potential trajectory of the tagged cells through a long channel with a defined cross-section and flow rate, and then, depending on the trajectory results, extend the length of the device by cascading a series of the active-passive devices. By extending the length of the channel, tagged cells that are closer to the magnetic surface will be captured earlier, while the ones that are further away experience downward trajectories and eventually will be captured somewhere downstream; depending on their size, magnetic properties, number of attached MPs, and their linear velocities. One drawback of this approach is that as the number of cascaded micro-electromagnets enlarges, the power consumption of the device increases and thus there will be a need for a bulkier power supply.

Another approach for improving the device efficiency is to manipulate the drag force based on the idea of the velocity valleys presented by Besant *et al.*.[187] By growing tall ferromagnetic micro-barriers within the microfluidic channel, it is possible to locally reduce the linear velocities of magnetically tagged cells. When the current is ON, the ferromagnetic structures become magnetized and magnetically labelled cells, whose linear velocity is reduced, will be captured. One likely limitation of this method is the channel blockage due to non-specific adhesions of unwanted cells or proteins when dealing with more complex samples such as blood.

Optimizing the channel dimensions can enhance the capture efficiency and throughput. Reducing the depth of the channel will force the analytes to flow at vicinity of

the magnetic device. However, since the linear velocity is increased by reducing the height of the channel (keeping the width of the channel unchanged), the magnitude of the magnetic force may not be large enough to immobilize the target cells. To compensate for that we envision to integrate wrinkled permalloy micro/nano-structures into the channel walls to increase the regions of high magnetic field gradient. The fabrication of the permalloy embedded microchannel can be conducted by laser engraving the macro-scaled design of the channel into a PSPS sheet and electroplating a thin film (in nanoscale) permalloy into the channel footprint. By thermal shrinking the PSPS, the length and width of the channel will be reduced while its height increases, and the resultant stress causes the electrodeposited permalloy to wrinkle. The permalloy encapsulated PS channel can be bonded to the active-passive device through surface modification and plasma treatment. Due to shallowness of the channel, we expect the wrinkled permalloy to get magnetized when the bottom active-passive device is ON. Non-specific adhesion can be a potential problem with this approach as well, when passing a heterogeneous physiological sample through the shallow channels. We can apply the same method used in Chapter 6 to create a thin lubricant-infused coating inside the channel, and therefore mitigate non-specific adhesion and delay blood coagulations.

Even though the obtained experimental results in Chapter 5 are preliminary, these devices can be further optimized for separation of rare cells such as CTCs from physiological samples (e.g. blood). One major challenge of working with body fluids is the non-specific adhesion of cells and proteins to the device surface and channel walls. In addition, since most of these physiological fluids are more viscous than water, a higher

magnetic force might be required to capture the magnetically labelled cells. To overcome these issues, we can employ the lubricant-infused coating that was presented in Chapter 6 to reduce the non-specific adhesion and enhance the slipperiness of the magnetic device surfaces.

To fulfill the application of this microfluidic magnetic platform, we need to integrate the device with a rapid and sensitive detection system. Although magnetic separation using magnetic microparticles (MPs) offer higher efficiency and specificity than other techniques such as membrane-based filtration[260] and centrifugation,[261] they suffer from complications associated with resuspension of target cells or biomolecules after separation and potential intrusion with biosensing components.[261]–[263] In contrast, magnetic nanoparticles (MNPs) offer higher surface-to-volume ratio, rapid reaction kinetics and lower blocking effect; particularly important for the optical detection and analysis.[261] Wang *et al.* developed a magnetic multiplex immunoassay for fast, sensitive, and simultaneous detection of three main pathogenic bacteria found in food products. The immunoassay was composed of MNPs for immune-separation and quantum dots (QDs) as fluorescent tags. They were able to magnetically separate the bacteria from the sample, and then resuspended and modified the MNPs-cell complexes with immune-QDs to create the MNPs-cell-QD conjugates for simultaneous detection of three different pathogenic bacteria using fluorescence intensity measurement techniques in < 2 hours.[264] This multiplex immunoassay can potentially be integrated to the on-chip magnetic device presented in this thesis; where capturing, fluorescent labelling, and detection can all be performed on the magnetic traps of the chip to reduce the sample-to-response time, reagents, and sample

volumes.

As it was mentioned before, one merit of the proposed microfluidic magnetic device is its ability to capture and release magnetically tagged cells and biomolecules. Leveraging this property, we can magnetically trap target objects, and then release them towards integrated transducers in an automated and continuous fashion. Wang *et al.* employed MNP-based assays to detect β human chorionic gonadotropin (βhCG) on antibody-coated thin gold film electrodes using the grating-coupled surface plasmon resonance (GC-SPR) technique. It was shown that in comparison with other non-magnetic assays, the MNP-based assays can improve the limit of detection within the picomolar range.[265] The same strategy can be adopted to release the magnetically captured target proteins or cells towards surface-based electrical/electrochemical biosensors using the benchtop-fabricated active-passive device.

7.5 References

[1] P. Abgrall and A. M. Gué, "Lab-on-chip technologies: Making a microfluidic network and coupling it into a complete microsystem - A review," *J. Micromechanics Microengineering*, vol. 17, no. 5, pp. R15–R49, 2007.

[2] A. Manz, H. M. Widmers, and N. Graber, "Miniaturized total chemical analysis systems: A novel concept for chemical sensing," *Sensors Actuators B Chem.*, vol. 1, no. 1–6, pp. 244–248, 1990.

[3] D. J. Harrison *et al.*, "Micromachining a Miniaturized Capillary Electrophoresis-Based Chemical Analysis System on a Chip," *Science (80-.).*, vol. 261, no. 5123, pp. 895–897, 1993.

[4] P. Schena, M., Shalon, D., Davis, R. and Brown, "Quantitative Monitoring of Gene Expression Patterns with a Complementary DNA Microarray," *Science (80-.).*, vol. 270, no. 5235, pp. 467–470, 1995.

[5] W. G. Lee, Y.-G. Kim, B. G. Chung, U. Demirci, and A. Khademhosseini, "Nano/microfluidics for diagnosis of infectious diseases in developing countries,"

Adv Drug Deliv. Rev, vol. 62, no. 4–5, pp. 449–457, 2011.

[6] E. P. Kartalov, J. F. Zhong, A. Scherer, S. R. Quake, C. R. Taylor, and W. F. Anderson, "High-throughput multi-antigen microfluidic fluorescence immunoassays," *Biotechniques*, vol. 40, no. 1, pp. 85–90, 2006.

[7] K. Sato, M. Yamanaka, H. Takahashi, M. Tokeshi, H. Kimura, and T. Kitamori, "Microchip-based immunoassay system with branching multichannels for simultaneous determination of interferon-??," *Electrophoresis*, vol. 23, no. 5, pp. 734–739, 2002.

[8] C. Situma, M. Hashimoto, and S. A. Soper, "Merging microfluidics with microarray-based bioassays," *Biomol. Eng.*, vol. 23, no. 5, pp. 213–231, 2006.

[9] A. P. F. Turner, "Biosensors - Sense and sensitivity," *Science (80-.).*, vol. 290, no. 5495, pp. 1315–1317, 2000.

[10] T. Thorsen, S. J. Maerkl, and S. R. Quake, "Microfluidic Large-Scale Integration," *Science (80-.).*, vol. 298, no. 5593, pp. 580–584, 2002.

[11] D. Thevenot *et al.*, "Electrochemical biosensors : recommended definitions and classification To cite this version : Technical report Electrochemical biosensors : recommended definitions and," *Biosens. Bioelectron.*, vol. 16, pp. 121–131, 2001.

[12] L. Soleymani and F. Li, "Mechanistic Challenges and Advantages of Biosensor Miniaturization into the Nanoscale," *ACS Sensors*, vol. 2, no. 4, pp. 458–467, 2017.

[13] H. Yang, "Enzyme-based ultrasensitive electrochemical biosensors," *Curr. Opin. Chem. Biol.*, vol. 16, no. 3–4, pp. 422–428, 2012.

[14] J. Wang, "SURVEY AND SUMMARY: From DNA biosensors to gene chips," *Nucleic Acids Res.*, vol. 28, no. 16, pp. 3011–3016, 2000.

[15] F. Uslu, S. Ingebrandt, D. Mayer, S. Böcker-Meffert, M. Odenthal, and A. Offenhäusser, "Labelfree fully electronic nucleic acid detection system based on a field-effect transistor device," *Biosens. Bioelectron.*, vol. 19, no. 12, pp. 1723–1731, 2004.

[16] P. A. E. Piunno, U. J. Krull, R. H. E. Hudson, M. J. Damha, and H. Cohen, "Fiber-Optic DNA Sensor for Fluorometric Nucleic Acid Determination," *Anal. Chem.*, vol. 67, no. 15, pp. 2635–2643, 1995.

[17] M. Calleja, M. Nordström, M. Álvarez, J. Tamayo, L. M. Lechuga, and A. Boisen, "Highly sensitive polymer-based cantilever-sensors for DNA detection Ultramicroscopy 105 , 215 (2005), original manuscript," *Ultramicroscopy*, vol. 105, no. 1–4, pp. 215–222, 2005.

[18] Y. Huang, E. L. Mather, J. L. Bell, and M. Madou, "MEMS-based sample

preparation for molecular diagnostics," *Anal. Bioanal. Chem.*, vol. 372, no. 1, pp. 49–65, 2002.

[19] K. Pantel and R. H. Brakenhoff, "Dissecting the metastatic cascade.," *Nat. Rev. Cancer*, vol. 4, no. 6, pp. 448–456, 2004.

[20] B. J. Green, T. S. Safaei, A. Mepham, M. Labib, R. M. Mohamadi, and S. O. Kelley, "Beyond the Capture of Circulating Tumor Cells : Next- Generation Devices and Materials," *Angew. Chemie - Int. Ed.*, vol. 55, no. 4, pp. 1252–1265, 2016.

[21] S. Miltenyi, W. Müller, W. Weichel, and A. Radbruch, "High gradient magnetic cell separation with MACS," *Cytometry*, vol. 11, no. 2, pp. 231–238, 1990.

[22] D. R. Gossett *et al.*, "Label-free cell separation and sorting in microfluidic systems," *Anal. Bioanal. Chem.*, vol. 397, no. 8, pp. 3249–3267, 2010.

[23] J. Kim, M. Johnson, P. Hill, and B. K. Gale, "Microfluidic sample preparation: cell lysis and nucleic acid purification," *Integr. Biol.*, vol. 1, no. 10, pp. 574–586, 2009.

[24] R. K. Saiki *et al.*, "Primer-Directed Enzymatic Amplification of DNA with a Thermostable DNA Polymerase Published by : American Association for the Advancement of Science Stable URL : http://www.jstor.org/stable/1700278 REFERENCES Linked references are available on JSTOR for t," *Science (80-.).*, vol. 239, no. 4839, pp. 487–491, 1988.

[25] S. O. Kelley, C. A. Mirkin, D. R. Walt, R. F. Ismagilov, M. Toner, and E. H. Sargent, "Advancing the speed, sensitivity and accuracy of biomolecular detection using multi-length-scale engineering," *Nat Nanotechnol*, vol. 9, no. 12, pp. 969–980, 2014.

[26] S. C. Terry, J. H. Herman, and J. B. Angell, "A Gas Chromatographic Air Analyzer Fabricated on a Silicon Wafer," *IEEE Trans. Electron Devices*, vol. 26, no. 12, pp. 1880–1886, 1979.

[27] D. W. Inglis, R. Riehn, J. C. Sturm, and R. H. Austin, "Microfluidic high gradient magnetic cell separation," *J. Appl. Phys.*, vol. 99, no. 8, pp. 99–101, 2006.

[28] P.-L. Guo, M. Tang, S.-L. Hong, X. Yu, D.-W. Pang, and Z.-L. Zhang, "Combination of dynamic magnetophoretic separation and stationary magnetic trap for highly sensitive and selective detection of Salmonella typhimurium in complex matrix," *Biosens. Bioelectron.*, vol. 74, pp. 628–636, 2015.

[29] D. Nawarathna *et al.*, "Shrink-induced sorting using integrated nanoscale magnetic traps.," *Appl. Phys. Lett.*, vol. 102, no. 6, p. 63504, Feb. 2013.

[30] S. Kumar *et al.*, "Template-Stripped Multifunctional Wedge and Pyramid Arrays for Magnetic Nanofocusing and Optical Sensing," *ACS Appl. Mater. Interfaces*, vol. 8, no. 14, pp. 9319–9326, 2016.

[31] D. Wei, M. J. a Bailey, P. Andrew, and T. Ryhänen, "Electrochemical biosensors at the nanoscale.," *Lab Chip*, vol. 9, no. 15, pp. 2123–2131, 2009.

[32] E. Bassous, H. H. Taub, and L. Kuhn, "Ink jet printing nozzle arrays etched in silicon," *Appl. Phys. Lett.*, vol. 31, no. 2, pp. 135–137, 1977.

[33] C. T. Lim and Y. Zhang, "Bead-based microfluidic immunoassays: The next generation," *Biosens. Bioelectron.*, vol. 22, no. 7, pp. 1197–1204, 2007.

[34] J. Errington and P. Debenedetti, "Relationship between structural order and the anomalies of liquid water.," *Nature*, vol. 409, no. 6818, pp. 318–321, 2001.

[35] H. A. Stone, A. D. Stroock, and A. Ajdari, "Engineering Flows in Small Devices: Microfluidics Toward a Lab-on-a-Chip," *Annu. Rev. Fluid Mech.*, vol. 36, no. 1, pp. 381–411, 2004.

[36] R. a Vijayendran, K. M. Motsegood, D. J. Beebe, and D. E. Leckband, "Evaluation of a Three-Dimensional Micromixer in a Surface-Based Biosensor," *Langmuir*, vol. 19, no. 5, pp. 1824–1828, 2003.

[37] P. E. Sheehan and L. J. Whitman, "Detection Limits for Nanoscale Biosensors," *Nano Lett.*, vol. 5, no. 4, pp. 803–807, 2005.

[38] K. J. Freedman, L. M. Otto, A. P. Ivanov, A. Barik, S. H. Oh, and J. B. Edel, "Nanopore sensing at ultra-low concentrations using single-molecule dielectrophoretic trapping," *Nat. Commun.*, vol. 7, p. 10217, 2016.

[39] J. Dai, T. Ito, L. Sun, and R. M. Crooks, "Electrokinetic Trapping and Concentration Enrichment of DNA in a Microfluidic Channel," *J. Am. Chem. Soc.*, vol. 125, no. 43, pp. 13026–13027, 2003.

[40] K. Liao and C. Chou, "Nanoscale Molecular Traps and Dams for Ultrafast Protein Enrichment in High-Conductivity Bu ff ers," *J. Am. Chem. Soc.*, vol. 134, pp. 8742–8745, 2012.

[41] N. Swami, C. F. Chou, V. Ramamurthy, and V. Chaurey, "Enhancing DNA hybridization kinetics through constriction-based dielectrophoresis," *Lab Chip*, vol. 9, no. 22, pp. 3212–3220, 2009.

[42] P. Augustsson, C. Magnusson, M. Nordin, H. Lilja, and T. Laurell, "Microfluidic, Label-Free Enrichment of Prostate Cancer Cells in Blood Based on Acoustophoresis," *Anal Chem.*, vol. 84, no. 18, pp. 7954–7962, 2012.

[43] M. a M. Gijs, F. Lacharme, and U. Lehmann, "Microfluidic applications of magnetic particles for biological analysis and catalysis.," *Chem. Rev.*, vol. 110, no. 3, pp. 1518–1563, Mar. 2010.

[44] M. K. Sun, G. J. Sommer, M. A. Burns, and E. F. Hasselbrink, "Low-power concentration and separation using temperature gradient focusing via Joule

heating," *Anal. Chem.*, vol. 78, no. 23, pp. 8028–8035, 2006.

[45] B. Wang and X. Cheng, "Enhancement of binding kinetics on affinity substrates by laser point heating induced transport," *Analyst*, vol. 141, no. 5, pp. 1807–1813, 2016.

[46] B. S. Gallardo *et al.*, "Electrochemical principles of active control of liquids on submillimeter scales," *Science (80-.).*, vol. 283, no. 5398, pp. 57–60, 1999.

[47] L. H. Thamdrup, N. B. Larsen, and A. Kristensen, "Light-induced local heating for thermophoretic manipulation of DNA in polymer micro- And nanochannels," *Nano Lett.*, vol. 10, no. 3, pp. 826–832, 2010.

[48] H. C. Feldman, M. Sigurdson, and C. D. Meinhart, "AC electrothermal enhancement of heterogeneous assays in microfluidics.," *Lab Chip*, vol. 7, no. 11, pp. 1553–1559, 2007.

[49] A. Sandhu, H. Handa, and M. Abe, "Synthesis and applications of magnetic nanoparticles for biorecognition and point of care medical diagnostics," *Nanotechnology*, vol. 21, no. 44, pp. 442001–442022, 2010.

[50] J. Dobson, "Magnetic Nanoparticles for Drug Delivery," *Drug Dev. Res.*, vol. 67, no. 1, pp. 55–60, 2006.

[51] R. Di Corato *et al.*, "Magnetic-fluorescent colloidal nanobeads: Preparation and exploitation in cell separation experiments," *Macromol. Biosci.*, vol. 9, no. 10, pp. 952–958, 2009.

[52] S. J. Huang LR, Cox EC, Austin RH, "Continuous Particle Separation Through Deterministic Lateral Displacement," *Science (80-.).*, vol. 304, no. 5673, pp. 987–990, 2004.

[53] B. S. Cho, T. G. Schuster, X. Zhu, D. Chang, G. D. Smith, and S. Takayama, "Passively driven integrated microfluidic system for separation of motile sperm," *Anal. Chem.*, vol. 75, no. 7, pp. 1671–1675, 2003.

[54] H. Lu, S. Gaudet, M. A. Schmidt, and K. F. Jensen, "A microfabricated device for subcellular organelle sorting," *Anal. Chem.*, vol. 76, no. 19, pp. 5705–5712, 2004.

[55] T. P. Hunt, H. Lee, and R. M. Westervelt, "Addressable micropost array for the dielectrophoretic manipulation of particles in fluid," *Appl. Phys. Lett.*, vol. 85, no. 26, pp. 6421–6423, 2004.

[56] M. M. Wang *et al.*, "Microfluidic sorting of mammalian cells by optical force switching," *Nat. Biotechnol.*, vol. 23, no. 1, pp. 83–87, 2005.

[57] S. Nagrath *et al.*, "Isolation of rare circulating tumour cells in cancer patients by microchip technology.," *Nature*, vol. 450, no. 7173, pp. 1235–9, 2007.

[58] J. S. Wang, K. Liu, J. Liu, Z. T. Yu, X. Xu, L. Zhao, T. Lee, E. K. Lee, J. Reiss, Y.

K. Lee, L. W. Chung and H. R. T. Huang, M. Rettig, D. Seligson, K. N. Duraiswamy, C. K. Shen, "Highly Efficient Capture of Circulating Tumor Cells Using Nanostructured Silicon Substrates with Integrated Chaotic Micromixers," *Angew. Chem. Int. Ed.*, vol. 50, no. 13, pp. 3084–3088, 2011.

[59] S. Wang *et al.*, "Three-Dimensional Nanostructured Substrates toward Efficient Capture of Circulating Tumor Cells," *Angew Chem Int Ed*, vol. 48, no. 47, pp. 8970–8973, 2009.

[60] M. Lin *et al.*, "Nanostructure embedded microchips for detection, isolation, and characterization of circulating tumor cells," *Acc. Chem. Res.*, vol. 47, no. 10, pp. 2941–2950, 2014.

[61] J. Sekine, S. C. Luo, S. Wang, B. Zhu, H. R. Tseng, and H. H. Yu, "Functionalized conducting polymer nanodots for enhanced cell capturing: The synergistic effect of capture agents and nanostructures," *Adv. Mater.*, vol. 23, no. 41, pp. 4788–4792, 2011.

[62] N. Zhang *et al.*, "Electrospun TiO2 Nanofiber-Based Cell Capture Assay for Detecting Circulating Tumor Cells from Colorectal and Gastric Cancer Patients," *Adv. Mater.*, vol. 24, no. 20, pp. 2756–2760, 2012.

[63] S. Hou *et al.*, "Polymer Nanofiber-Embedded Microchips for Detection, Isolation, and Molecular Analysis of Single Circulating Melanoma Cells," *Angew Chem Int Ed*, vol. 52, no. 12, p. 3379, 2013.

[64] J. Wen, L. A. Legendre, J. M. Bienvenue, and J. P. Landers, "Purification of nucleic acids in microfluidic devices," *Anal. Chem.*, vol. 80, no. 17, pp. 6472–6479, 2008.

[65] H. Tian, A. F. R. Hühmer, and J. P. Landers, "Evaluation of silica resins for direct and efficient extraction of dna from complex biological matrices in a miniaturized format," *Anal. Biochem.*, vol. 283, no. 2, pp. 175–191, 2000.

[66] N. C. Cady, S. Stelick, and C. A. Batt, "Nucleic acid purification using microfabricated silicon structures," *Biosens. Bioelectron.*, vol. 19, no. 1, pp. 59–66, 2003.

[67] N. C. Cady, S. Stelick, M. V. Kunnavakkam, and C. A. Batt, "Real-time PCR detection of Listeria monocytogenes using an integrated microfluidics platform," *Sensors Actuators, B Chem.*, vol. 107, no. 1, pp. 332–341, 2005.

[68] X. Chen, D. Cui, C. Liu, H. Li, and J. Chen, "Continuous flow microfluidic device for cell separation, cell lysis and DNA purification," *Anal. Chim. Acta*, vol. 584, no. 2, pp. 237–243, 2007.

[69] S. H. Seal, "A sieve for the isolation of cancer cells and other large cells from the blood," *Cancer*, vol. 17, no. 5, pp. 637–642, 1964.

[70] O. Lara, X. Tong, M. Zborowski, and J. J. Chalmers, “Enrichment of rare cancer cells through depletion of normal cells using density and flow-through, immunomagnetic cell separation.,” *Exp. Hematol.*, vol. 32, no. 10, pp. 891–904, 2004.

[71] G. Vona *et al.*, “Isolation by Size of Epithelial Tumor Cells,” *Am. J. Pathol.*, vol. 156, no. 1, pp. 57–63, 2000.

[72] S. Zheng *et al.*, “Membrane microfilter device for selective capture, electrolysis and genomic analysis of human circulating tumor cells.,” *J. Chromatogr. A*, vol. 1162, no. 2, pp. 154–61, 2007.

[73] H. J. Lee *et al.*, “Efficient isolation and accurate in situ analysis of circulating tumor cells using detachable beads and a high-pore-density filter,” *Angew. Chemie - Int. Ed.*, vol. 52, no. 32, pp. 8337–8340, 2013.

[74] J. S. Kuo *et al.*, “Deformability considerations in filtration of biological cells.,” *Lab Chip*, vol. 10, no. 7, pp. 837–842, 2010.

[75] M. G. Elgort, M. G. Herrmann, M. Erali, J. D. Durtschi, K. V. Voelkerding, and R. E. Smith, “Extraction and Amplification of Genomic DNA from Human Blood on Nanoporous Aluminum Oxide Mem- branes,” *Clin. Chem.*, vol. 50, no. 10, pp. 1817–1819, 2004.

[76] J. Kim, K. V. Voelkerding, and B. K. Gale, “Patterning of a nanoporous membrane for multi-sample DNA extraction,” *J. Micromechanics Microengineering*, vol. 16, no. 1, pp. 33–39, 2006.

[77] J. Kim and B. K. Gale, “Quantitative and qualitative analysis of a microfluidic DNA extraction system using a nanoporous AlOx membrane,” *Lab Chip*, vol. 8, no. 9, pp. 1516–1523, 2008.

[78] N. Pamme, “Continuous flow separations in microfluidic devices,” *Lab Chip*, vol. 7, no. 12, pp. 1644–1659, 2007.

[79] M. Yamada, M. Nakashima, and M. Seki, “Pinched flow fractionation: Continuous size separation of particles utilizing a laminar flow profile in a pinched microchannel,” *Anal. Chem.*, vol. 76, no. 18, pp. 5465–5471, 2004.

[80] M. E. brahim. Warkiani *et al.*, “Ultra-fast, label-free isolation of circulating tumor cells from blood using spiral microfluidics,” *Nat. Protoc.*, vol. 11, no. 1, pp. 134–148, 2016.

[81] I. C. Lee, J. F. Chang, and R. S. Juang, “Recent advances and perspectives on capture and concentration of label-free rare cells for biomedical science and engineering research,” *J. Taiwan Inst. Chem. Eng.*, vol. 85, no. 1, pp. 40–55, 2018.

[82] H. Mohamed, M. Murray, J. N. Turner, and M. Caggana, “Isolation of tumor cells using size and deformation,” *J. Chromatogr. A*, vol. 1216, no. 47, pp. 8289–8295,

2009.

[83] J. S. Kuo *et al.*, "Deformability considerations in filtration of biological cells," *Lab Chip*, vol. 10, no. 7, pp. 837–842, 2010.

[84] F. Shen, H. Hwang, Y. K. Hahn, and J. Park, "Label-Free Cell Separation Using a Tunable Magnetophoretic Repulsion Force.pdf," *Anal. Chem.*, vol. 84, no. 7, pp. 3075–3081, 2012.

[85] J. Dykes, A. Lenshof, I. B. Åstrand-Grundström, T. Laurell, and S. Scheding, "Efficient removal of platelets from peripheral blood progenitor cell products using a novel micro-chip based acoustophoretic platform," *PLoS One*, vol. 6, no. 8, p. e23074, 2011.

[86] A. H. J. Yang and H. T. Soh, "Acoustophoretic Sorting of Viable Mammalian Cells in a Microfluidic Device," *Anal Chem.*, vol. 84, no. 24, pp. 10756–10762, 2012.

[87] L. R. Huang, J. O. Tegenfeld, J. J. Kraeft, J. C. Sturm, R. H. Austin, and E. C. Cox, "A dna prism for high-speed continuous fractionation of large dna molecules," *Nat. Biotechnol.*, vol. 20, no. 10, pp. 1048–1051, 2002.

[88] P. R. C. Gascoyne and S. Shim, "Isolation of circulating tumor cells by dielectrophoresis," *Cancers (Basel).*, vol. 6, no. 1, pp. 545–579, 2014.

[89] M. S. Talary, K. I. Mills, T. Hoy, A. K. Burnett, and R. Pethig, "Dielectrophoretic separation and enrichment of CD34+cell subpopulation from bone marrow and peripheral blood stem cells," *Med. Biol. Eng. Comput.*, vol. 33, no. 2, pp. 235–237, 1995.

[90] H.-S. Moon *et al.*, "Continuous separation of breast cancer cells from blood samples using multi-orifice flow fractionation (MOFF) and dielectrophoresis (DEP).," *Lab Chip*, vol. 11, no. 6, pp. 1118–1125, 2011.

[91] F. F. B. P. R. Gascoyne, J. Noshari, T. J. Anderson, "Isolation of Rare Cells from Cell Mixtures by Dielectrophoresis," *Electrophoresis*, vol. 30, no. 8, pp. 1388–1398, 2009.

[92] T.-K. Chiu *et al.*, "Application of optically-induced-dielectrophoresis in microfluidic system for purification of circulating tumour cells for gene expression analysis- Cancer cell line model," *Sci. Rep.*, vol. 6, no. 1, p. 32851, 2016.

[93] N. Pamme, "On-chip bioanalysis with magnetic particles.," *Curr. Opin. Chem. Biol.*, vol. 16, no. 3–4, pp. 436–43, Aug. 2012.

[94] M. Hejazian, W. Li, and N.-T. Nguyen, "Lab on a chip for continuous-flow magnetic cell separation," *Lab Chip*, vol. 15, no. 4, pp. 959–970, 2015.

[95] Q. a Pankhurst, J. Connolly, S. K. Jones, and J. Dobson, "Applications of magnetic

nanoparticles in biomedicine," *J. Phys. D. Appl. Phys.*, vol. 36, no. 13, pp. R167–R181, Jul. 2003.

[96] L. Coudron, I. D. Johnston, C. K. L. Tan, and M. C. Tracey, "Low-cost credit card-based microfluidic devices for magnetic bead immobilisation," *Microfluid. Nanofluidics*, vol. 14, no. 1–2, pp. 359–369, Sep. 2012.

[97] A. Hosseini and L. Soleymani, "Benchtop fabrication of multi-scale micro-electromagnets for capturing magnetic particles," *Appl. Phys. Lett.*, vol. 105, no. 7, p. 074102, Aug. 2014.

[98] D. W. Inglis, R. Riehn, R. H. Austin, and J. C. Sturm, "Continuous microfluidic immunomagnetic cell separation," *Appl. Phys. Lett.*, vol. 85, no. 21, pp. 5093–5095, 2004.

[99] P. Chen, Y.-Y. Huang, K. Hoshino, and X. Zhang, "Multiscale immunomagnetic enrichment of circulating tumor cells: from tubes to microchips.," *Lab Chip*, vol. 14, no. 3, pp. 446–458, 2014.

[100] Q. Cao, X. Han, and L. Li, "Configurations and control of magnetic fields for manipulating magnetic particles in microfluidic applications: magnet systems and manipulation mechanisms," *Lab Chip*, vol. 14, no. 15, pp. 2762–2777, 2014.

[101] R.-J. Yang, H.-H. Hou, Y.-N. Wang, and L.-M. Fu, "Micro-magnetofluidics in microfluidic systems: A review," *Sensors Actuators B Chem.*, vol. 224, pp. 1–15, 2016.

[102] D. Niarchos, "Magnetic MEMS: key issues and some applications," *Sensors Actuators A Phys.*, vol. 109, no. 2, pp. 166–173, 2003.

[103] Q. Ramadan, V. Samper, D. P. Poenar, and C. Yu, "An integrated microfluidic platform for magnetic microbeads separation and confinement," *Biosens. Bioelectron.*, vol. 21, no. 9, pp. 1693–1702, 2006.

[104] N. Xia *et al.*, "Combined microfluidic-micromagnetic separation of living cells in continuous flow," *Biomed. Microdevices*, vol. 8, no. 4, pp. 299–308, 2006.

[105] J. R. Basore and L. A. Baker, "Applications of microelectromagnetic traps," *Anal. Bioanal. Chem.*, vol. 403, no. 8, pp. 2077–2088, 2012.

[106] S. Dubus, J.-F. Gravel, B. Le Drogoff, P. Nobert, T. Veres, and D. Boudreau, "PCR-Free DNA Detection Using a Magnetic Bead-Supported Polymeric Transducer and Microelectromagnetic Traps Se," *Anal. Chem.*, vol. 78, no. 13, pp. 4457–4464, 2006.

[107] H. Lee, a. M. Purdon, and R. M. Westervelt, "Manipulation of biological cells using a microelectromagnet matrix," *Appl. Phys. Lett.*, vol. 85, no. 6, p. 1063, 2004.

[108] C. S. Lee, H. Lee, and R. M. Westervelt, "Microelectromagnets for the control of magnetic nanoparticles," *Appl. Phys. Lett.*, vol. 79, no. 20, pp. 3308–3310, 2001.

[109] Q. Ramadan, D. P. Poenar, and C. Yu, "Customized trapping of magnetic particles," *Microfluid. Nanofluidics*, vol. 6, no. 1, pp. 53–62, 2009.

[110] Q. Ramadan, V. Samper, D. Poenar, and C. Yu, "On-chip micro-electromagnets for magnetic-based bio-molecules separation," *J. Magn. Magn. Mater.*, vol. 281, no. 2–3, pp. 150–172, Oct. 2004.

[111] C. J. Liu, K. Y. Lien, C. Y. Weng, J. W. Shin, T. Y. Chang, and G. Bin Lee, "Magnetic-bead-based microfluidic system for ribonucleic acid extraction and reverse transcription processes," *Biomed. Microdevices*, vol. 11, no. 2, pp. 339–350, 2009.

[112] R. Fulcrand *et al.*, "On chip magnetic actuator for batch-mode dynamic manipulation of magnetic particles in compact lab-on-chip," *Sensors Actuators, B Chem.*, vol. 160, no. 1, pp. 1520–1528, 2011.

[113] J. R. Basore, N. V. Lavrik, and L. A. Baker, "Electromagnetic micropores: Fabrication and operation," *Langmuir*, vol. 26, no. 24, pp. 19239–19244, 2010.

[114] C. P. Gooneratne, C. Liang, and J. Kosel, "A planar conducting microstructure to guide and confine magnetic beads to a sensing zone," *Microelectron. Eng.*, vol. 88, no. 8, pp. 1757–1760, 2011.

[115] J. Choi, C. H. Ahn, S. Bhansali, and H. T. Henderson, "A new magnetic bead-based, filterless bio-separator with planar electromagnet surfaces for integrated bio-detection systems," *Sensors and Actuators*, vol. 68, pp. 34–39, 2000.

[116] J. W. Choi, T. M. Liakopoulos, and C. H. Ahn, "An on-chip magnetic bead separator using spiral electromagnets with semi-encapsulated permalloy," *Biosens. Bioelectron.*, vol. 16, no. 6, pp. 409–416, 2001.

[117] S. H. Song, B. S. Kwak, J. S. Park, W. Kim, and H. IL Jung, "Novel application of Joule heating to maintain biocompatible temperatures in a fully integrated electromagnetic cell sorting system," *Sensors Actuators, A Phys.*, vol. 151, no. 1, pp. 64–70, 2009.

[118] P. WEISS, "The little engines that couldn't: Tired of grinding their gears, micromachine researchers turn to surface science," *Sci. News*, vol. 158, no. 4, p. 56, 2000.

[119] J. Xie, C. Xu, N. Kohler, Y. Hou, and S. Sun, "Controlled PEGylation of Monodisperse Fe 3 O 4 Nanoparticles for Reduced Non-Specific Uptake by Macrophage Cells**," *Adv. Mater.*, vol. 19, no. 20, pp. 3163–3166, 2007.

[120] T. F. Didar *et al.*, "Improved treatment of systemic blood infections using antibiotics with extracorporeal opsonin hemoadsorption," *Biomaterials*, vol. 67,

pp. 382–392, 2015.

[121] T.-S. Wong *et al.*, "Bioinspired self-repairing slippery surfaces with pressure-stable omniphobicity.," *Nature*, vol. 477, no. 7365, pp. 443–7, 2011.

[122] D. C. Leslie *et al.*, "A bioinspired omniphobic surface coating on medical devices prevents thrombosis and biofouling.," *Nat. Biotechnol.*, vol. 32, no. 11, pp. 1134–40, 2014.

[123] S. Wang, K. Liu, X. Yao, and L. Jiang, "Bioinspired Surfaces with Superwettability: New Insight on Theory, Design, and Applications," *Chem. Rev.*, vol. 115, no. 16, pp. 8230–8293, Aug. 2015.

[124] Y. Lu, S. Sathasivam, J. Song, C. R. Crick, C. J. Carmalt, and I. P. Parkin, "Robust self-cleaning surfaces that function when exposed to either air or oil," *Science (80-.).*, vol. 347, no. 6226, 2015.

[125] J. T. Luo, N. R. Geraldi, J. H. Guan, G. McHale, G. G. Wells, and Y. Q. Fu, "Slippery Liquid-Infused Porous Surfaces and Droplet Transportation by Surface Acoustic Waves," *Phys. Rev. Appl.*, vol. 7, no. 1, 2017.

[126] Y. Tuo, H. Zhang, W. Chen, and X. Liu, "Corrosion protection application of slippery liquid-infused porous surface based on aluminum foil," *Appl. Surf. Sci.*, vol. 423, pp. 365–374, 2017.

[127] P. Irajizad, M. Hasnain, N. Farokhnia, S. M. Sajadi, and H. Ghasemi, "Magnetic slippery extreme icephobic surfaces," *Nat. Commun.*, vol. 7, no. 1, p. 133951, 2016.

[128] D. Zhao *et al.*, "Fouling-resistant behavior of liquid-infused porous slippery surfaces," *Chinese J. Polym. Sci. (English Ed.*, vol. 35, no. 7, pp. 887–896, 2017.

[129] D. Mark, S. Haeberle, G. Roth, F. Von Stetten, and R. Zengerle, "Microfluidic lab-on-a-chip platforms: Requirements, characteristics and applications," *Chem. Soc. Rev.*, vol. 39, no. 3, pp. 1153–1182, 2010.

[130] L. M. Rossi, N. J. S. Costa, F. P. Silva, and R. Wojcieszak, "Magnetic nanomaterials in catalysis: Advanced catalysts for magnetic separation and beyond," *Green Chem.*, vol. 16, no. 6, pp. 2906–2933, 2014.

[131] N. Pamme, "Magnetism and microfluidics.," *Lab Chip*, vol. 6, no. 1, pp. 24–38, Jan. 2006.

[132] A.-L. Gassner *et al.*, "Magnetic forces produced by rectangular permanent magnets in static microsystems.," *Lab Chip*, vol. 9, no. 16, pp. 2356–2363, 2009.

[133] L. E. Smart and E. A. Moore, *SOLID STATE CHEMISTRY: An Introduction*. 2005.

[134] N. Nguyen, "Micro magnetofluidics – interactions between magnetism and fluid flow on the microscale," *Microfluid. Nanofluidics*, vol. 12, no. 1–4, pp. 1–16,

2012.

[135] W. F. Brown, “Thermal fluctuations of a single-domain particle,” *Phys. Rev.*, vol. 130, no. 5, pp. 1677–1686, 1963.

[136] A.-H. Lu, E. L. Salabas, and F. Schüth, “Magnetic nanoparticles: synthesis, protection, functionalization, and application.,” *Angew. Chem. Int. Ed. Engl.*, vol. 46, no. 8, pp. 1222–44, Jan. 2007.

[137] S. S. Guo, C. C. Zuo, W. H. Huang, C. Peroz, and Y. Chen, “Response of super-paramagnetic beads in microfluidic devices with integrated magnetic micro-columns,” *Microelectron. Eng.*, vol. 83, no. 4–9, pp. 1655–1659, 2006.

[138] T. Jamshaid *et al.*, “Magnetic particles: From preparation to lab-on-a-chip, biosensors, microsystems and microfluidics applications,” *Trends Anal. Chem.*, vol. 79, no. 1, pp. 344–362, 2016.

[139] P. Li, D. Kilinc, Y.-F. Ran, and G. U. Lee, “Flow enhanced non-linear magnetophoretic separation of beads based on magnetic susceptibility.,” *Lab Chip*, vol. 13, no. 22, pp. 4400–8, Nov. 2013.

[140] G. Fonnum, C. Johansson, A. Molteberg, S. Mørup, and E. Aksnes, “Characterisation of Dynabeads®by magnetization measurements and Mössbauer spectroscopy,” *J. Magn. Magn. Mater.*, vol. 293, no. 1, pp. 41–47, 2005.

[141] R. J. S. Derks, A. Dietzel, R. Wimberger-Friedl, and M. W. J. Prins, “Magnetic bead manipulation in a sub-microliter fluid volume applicable for biosensing,” *Microfluid. Nanofluidics*, vol. 3, no. 2, pp. 141–149, 2007.

[142] S. S. Shevkoplyas, A. C. Siegel, R. M. Westervelt, M. G. Prentiss, and G. M. Whitesides, “The force acting on a superparamagnetic bead due to an applied magnetic field.,” *Lab Chip*, vol. 7, no. 10, pp. 1294–302, Oct. 2007.

[143] J. Berthier and P. Silberzan, *Microfluidics for Biotechnology*. 2010.

[144] J. Castillo, W. E. Svendsen, and M. Dimaki, *Micro and Nano Techniques for the Handling of Biological Samples*. 2011.

[145] R. Wirix-Speetjens, W. Fyen, K. Xu, J. De Boeck, and G. Borghs, “A force study of on-chip magnetic particle transport based on tapered conductors,” *IEEE Trans. Magn.*, vol. 41, no. 10, pp. 4128–4133, 2005.

[146] N. Pamme and A. Manz, “On-chip free-flow magnetophoresis: Continuous flow separation of magnetic particles and agglomerates,” *Anal. Chem.*, vol. 76, no. 24, pp. 7250–7256, 2004.

[147] Y. Chen *et al.*, “Rare cell isolation and analysis in microfluidics,” *Lab Chip*, vol. 14, no. 4, pp. 626–645, 2014.

[148] E. P. Furlani, “Analysis of particle transport in a magnetophoretic microsystem,” *J.*

Appl. Phys., vol. 99, no. 2, p. 024912, 2006.

[149] J. S. Park, S. H. Song, and H. Il Jung, "Continuous focusing of microparticles using inertial lift force and vorticity via multi-orifice microfluidic channels," *Lab Chip*, vol. 9, no. 7, pp. 939–948, 2009.

[150] B. Yellen, G. Friedman, and A. Feinerman, "Analysis of interactions for magnetic particles assembling on magnetic templates," *J. Appl. Phys.*, vol. 91, no. 10, p. 8552, 2002.

[151] E. Katz and I. Willner, "Integrated nanoparticle-biomolecule hybrid systems: synthesis, properties, and applications.," *Angew. Chem. Int. Ed. Engl.*, vol. 43, no. 45, pp. 6042–6108, Nov. 2004.

[152] J.-M. Nam, S. I. Stoeva, and C. a Mirkin, "Bio-bar-code-based DNA detection with PCR-like sensitivity.," *J. Am. Chem. Soc.*, vol. 126, no. 19, pp. 5932–5933, May 2004.

[153] N. Gan *et al.*, "A Novel Signal-Amplified Immunoassay for the Detection of C-Reactive Protein Using HRP-Doped Magnetic Nanoparticles as Labels with the Electrochemical Quartz Crystal Microbalance as a Detector.," *J. Anal. Methods Chem.*, vol. 2013, p. 482316, Jan. 2013.

[154] J.-M. Nam, C. S. Thaxton, and C. a Mirkin, "Nanoparticle-based bio-bar codes for the ultrasensitive detection of proteins.," *Science*, vol. 301, no. 5641, pp. 1884–1886, Sep. 2003.

[155] H. Gu, P.-L. Ho, K. W. T. Tsang, L. Wang, and B. Xu, "Using biofunctional magnetic nanoparticles to capture vancomycin-resistant enterococci and other gram-positive bacteria at ultralow concentration.," *J. Am. Chem. Soc.*, vol. 125, no. 51, pp. 15702–15703, Dec. 2003.

[156] J. M. Perez, F. J. Simeone, Y. Saeki, L. Josephson, and R. Weissleder, "Viral-induced self-assembly of magnetic nanoparticles allows the detection of viral particles in biological media.," *J. Am. Chem. Soc.*, vol. 125, no. 34, pp. 10192–10193, Aug. 2003.

[157] M. a. M. Gijs, "Magnetic bead handling on-chip: new opportunities for analytical applications," *Microfluid. Nanofluidics*, vol. 1, pp. 22–40, Oct. 2004.

[158] U. Lehmann, C. Vandevyver, V. K. Parashar, and M. a M. Gijs, "Droplet-based DNA purification in a magnetic lab-on-a-chip.," *Angew. Chem. Int. Ed. Engl.*, vol. 45, no. 19, pp. 3062–7, May 2006.

[159] J.-W. Choi, C. H. Ahn, S. Bhansali, and H. T. Henderson, "A new magnetic bead-based, filterless bio-separator with planar electromagnet surfaces for integrated bio-detection systems," *Sensors Actuators B Chem.*, vol. 68, no. 1–3, pp. 34–39, Aug. 2000.

[160] C. M. Gabardo, Y. Zhu, L. Soleymani, and J. M. Moran-Mirabal, "Bench-Top Fabrication of Hierarchically Structured High-Surface-Area Electrodes," *Adv. Funct. Mater.*, vol. 23, no. 24, pp. 3030–3039, Jun. 2013.

[161] T. Yanai, T. Shimokawa, Y. Watanabe, M. Nakano, and H. K. Suzuki, and Fukunaga, "Electrodeposited Fe–Ni Films Prepared in a Citric-Acid-Based Bath with Different pH Values," *IEEE Trans. Magn.*, vol. 50, no. 1, pp. 2013–2015, 2014.

[162] R. Abdel-Karim, Y. Reda, M. Muhammed, S. El-Raghy, M. Shoeib, and H. Ahmed, "Electrodeposition and Characterization of Nanocrystalline Ni-Fe Alloys," *J. Nanomater.*, vol. 2011, pp. 1–8, 2011.

[163] S. Park, D. G. Senesky, and A. P. Pisano, "ELECTRODEPOSITION OF PERMALLOY IN DEEP SILICON TRENCHES WITHOUT EDGE-OVERGROWTH UTILIZING DRY FILM PHOTORESIST," in *Micro Electro Mechanical Systems, 2009. MEMS 2009. IEEE 22nd International Conference on*, 2009, pp. 689–692.

[164] D. Gangasingh and J. B. Talbot, "Anomalous Electrodeposition of Nickel-Iron," *J. Electrochem. Soc.*, vol. 138, no. 12, pp. 1–7, 1991.

[165] U. Abidin, B. Y. Majlis, and J. Yunas, "Design and simulation of high magnetic gradient device for effective bioparticles trapping," in *2012 10th IEEE International Conference on Semiconductor Electronics (ICSE)*, 2012, no. 3, pp. 195–199.

[166] K. Smistrup, O. Hansen, H. Bruus, and M. F. Hansen, "Magnetic separation in microfluidic systems using microfabricated electromagnets—experiments and simulations," *J. Magn. Magn. Mater.*, vol. 293, no. 1, pp. 597–604, May 2005.

[167] J. Do, J. Choi, and C. H. Ahn, "Low-Cost Magnetic Interdigitated Array on a Plastic Wafer," *IEEE Trans. Magn.*, vol. 40, no. 4, pp. 3009–3011, 2004.

[168] C. H. Ahn and M. G. Allen, "Micromachined Planar Inductors on Silicon Wafers for MEMS Applications," *IEEE Trans. Ind. Electron.*, vol. 45, no. 6, pp. 866–876, 1998.

[169] S. H. Oh, K.-C. Lee, J. Chun, M. Kim, and S. S. Lee, "Micro heat flux sensor using copper electroplating in SU-8 microstructures," *J. Micromechanics Microengineering*, vol. 11, no. 3, pp. 221–225, May 2001.

[170] V. Venkatadri, B. Sammakia, K. Srihari, and D. Santos, "A Review of Recent Advances in Thermal Management in Three Dimensional Chip Stacks in Electronic Systems," *J. Electron. Packag.*, vol. 133, no. 4, p. 041011, 2011.

[171] A. Hosseini, D. N. Philpott, and L. Soleymani, "Enrichment of magnetic particles using temperature and magnetic field gradients induced by benchtop fabricated micro-electromagnets," *Lab Chip*, vol. 17, no. 23, pp. 4097–4104, 2017.

[172] K. T. Liao and C. F. Chou, "Nanoscale molecular traps and dams for ultrafast protein enrichment in high-conductivity buffers," *J. Am. Chem. Soc.*, vol. 134, no. 21, pp. 8742–8745, 2012.

[173] Y. Kang and D. Li, "Electrokinetic motion of particles and cells in microchannels," *Microfluid. Nanofluidics*, vol. 6, no. 4, pp. 431–460, 2009.

[174] C. Zhang, K. Khoshmanesh, A. Mitchell, and K. Kalantar-Zadeh, "Dielectrophoresis for manipulation of micro/nano particles in microfluidic systems," *Analytical and Bioanalytical Chemistry*, vol. 396, no. 1. pp. 401–420, 2010.

[175] K. Khoshmanesh, S. Nahavandi, S. Baratchi, A. Mitchell, and K. Kalantar-zadeh, "Dielectrophoretic platforms for bio-microfluidic systems," *Biosens. Bioelectron.*, vol. 26, no. 5, pp. 1800–1814, 2011.

[176] D. Ross and L. E. Locascio, "Microfluidic Temperature Gradient Focusing Microfluidic Temperature Gradient Focusing," *Anal. Chem.*, vol. 74, no. April, pp. 2556–2564, 2002.

[177] G. P. Hatch and R. E. Stelter, "Magnetic design considerations for devices and particles used for biological high-gradient magnetic separation (HGMS) systems," *J. Magn. Magn. Mater.*, vol. 225, no. 1–2, pp. 262–276, 2001.

[178] B. Le Drogoff, L. Clime, and T. Veres, "The influence of magnetic carrier size on the performance of microfluidic integrated micro-electromagnetic traps," *Microfluid. Nanofluidics*, vol. 5, no. 3, pp. 373–381, 2008.

[179] D. Erickson, D. Sinton, and D. Li, "Joule heating and heat transfer in poly(dimethylsiloxane) microfluidic systems.," *Lab Chip*, vol. 3, no. 3, pp. 141–149, 2003.

[180] S. Xu, G. W. Scherer, T. S. Mahadevan, and S. H. Garofalini, "Thermal expansion of confined water," *Langmuir*, vol. 25, no. 9, pp. 5076–5083, 2009.

[181] Z. Saiyed, S. Telang, and C. Ramchand, "Application of magnetic techniques in the field of drug discovery and biomedicine," *Biomagn. Res. Technol.*, vol. 1, no. 2, pp. 23–33, 2003.

[182] F. Liu *et al.*, "Highly sensitive and selective lateral flow immunoassay based on magnetic nanoparticles for quantitative detection of carcinoembryonic antigen," *Talanta*, vol. 161, pp. 205–210, 2016.

[183] C. Wyatt Shields Iv, C. D. Reyes, and G. P. López, "Microfluidic cell sorting: A review of the advances in the separation of cells from debulking to rare cell isolation," *Lab Chip*, vol. 15, no. 5, pp. 1230–1249, 2015.

[184] M. Zborowski and J. J. Chalmers, "Rare Cell Separation and Analysis by Magnetic Sorting," *Anal Chem.*, vol. 83, no. 21, pp. 8050–8056, 2011.

[185] A. A. S. Bhagat, H. Bow, H. W. Hou, S. J. Tan, J. Han, and C. T. Lim, "Microfluidics for cell separation," *Med. Biol. Eng. Comput.*, vol. 48, no. 10, pp. 999–1014, 2010.

[186] H. Tsutsui and C.-M. Ho, "Cell Separation by Non-Inertial Force Fields in Microfluidic Systems," *Mech Res Commun.*, vol. 36, no. 1, pp. 92–103, 2009.

[187] J. D. Besant, R. M. Mohamadi, P. M. Aldridge, Y. Li, E. H. Sargent, and S. O. Kelley, "Velocity valleys enable efficient capture and spatial sorting of nanoparticle-bound cancer cells.," *Nanoscale*, vol. 7, no. 14, pp. 6278–85, 2015.

[188] H. Lee, Y. Liu, D. Ham, and R. M. Westervelt, "Integrated cell manipulation system--CMOS/microfluidic hybrid.," *Lab Chip*, vol. 7, no. 3, pp. 331–7, Mar. 2007.

[189] S. H. Song, H. L. Lee, Y. H. Min, and H. Il Jung, "Electromagnetic microfluidic cell labeling device using on-chip microelectromagnet and multi-layered channels," *Sensors Actuators, B Chem.*, vol. 141, no. 1, pp. 210–216, 2009.

[190] J. Zeng, Y. Deng, P. Vedantam, T. R. Tzeng, and X. Xuan, "Magnetic separation of particles and cells in ferrofluid flow through a straight microchannel using two offset magnets," *J. Magn. Magn. Mater.*, vol. 346, no. 1, pp. 118–123, 2013.

[191] N. Pamme and C. Wilhelm, "Continuous sorting of magnetic cells via on-chip free-flow magnetophoresis," *Lab Chip*, vol. 6, no. 8, pp. 974–980, 2006.

[192] R. M. Mohamadi *et al.*, "Nanoparticle-mediated binning and profiling of heterogeneous circulating tumor cell subpopulations," *Angew. Chemie - Int. Ed.*, vol. 54, no. 1, pp. 139–143, 2015.

[193] J. D. Adams, U. Kim, and H. T. Soh, "Multitarget magnetic activated cell sorter," *Proc. Natl. Acad. Sci.*, vol. 105, no. 47, pp. 18165–18170, 2008.

[194] N. Sharon and H. Lis, "Lectins: Cell-Agglutinating and Sugar-Specific Proteins," *Science (80-.).*, vol. 177, no. 4053, pp. 949–959, 1972.

[195] M. Donolato *et al.*, "Magnetic domain wall conduits for single cell applications," *Lab Chip*, vol. 11, no. 17, pp. 2976–2983, 2011.

[196] C. M. Gabardo, R. C. Adams-McGavin, O. M. Vanderfleet, and L. Soleymani, "Rapid prototyping of microfluidic devices with integrated wrinkled gold micro-/nano textured electrodes for electrochemical analysis," *Analyst*, vol. 140, no. 16, pp. 5781–5788, 2015.

[197] D. C. Duffy, J. C. McDonald, O. J. A. Schueller, and G. M. Whitesides, "Rapid prototyping of microfluidic systems in poly(dimethylsiloxane)," *Anal. Chem.*, vol. 70, no. 23, pp. 4974–4984, 1998.

[198] M. Kolaczkowski, M. Van der Rest, A. Cybularz-Kolaczkowska, J. P. Soumillion,

W. N. Konings, and A. Goffeau, “Anticancer drugs, ionophoric peptides, and steroids as substrates of the yeast multidrug transporter Pdr5p,” *J. Biol. Chem.*, vol. 271, no. 49, pp. 31543–31548, 1996.

[199] Y. Li, J. Chen, and S. Y. Lun, “Biotechnological production of pyruvic acid,” *Appl. Microbiol. Biotechnol.*, vol. 57, no. 4, pp. 451–459, 2001.

[200] A. Hosseini *et al.*, “Conductive electrochemically-active lubricant-infused nanostructured surfaces attenuate coagulation and enable friction-less droplet manipulation,” *Adv. Mater. Interfaces*, vol. 5, no. 1, p. 1800617, 2018.

[201] A. E. Nel *et al.*, “Understanding biophysicochemical interactions at the nano–bio interface,” *Nat. Mater.*, vol. 8, no. 7, pp. 543–557, Jul. 2009.

[202] T. F. Didar, K. Li, T. Veres, and M. Tabrizian, “Separation of rare oligodendrocyte progenitor cells from brain using a high-throughput multilayer thermoplastic-based microfluidic device,” *Biomaterials*, vol. 34, no. 22, pp. 5588–5593, 2013.

[203] T. F. Didar, K. Bowey, G. Almazan, and M. Tabrizian, “A Miniaturized Multipurpose Platform for Rapid, Label-Free, and Simultaneous Separation, Patterning, and In Vitro Culture of Primary and Rare Cells,” *Adv. Healthc. Mater.*, vol. 3, no. 2, pp. 253–260, Feb. 2014.

[204] A. Roosjen, H. C. van der Mei, H. J. Busscher, and W. Norde, “Microbial Adhesion to Poly(ethylene oxide) Brushes: Influence of Polymer Chain Length and Temperature,” *Langmuir*, vol. 20, no. 25, pp. 10949–10955, Dec. 2004.

[205] I. Banerjee, R. C. Pangule, and R. S. Kane, “Antifouling Coatings: Recent Developments in the Design of Surfaces That Prevent Fouling by Proteins, Bacteria, and Marine Organisms,” *Adv. Mater*, vol. 23, pp. 690–718, 2011.

[206] M. S. Wang, L. B. Palmer, J. D. Schwartz, and A. Razatos, “Evaluating Protein Attraction and Adhesion to Biomaterials with the Atomic Force Microscope,” *Langmuir*, vol. 20, no. 18, pp. 7753–7759, 2004.

[207] M. V Sefton, C. H. Gemmell, and M. B. Gorbet, “What really is blood compatibility? *,” *J. Biomater. Sci. Polym. Edn*, vol. 11, no. 11, pp. 1165–1182, 2000.

[208] S. Choi and J. Chae, “Methods of reducing non - specific adsorption in microfluidic biosensors,” *J . Micromech . Microeng*, vol. 20, pp. 75015–9, 2010.

[209] J. Xie, C. Xu, N. Kohler, Y. Hou, and S. Sun, “Controlled PEGylation of Monodisperse Fe 3 O 4 Nanoparticles for Reduced Non-Specific Uptake by Macrophage Cells**,” *Adv. Mater.*, vol. 19, pp. 3163–3166, 2007.

[210] Y. H. Yeong, C. Wang, K. J. Wynne, and M. C. Gupta, “Oil-Infused Superhydrophobic Silicone Material for Low Ice Adhesion with Long-Term Infusion Stability,” *ACS Appl. Mater. Interfaces*, vol. 8, no. 46, pp. 32050–32059,

Nov. 2016.

[211] G. H. Zhu, C. Zhang, C. Wang, and N. S. Zacharia, “Gel-Infused Slippery Surface with Enhanced Longevity and Thermally Controllable Sliding Properties,” *Adv. Mater. Interfaces*, vol. 3, no. 20, p. 1600515, Oct. 2016.

[212] A. K. Epstein, T.-S. Wong, R. A. Belisle, E. M. Boggs, and J. Aizenberg, “Liquid-infused structured surfaces with exceptional anti-biofouling performance.,” *Proc. Natl. Acad. Sci. U. S. A.*, vol. 109, no. 33, pp. 13182–13187, Aug. 2012.

[213] H. Guo *et al.*, “Bio-Inspired Superhydrophobic and Omniphobic Wood Surfaces,” *Adv. Mater. Interfaces*, vol. 4, no. 1, p. 1600289, Jan. 2017.

[214] A. Keiser, L. Keiser, C. Clanet, and D. Quéré, “Drop friction on liquid-infused materials,” *Soft Matter*, vol. 13, no. 39, pp. 6981–6987, Oct. 2017.

[215] P. Irajizad, M. Hasnain, N. Farokhnia, S. M. Sajadi, and H. Ghasemi, “Magnetic slippery extreme icephobic surfaces,” *Nat. Commun.*, vol. 7, p. 13395, Nov. 2016.

[216] J. D. Smith *et al.*, “Droplet mobility on lubricant-impregnated surfaces,” *Soft Matter*, vol. 9, no. 6, pp. 1772–1780, 2013.

[217] F. Schellenberger *et al.*, “Direct observation of drops on slippery lubricant-infused surfaces,” *Soft Matter*, vol. 11, no. 38, pp. 7617–7626, Sep. 2015.

[218] K. Doll *et al.*, “Development of Laser-Structured Liquid-Infused Titanium with Strong Biofilm-Repellent Properties,” *ACS Appl. Mater. Interfaces*, vol. 9, no. 11, pp. 9359–9368, Mar. 2017.

[219] R. Qiu *et al.*, “Fabrication of slippery liquid-infused porous surface based on carbon fiber with enhanced corrosion inhibition property,” *Colloids Surfaces A Physicochem. Eng. Asp.*, vol. 453, no. Complete, pp. 132–141, 2014.

[220] Z. Brabcova, G. McHale, G. G. Wells, C. V. Brown, and M. I. Newton, “Electric field induced reversible spreading of droplets into films on lubricant impregnated surfaces,” *Appl. Phys. Lett.*, vol. 110, no. 12, p. 121603, Mar. 2017.

[221] P. Kim, T.-S. Wong, J. Alvarenga, M. J. Kreder, W. E. Adorno-Martinez, and J. Aizenberg, “Liquid-Infused Nanostructured Surfaces with Extreme Anti-Ice and Anti-Frost Performance,” *ACS Nano*, vol. 6, no. 8, pp. 6569–6577, Aug. 2012.

[222] P. Kim, M. J. Kreder, J. Alvarenga, and J. Aizenberg, “Hierarchical or Not? Effect of the Length Scale and Hierarchy of the Surface Roughness on Omniphobicity of Lubricant-Infused Substrates,” *Nano Lett.*, vol. 13, no. 4, pp. 1793–1799, 2013.

[223] S. Sunny, N. Vogel, C. Howell, T. L. Vu, and J. Aizenberg, “Lubricant-Infused Nanoparticulate Coatings Assembled by Layer-by-Layer Deposition,” *Adv. Funct. Mater.*, vol. 24, no. 42, pp. 6658–6667, Nov. 2014.

[224] S. Wooh and H.-J. Butt, “A Photocatalytically Active Lubricant-Impregnated

Surface," *Angew. Chemie Int. Ed.*, vol. 56, no. 18, pp. 4965–4969, Apr. 2017.

[225] C. Hao *et al.*, "Electrowetting on liquid-infused film (EWOLF): Complete reversibility and controlled droplet oscillation suppression for fast optical imaging," *Sci. Rep.*, vol. 4, p. 6846, 2014.

[226] X. Liu, Y. Liang, F. Zhou, and W. Liu, "Extreme wettability and tunable adhesion: biomimicking beyond nature?," *Soft Matter*, vol. 8, no. 7, pp. 2070–2086, Jan. 2012.

[227] M. Villegas, Z. Cetinic, A. Shakeri, and T. F. Didar, "Fabricating smooth PDMS microfluidic channels from low-resolution 3D printed molds using an omniphobic lubricant-infused coating," *Anal. Chim. Acta*, vol. 1000, pp. 248–255, Feb. 2018.

[228] P. W. Wilson *et al.*, "Inhibition of ice nucleation by slippery liquid-infused porous surfaces (SLIPS)," *Phys. Chem. Chem. Phys.*, vol. 15, no. 2, pp. 581–585, Dec. 2013.

[229] S. Anand, A. T. Paxson, R. Dhiman, J. D. Smith, and K. K. Varanasi, "Enhanced Condensation on Lubricant-Impregnated Nanotextured Surfaces," *ACS Nano*, vol. 6, no. 11, pp. 10122–10129, Nov. 2012.

[230] M. J. Kratochvil, M. A. Welsh, U. Manna, B. J. Ortiz, H. E. Blackwell, and D. M. Lynn, "Slippery Liquid-Infused Porous Surfaces that Prevent Bacterial Surface Fouling and Inhibit Virulence Phenotypes in Surrounding Planktonic Cells," *ACS Infect. Dis.*, vol. 2, no. 7, pp. 509–517, Jul. 2016.

[231] D. Zhao *et al.*, "Fouling-resistant Behavior of Liquid-infused Porous Slippery Surfaces," *Chinese J. Polym. Sci.*, vol. 35, no. 7, p. 887−896, 2017.

[232] C. Howell *et al.*, "Self-Replenishing Vascularized Fouling-Release Surfaces," *ACS Appl. Mater. Interfaces*, vol. 6, no. 15, pp. 13299–13307, Aug. 2014.

[233] R. S. Smith *et al.*, "Vascular catheters with a nonleaching poly-sulfobetaine surface modification reduce thrombus formation and microbial attachment.," *Sci. Transl. Med.*, vol. 4, no. 153, p. 153ra132, Sep. 2012.

[234] J. M. Harris and R. B. Chess, "Effect of pegylation on pharmaceuticals," *Nat. Rev. Drug Discov.*, vol. 2, no. 3, pp. 214–221, Mar. 2003.

[235] I. Sotiri, J. C. Overton, A. Waterhouse, and C. Howell, "Immobilized liquid layers: A new approach to anti-adhesion surfaces for medical applications," *Exp. Biol. Med.*, vol. 241, no. 9, pp. 909–918, May 2016.

[236] C. M. Gabardo, R. C. Adams-McGavin, B. C. Fung, E. J. Mahoney, Q. Fang, and L. Soleymani, "Rapid prototyping of all-solution-processed multi-lengthscale electrodes using polymer-induced thin film wrinkling.," *Sci. Rep.*, vol. 7, p. 42543, Feb. 2017.

[237] S. Lin, E. K. Lee, N. Nguyen, and M. Khine, “Thermally-induced miniaturization for micro- and nanofabrication: progress and updates.,” *Lab Chip*, vol. 14, no. 18, pp. 3475–88, Sep. 2014.

[238] S. M. Woo, C. M. Gabardo, and L. Soleymani, “Prototyping of Wrinkled Nano-/Microstructured Electrodes for Electrochemical DNA Detection,” *Anal. Chem.*, vol. 86, no. 2014, p. 12341−12347, 2014.

[239] R. C. Adams-McGavin *et al.*, “Nanoporous and wrinkled electrodes enhance the sensitivity of glucose biosensors,” *Electrochim. Acta*, vol. 242, pp. 1–9, 2017.

[240] C. M. Gabardo, A. Hosseini, and L. Soleymani, “A New Wrinkle in Biosensors: Wrinkled electrodes could be a breakthrough for lab-on-a-chip devices.,” *IEEE Nanotechnol. Mag.*, vol. 10, no. 2, pp. 6–18, Jun. 2016.

[241] P. Tseng *et al.*, “Flexible and stretchable micromagnet arrays for tunable biointerfacing,” *Adv Mater*, vol. 27, no. 6, pp. 1083–1089, Apr. 2015.

[242] J. Y. Chung, A. J. Nolte, and C. M. Stafford, “Surface wrinkling: A versatile platform for measuring thin-film properties,” *Adv. Mater.*, vol. 23, no. 3, pp. 349–368, 2011.

[243] S. Nishimotoab and B. Bhushan, “Bioinspired self-cleaning surfaces with superhydrophobicity, superoleophobicity, and superhydrophilicity,” *RSC Adv.*, vol. 3, no. 3, pp. 671–690, Dec. 2013.

[244] C. Yu, X. Zhu, K. Li, M. Cao, and L. Jiang, “Manipulating Bubbles in Aqueous Environment via a Lubricant-Infused Slippery Surface,” *Adv. Funct. Mater.*, p. 1701605, May 2017.

[245] Z. Chu and S. Seeger, “Superamphiphobic surfaces,” *Chem. Soc. Rev.*, vol. 43, no. 8, pp. 2784–2798, Mar. 2014.

[246] K. Liu, Y. Tian, and L. Jiang, “Bio-inspired superoleophobic and smart materials: Design, fabrication, and application,” *Prog. Mater. Sci.*, vol. 58, no. 4, pp. 503–564, May 2013.

[247] M. Badv, I. H. Jaffer, J. I. Weitz, and T. F. Didar, “An omniphobic lubricant-infused coating produced by chemical vapor deposition of hydrophobic organosilanes attenuates clotting on catheter surfaces,” *Sci. Rep.*, vol. 7, no. 1, p. 11639, Dec. 2017.

[248] M. Kind, C. Wöll, and H. Petek, “Organic surfaces exposed by self-assembled organothiol monolayers: Preparation, characterization, and application,” *Prog. Surf. Sci.*, vol. 84, pp. 230–278, 2009.

[249] W. Wang and M. W. Vaughn, “Morphology and Amine Accessibility of (3-Aminopropyl) Triethoxysilane Films on Glass Surfaces,” *Scanning*, vol. 30, no. 2, pp. 65–77, Mar. 2008.

[250] M. A. Islam *et al.*, "Comparison of Structural and Optical Properties of CdS Thin Films Grown by CSVT, CBD and Sputtering Techniques," *Energy Procedia*, vol. 33, pp. 203–213, 2013.

[251] A. Chandekar, S. K. Sengupta, and J. E. Whitten, "Thermal stability of thiol and silane monolayers: A comparative study," *Appl. Surf. Sci.*, vol. 256, no. 9, pp. 2742–2749, Feb. 2010.

[252] C. Semprebon, G. Mchale, and H. Kusumaatmaja, "Apparent contact angle and contact angle hysteresis on liquid infused surfaces," *Soft Matter*, vol. 13, no. 13, pp. 101–110, 2017.

[253] A. B. D. Cassie and S. Baxter, "Wettability of porous surfaces," *Trans. Faraday Soc.*, vol. 40, no. 0, p. 546, Jan. 1944.

[254] K.-Y. Law and H. Zhao, *Surface wetting : characterization, contact angle, and fundamentals*. Springer International Publishing, 2016.

[255] A. Shahraz, A. Borhan, and K. A. Fichthorn, "A theory for the morphological dependence of wetting on a physically patterned solid surface," *Langmuir*, vol. 28, no. 40, pp. 14227–14237, Oct. 2012.

[256] E. Celia, T. Darmanin, E. Taffin de Givenchy, S. Amigoni, and F. Guittard, "Recent advances in designing superhydrophobic surfaces," *J. Colloid Interface Sci.*, vol. 402, pp. 1–18, 2013.

[257] J. M. Berg, L. G. T. Eriksson, P. M. Claesson, K. Grete, and N. Barvet, "Three-Component Langmuir-Blodgett Films with a Controllable Degree of Polarity," *Langmuir*, vol. 10, pp. 1225–1234, 1994.

[258] V. H. Dalvi and P. J. Rossky, "Molecular origins of fluorocarbon hydrophobicity.," *Proc. Natl. Acad. Sci. U. S. A.*, vol. 107, no. 31, pp. 13603–7, Aug. 2010.

[259] J. W. Yau, A. R. Stafford, P. Liao, J. C. Fredenburgh, R. Roberts, and J. I. Weitz, "Mechanism of catheter thrombosis: comparison of the antithrombotic activities of fondaparinux, enoxaparin, and heparin in vitro and in vivo," *Blood*, vol. 118, no. 25, pp. 6667–6674, 2011.

[260] J. Y. Lee and R. A. Deininger, "Detection of E. coli in beach water within 1 hour using immunomagnetic separation and ATP bioluminescence," *Luminescence*, vol. 19, no. 1, pp. 31–36, 2004.

[261] M. Varshney, L. Yang, X. Su, and Y. Li, "Magnetic nanoparticle-antibody conjugates for the separation of Escherichia coli O157:H7 in ground beef.," *J. Food Prot.*, vol. 68, no. 9, pp. 1804–1811, 2005.

[262] K. A. Stevens and L. A. Jaykus, "Bacterial separation and concentration from complex sample matrices: A review," *Crit. Rev. Microbiol.*, vol. 30, no. 1, pp. 7–24, 2004.

[263] X. L. Su and Y. Li, “Quantum dot biolabeling coupled with immunomagnetic separation for detection of Escherichia coli O1517:H7,” *Anal. Chem.*, vol. 76, no. 16, pp. 4806–4810, 2004.

[264] H. WANG, Y. LI, A. WANG, and M. SLAVIK, “Rapid, Sensitive, and Simultaneous Detection of Three Foodborne Pathogens Using Magnetic Nanobead–Based Immunoseparation and Quantum Dot–Based Multiplex Immunoassay,” *J. Food Prot.*, vol. 74, no. 12, pp. 2039–2047, 2011.

[265] Y. Wang, J. Dostalek, and W. Knoll, “Magnetic Nanoparticle-Enhanced Biosensor Based on Grating-Coupled Surface Plasmon Resonance,” *Anal. Chem.*, vol. 83, no. 16, pp. 6202–6207, 2011.